

THESIS

TOTAL AND DIFFERENTIAL SPUTTER YIELDS OF BORON NITRIDE

Submitted by

James Leo Topper IV

Department of Mechanical Engineering

In partial fulfillment of the requirements

For the Degree of Master of Science

Colorado State University

Fort Collins, Colorado

Spring 2011

Master's Committee:

Advisor: Azer Yalin

John Williams

Carmen Menoni

Copyright by James Leo Topper IV 2011

All Rights Reserved

ABSTRACT

TOTAL AND DIFFERENTIAL SPUTTER YIELDS OF BORON NITRIDE

A quartz crystal microbalance (QCM) based system was used to measure total and differential sputter yields of Boron Nitride targets due to Xenon ion bombardment. The system used a four-grid ion source to generate a (nearly) mono-energetic beam of ions with a low singles-to-doubles ratio that remains well-collimated at low energies. Boron Nitride sputter yields were measured as a function of Xenon ion energy and incidence angle. Total yield measurements are found by integrating differential yield data taken by the QCM. The measurement system was validated by sputtering Molybdenum, for which the measured yields compared well with published data. For Boron Nitride, complementary weight loss sputter yield measurements were conducted, but were found to be less accurate due to moisture absorption effects when samples were exposed to atmosphere. The effects of neutralization of both the ion beam and target surface were investigated, and a plasma bridge neutralizer (PBN) was used to prevent surface charge buildup on the target. The measured total sputter yields were found to vary strongly due to neutralization conditions, and were found to be approximately a factor of two higher than those available in the literature when aggressive target and beam neutralization was applied. The angular shape of the differential sputter yield profiles was described with fit parameters from the Modified Zhang equation.

ACKNOWLEDGEMENTS

I would like to thank my parents for encouraging me to follow my interests, and for their support before, during and after my departure for CSU. Without family support, one cannot get far in life. Family will always be the bedrock from which I can reach for the stars.

Thank you to Azer Yalin, for bringing me out in the first place, and for providing such an excellent working environment at the LPDL. Thanks are also due for his understanding (and participation!) that Grad students occasionally need to unwind on the slopes.

Thank you to John Williams for all the direction and assistance with the equipment, materials, and troubleshooting, without which none of us would have any idea what was going on.

A special thank you to Dr. Binyamin Rubin for bringing me up to speed and teaching me all the important stuff about running the system, and for being the fall-back whenever John wasn't around. I would have been hard pressed to find a better post-doc to work with.

Thank you to my professors who have guided me toward this work, and who have been some of the most amazing educators in the world. You make a huge difference in the lives of hundreds of eager students. In particular, thank you to Dr. Alec Gallimore, who will always be the best, smartest, and most capable professor I ever had, and to Dr. Paul Wilbur, who continued the trend of amazing professors in the electric propulsion field, and to John Olstad, who started it all, way back in High School.

Thanks to all my co-workers, without whom I would not have had the instrumental sounding board for all my ideas. Your firm grasp of reality (as well as really good understanding of physics) prevented me from making a lot of mistakes.

Finally, a big thanks to my fiancée Laura, who gives me the strength, commitment, and foundation to accomplish anything.

TABLE OF CONTENTS

Abstract	ii
Acknowledgements	iii
Table of Contents	iv
List of Figures	vii
List of Tables	xi

Chapter

1. Introduction	1
1.1 Electric Propulsion	2
1.2 Sputtering Basics	8
1.2.1 The Sigmund Equation	8
1.2.2 Evolution of Model Equations	11
1.3 The Role of Sputtering in Electric Propulsion ...	12
1.4 Boron Nitride in Hall-Effect Thrusters	14
1.5 Sputter Measurement Techniques	16
1.5.1 Rutherford Backscattering	16
1.5.2 Mass Spectrometry	17
1.5.3 Laser Techniques	18
2. Experimental Setup	21
2.1 Measurement System Overview	21
2.1.1 Definition of Angles	23

2.2 Quartz Crystal Microbalance	24
2.2.1 The Sauerbrey Equation	25
2.2.2 Quartz Crystal	26
2.2.3 Measurement	27
2.3 Data Acquisition	28
2.4 Ion Source and Four Grid Optics	29
2.4.1 Ion Source	29
2.4.2 Four Grid Ion Optics	30
2.4.3 Beam Profiling	32
2.4.4 Beam Characterization	34
2.5 Boron Nitride Test Samples	40
2.5.1 Boron Nitride Purity	40
2.5.2 Moisture Absorption and Atmospheric Effects ...	41
2.5.3 Surface Analysis	44
2.6 Weight Loss Measurements	45
2.6.1 Procedure	46
2.6.2 Ion Implantation	47
2.6.3 Sputter Yield Calculation	48
2.7 System Thermal Control	49
2.8 Sample Thermal Control	51
3. QCM Signal Analysis	54
3.1 The Modified Zhang Equation	55
3.2 Analysis Considerations	56
3.2.1 Assumptions	56
3.2.2 Condensables	57
3.3 Matlab Analysis	59
4. Total Sputter Yields	60
4.1 Molybdenum Validation Experiments	60
4.2 Total Sputter Yields of Boron Nitride	61
4.3 Dependence of Sputter Yields on Neutralization	68

5. Differential Sputter Yield Profiles	72
5.1 Fitted Profiles	72
5.2 Zhang-Fit Hemispheres	75
5.3 E^* Shape Factors	78
6. Conclusions	80
6.1 Conclusions	80
6.2 Continuing Research	82
7. References	84
Appendices	88
A. Sputter Yield Data Tables	88
B. Matlab QCM Analysis Program	91

LIST OF FIGURES

Figure 1.	Left, the NEXT Ion Thruster at NASA’s Glenn Research Center. Right, a 2 kW Hall Thruster operating at Princeton Plasma Physics Laboratory. 7
Figure 2.	A Hall Thruster after 500 hours of operation at Keldysh Research Center. Erosion is visible along the insulator channel wall. 13
Figure 3.	Ion impact energy distribution in the thruster channel for 1 kW Hall Thruster. 14
Figure 4.	Erosion near an SPT-100 Hall Thruster exit plane. 15
Figure 5.	CRDS schematic. 19
Figure 6.	QCM measurement system. Major components are labeled. 22
Figure 7.	Solid model of QCM with angle definitions. 24
Figure 8.	FFX simulation of a four grid ion beamlet. Grids are labeled. 32
Figure 9.	Photograph of the MAPPS system. 33
Figure 10.	Left: Profile of a 250 eV beam at an axial distance of 16.3 cm from the ion source. Right: Profile of a 30 eV beam at an axial distance of 16.3 cm from the ion source. 34
Figure 11.	Exponential beam current decay due to charge exchange collisions and ion scattering. 37
Figure 12.	Four different ion energy distributions for beam voltages of 30, 80, 150, and 250 V (left to right). 38
Figure 13.	$\vec{E} \times \vec{B}$ probe schematic. 39
Figure 14.	$\vec{E} \times \vec{B}$ Probe trace for a beam energy of 250 eV. 39

Figure 15.	Moisture absorption for HBC and HBR grades of Boron Nitride. 42
Figure 16.	Mass gain of HP-grade Boron Nitride as a function of time of atmospheric exposure. Different symbols on the graph represent different test series. The starting sample mass is approximately 150 g. Time zero corresponds to 90 minutes after removal from the vacuum chamber. 43
Figure 17.	Measured sputter yields of HBR Boron Nitride after different bake-out procedures. 44
Figure 18.	SEM images of HBC Boron Nitride surface. Left: Unspattered. Right: After 15 hour dose of 250 eV Xe ⁺ ions. The scale for the upper two images is 100 μm, while the lower image scale is 10 μm. 45
Figure 19.	Angularly resolved XPS measurements of Xe in HBC-grade Boron Nitride target. The x-axis represents the emission angle of the electrons with respect to the surface normal. 48
Figure 20.	Sample holder designed for cartridge heaters. Pen is provided for size reference. 51
Figure 21.	Cooled sample holder. 52
Figure 22.	Left: XPS scan of HBC Boron Nitride surface. Right: QCM crystal surface. 58
Figure 23.	Molybdenum bombardment at normal incidence (CSU 2008). Yamamura & Tawara prediction, Kolasinski data, Doerner data, and former CSU (CSU 2007) data are provided for comparison. 61
Figure 24.	Total sputter yields of HBC-grade Boron Nitride at normal incidence. 63
Figure 25.	Total sputter yields of HBR-grade Boron Nitride at normal incidence. 63
Figure 26.	Total sputter yields of HP-grade Boron Nitride at normal incidence. 64
Figure 27.	Total sputter yields of all three grades of Boron Nitride at normal ion incidence. 64

Figure 28.	Comparison of total sputter yields to other published values. See text. 65
Figure 29.	Sputter yields of all three grades of Boron Nitride at 100 eV. A Yamamura prediction is provided for reference, and calculated using the average values for Boron and Nitrogen and their total atomic weight. Since the Yamamura prediction is intended for monatomic species, it should be viewed as a guide, not an expectation. 67
Figure 30.	Sputter yield of HBC-grade Boron Nitride at 250 eV. The Yamamura prediction is provided for reference, calculated using the average values for Boron and Nitrogen and their total atomic weight. 67
Figure 31.	Sputter yield of HBC-grade Boron Nitride at 350 eV. The Yamamura prediction is provided for reference, and calculated using the average values for Boron and Nitrogen and their total atomic weight. 68
Figure 32.	Comparison of sputter yield of Boron Nitride against filament-neutralized beam current ($I_{filament} \sim 6 I_{beam}$) with and without the Plasma Bridge Neutralizer (PBN) installed in the system. 69
Figure 33.	Sputter yield rate with variation of the primary (source) neutralizer emission. 70
Figure 34.	Sputter yield rate with variation of the PBN emission. 71
Figure 35.	Fitted profile of a QCM sweep over Molybdenum at 150 eV, normal incidence. Red dots are actual data points, the blue line is the Modified Zhang fit, and the green dashed line is a diffuse profile with the same total yield. 73
Figure 36.	HBC-grade Boron Nitride at 350 eV, normal incidence. 73
Figure 37.	Fitted profiles of HBC-grade Boron Nitride at various angles of ion incidence. (a) $\beta = 15^\circ$, (b) $\beta = 30^\circ$, (c) $\beta = 45^\circ$, (d) $\beta = 60^\circ$. For clarity, the y-axis in these graphs is the differential sputter yield. 74
Figure 38.	Zhang-fit hemispheres for various beam ion energies at normal incidence. 76

Figure 39.	Zhang-fit hemispheres for various incidence angles at 100 eV. The arrows demonstrate the angle of ion incidence. 76
Figure 40.	HBC-grade Boron Nitride at 5° incidence at 150 eV. Note the asymmetry between the left and right halves (left and right of $\alpha = 0$), as compared to the diffuse profile. 77
Figure 41.	Zhang-fit hemisphere of HBC-grade Boron Nitride at 5° incidence. Note that the forward sputter lobe is more than 10% higher than the backscatter lobe, indicating a strong asymmetry even at near-normal angles of incidence. 77
Figure 42.	Evolution of the ratio $\frac{E^*}{E}$ with respect to beam ion energy E for all studied grades of Boron Nitride at normal incidence. 79

LIST OF TABLES

Table 1.	Some thruster types and their associated specific impulse 5
Table 2.	Ion source characterization data 35
Table A1.	Raw sputter yield data for HBC-grade Boron Nitride. Yields represent condensable components, not converted total yields. 88
Table A2.	Raw sputter yield data for HBR-grade Boron Nitride 89
Table A3.	Raw sputter yield data for HP-grade Boron Nitride 90

1. Introduction

Since the dawn of time, man has gazed up at the stars and desired to explore the vast depths unknowable from the ground. The scientific achievements of Dr. von Braun in the 1940's in the field of rocketry provided the first hopes of venturing into space, and in the following decades many of the greatest accomplishments in mankind's history were made: sending living creatures into space, sending men into space, landing men on the moon, and launching observational spacecraft to distant planets. The more knowledge that was gained, the hungrier man became to further increase his knowledge of the stars. At the same time, as that knowledge has expanded man's understanding of the realm of physics, it has become more apparent that chemical rocketry will not provide the means to sate this exploratory desire. A new propulsive method was needed for travelling between the stars.

In the 1960's the first electric thrusters were flown. Since then, electric propulsion has become the modern hope for space travel. Electric rockets are now used on many satellites, and on several missions beyond the Earth's sphere of influence. Electric propulsion is also the only currently feasible means of sending mankind out into the distant solar system.

1.1 Electric Propulsion

All space propulsion relies on Newton's Third Law: *for every action, there is an equal and opposite reaction*. This means if an object is forced out of a nozzle, regardless of the means by which it is accelerated, the object pushes back against the nozzle with an equal force. Modern engines generate thrust in one of two ways: either a large mass is accelerated by a small amount, or a small mass is accelerated by a large amount. Chemical rocketry works on the former principle, while electric rocketry works on the latter. In an electric thruster, ions are accelerated, which in turn provides the thrust force on the spacecraft. However, to achieve any significant thrust, these ions must be accelerated to very high velocities. In an electrostatic thruster, this acceleration is achieved through an electric field between two biased sources.

There are many types of electric propulsion thrusters. The two types of thrusters considered in this study are Ion Engines and Hall-Effect Thrusters (also called Stationary Plasma Thrusters). In an ion engine, a roughly cylindrical discharge chamber containing an anode and a cathode is operated in near-vacuum. Neutral fuel gas, often Xenon or Argon, is pumped into the discharge chamber at a flow rate \dot{m} . Electrons are generated by a cathode. In spacecraft and long-term missions, the cathode is a hollow tube with a low-work function insert, typically impregnated with Barium Calcium Aluminum. This insert is heated to stimulate electron emission. Electrons accelerated by the potential difference between the cathode and anode

interact with the neutral fuel gas, generating a plasma. At the chamber exit, two or more charged grids create the ion beam itself. The inner-most (relative to the thruster chamber) grid is called the “screen”, and is kept at positive potential, typically equal to the cathode potential and with only the anode being more positive. Just downstream of the screen grid is the acceleration grid, or “accel grid”. This is kept at negative potential with respect to ground. The electric field between the screen and accelerator grids accelerates ions out of the thruster chamber. In some ion engines, a third grid placed just downstream of the accel grid and kept at ground potential helps focus the ions once they have passed the accel grid and therein provides a more collimated beam. After leaving the accelerator grid, the ions pass a neutralizer. In space-based ion engines, this neutralizer is an additional cathode, held at a potential about 20 to 40 volts below the beam plasma. These electrons do not necessarily neutralize the ions, but rather maintain a constant space charge in the downstream plasma, as well as neutralizing the overall charge on the spacecraft.

The grids on an ion source must be very carefully aligned. The electric field between the grids accelerates ions along field lines, which run more or less perpendicular to the grids. Thus, if the holes are not nearly perfectly aligned, the electric field will accelerate the ions directly into the downstream grid, causing significant erosion and seriously degrading the performance and lifetime of the thruster.

Ion engines have optimal operating conditions based on their design. Chamber size, grid spacing, grid potentials, fuel mass flow rate, and anode placement all contribute to the thrust and efficiency of the engine. One important measure of thruster performance is perveance¹

$$\mathcal{P} = \frac{j_{max} \ell_g^2}{\varphi_0^{\frac{3}{2}}} \quad (1)$$

where j_{max} is the maximum beam current which can be extracted, φ_0 is the grid potential difference, and ℓ_g is the grid spacing. For a given ion source, to obtain maximum thrust it is ideal to operate as close to the perveance limit as possible; that is, to extract as close to j_{max} as possible from the source at specific grid potentials. However, from a lifetime standpoint, it is more appropriate to operate below the perveance limit. High beam current (J_B) maximizes the thruster efficiency¹:

$$\eta_t = \eta_u \eta_p = \left(\frac{m_+^2 g^2 \dot{m}}{2 \varepsilon^2 \dot{m}_B^2} \right) \frac{J_B I_{sp}^2}{V_B + V_{NC} + \varepsilon} \quad (2)$$

where m_+ is the ion mass, g is the acceleration due to gravity (9.8 m/s^2), \dot{m} is the mass flow rate into the thruster and \dot{m}_B is the mass flow rate out of the thruster in the ion beam (which combined form the propellant utilization efficiency η_u), ε is the ionization energy of the fuel gas, I_{sp} is the specific impulse of the thruster, and V_{NC} and V_B are the neutralizer and overall beam voltages (which form the power usage efficiency η_p). From equation (2), it can be seen that efficiency is maximized through large ion mass, low ionization energy, and high specific impulse and beam current.

Specific impulse is another convenient way to describe the performance of an engine, as it compares the thrust provided by the engine to the mass flow rate.

$$I_{sp} = \frac{T}{\dot{m}g_0} \approx \frac{v_e}{g_0} \quad (3)$$

From equation (3), the optimal specific impulse is achieved when the maximum thrust (T) is reached per gram of fuel passing through the engine, or similarly when the exhaust velocity (v_e) is maximized. The equation is defined using the acceleration due to gravity at the surface of the earth (g_0). Most rockets function at a specific impulse in the vicinity of 300 – 400 s. Ion thrusters can operate from about 2500 to over 10,000 s, and advanced plasma thrusters can reach 100,000 s or more.

Table 1. Some thruster types and their associated specific impulse¹

Engine	Thrust (N)	Specific Impulse (s)
Space Shuttle Main Engine (SSME)	1,817,400	453
Resistojet	0.5 - 1	300
Arcjet	0.1 - 0.3	500-600
Hall Thruster	0.03 – 2	1500-2000
Ion Thruster	0.09 – 0.4	2500-3600

However, high I_{sp} comes at a cost. From equation (3), high specific impulse must be achieved in one of two ways: either the rocket must have very high thrust or very low mass flow. Thrust is fuel mass flow multiplied by its velocity. Thus the initial principle from this section is demonstrated – high thrust requires large fuel mass flow or large exhaust velocity. For long-distance space missions, there are no refueling stations along the way. Since the spacecraft must carry its entire fuel supply internally, minimizing the mass of fuel is important

$$\Delta v = v_e \ln \left(\frac{m_0}{m_1} \right) \quad (4)$$

Equation 4 is called the “Rocket Equation”, in which Δv is the total velocity change which the spacecraft must undergo, v_e is the exhaust velocity of the engine, m_0 is the initial mass of the spacecraft, and m_1 is the final (dry) mass of the spacecraft once the fuel has been burned. Therefore, to both achieve high I_{sp} and meet the mission requirements for long deep space travel, the thruster must accelerate the fuel to very high speeds. Since the acceleration of the fuel is due to the potential difference between the grids, it would seem that maximizing this potential difference would be the optimal condition. However, large potential differences mean large values of V_B and V_A , the beam potential and the acceleration grid potential, respectively. From equation (2), large values of V_B reduce the efficiency of the engine. It is therefore a balance which must be obtained between a high current, high thrust device and a highly efficient device.

Another type of electrostatic thruster operates on the Hall Effect. Hall Thrusters create crossed electric and magnetic fields, which cause ions to experience an acceleration due to the Lorentz Force, shown below (5)

$$\vec{F} = q[\vec{E} + (\vec{v} \times \vec{B})] \quad (5)$$

where q is the charge of the ion, \vec{E} is the electric field, \vec{v} is the ion velocity, and \vec{B} is the magnetic field. The net force from equation (5) is axially outward from the thruster for ions. Using this reaction, electrons generated from a cathode downstream and just outside the plume of the beam are drawn into the thruster.

Once these electrons reach the thruster channel, they begin to circulate, both around the central magnetic pole of the thruster and gyroscopically in their path. This leads to collisions between the gyrating, circulating electrons and neutrals injected directly into the thruster channel. The gyroscopic circulation is governed by the electron gyro-radius for electron motion in electric and magnetic fields¹ (6),

$$r_e = \frac{c\sqrt{m_e k}}{e} \left(\frac{\sqrt{T_e}}{B} \right) \quad (6)$$

where r_e is the electron gyroradius, c is the speed of light in a vacuum, k is Boltzmann's Constant, e is the elementary charge, T_e is the electron temperature, and B is the magnetic field strength. This gyration has the effect of increasing the path length the electron must travel before being collected at an anode, thus increasing the likelihood of an ionization collision with a neutral gas particle. Figure 1 is a picture of an Ion Thruster at the NASA Glenn Research Center and a Hall Thruster operating at Princeton University.

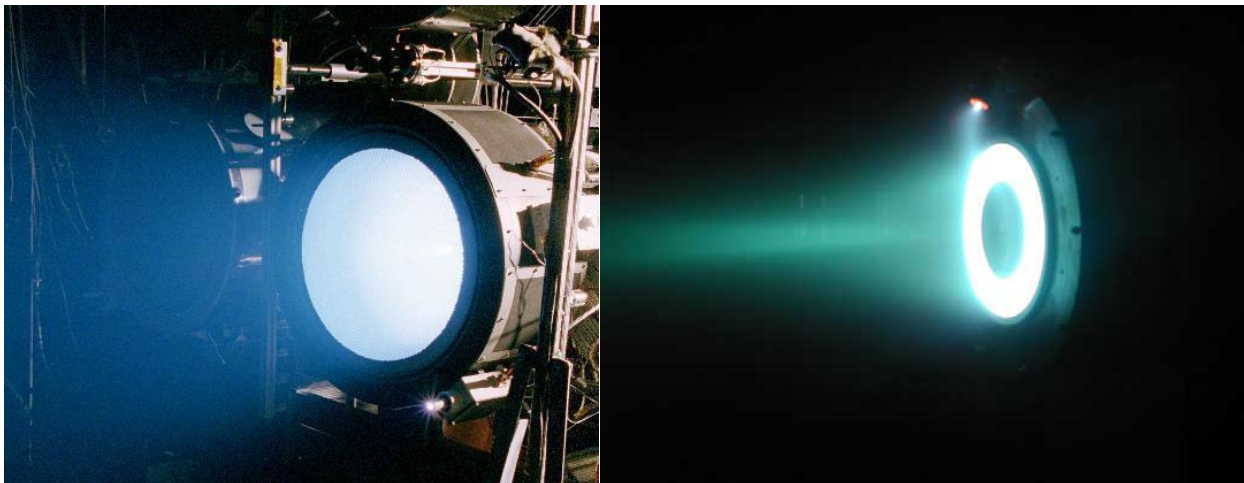


Figure 1. Left, the NEXT Ion Thruster at NASA's Glenn Research Center. Right, a 2 kW Hall Thruster operating at Princeton Plasma Physics Laboratory.

For both thruster types, the lifetime of the engine is critical, as they are expected to operate continuously for years or longer. Thus, the failure mechanisms of these engines must be investigated.

1.2 Sputtering Basics

When an energetic particle such as an ion strikes a material surface, the energy deposited by the particle into the atoms of that material causes a series (one or more) of collisions called a “collision cascade”. If the amount of energy is high enough, the result of the collision can be an ejected or “sputtered” particle leaving the surface. The sputtering process is critical to electric propulsion applications because this slow erosion of material due to ion impact is a primary lifetime limiting factor for ion and Hall-effect thrusters².

1.2.1 The Sigmund Equation

In 1969, Sigmund³ published his “Theory of Sputtering”, which has become the basis for most sputtering models. In his publication, Sigmund presents a theoretic equation for total sputter yield $Y(E)$

$$Y(E) = \frac{3\alpha T_m}{4\pi^2 U_0} \quad (7)$$

where α is a mass-dependent function, T_m is the momentum transferred by the impacting ion, and U_0 is the surface binding energy of the target particles.

Additionally, Sigmund predicted an angular dependence of sputtering yield that was diffuse and axisymmetric in nature

$$y = \frac{Y}{\pi} \cos(\alpha) \quad (8)$$

with Y being the total yield and y being the yield at a polar angle α above the target. Note that α in equation (8) is not the same parameter as α in equation (7). While these equations were revolutionary in nature, they assume complete isotropy of the sputtered particle velocities, many atom collision cascades, and normal (not glancing) ion impacts with atoms.

The elements of these equations are derived from both Collision and Transport theory. Starting from the assumption of an infinite surface of sufficient thickness to neglect the possibility of energy loss from the opposite side, the target atoms are held together with a binding energy U_0 . Incoming ions from the ion source will strike the surface with an energy E . Since the surface is not simply a solid wall, but rather a collection of bound atoms, the target particles will have a collision cross section, usually expressed differentially as $d\sigma$, and which is a function of initial ion energy E and transferred energy T . The total cross section will be the integral of this differential cross section over all solid angles. The maximum energy which can be transferred in this collision will be T_m ,

$$T_m = \frac{4M_1M_2}{(M_1+M_2)^2} E \quad (9)$$

where M_1 is the mass of the incoming ion and M_2 is the mass of the impacted atom. The cross-sections of the target atoms present a “nuclear stopping power” or the

ability for the target atom to reduce the velocity of the incoming ion. This stopping power is denoted $S_n(E)$, and is a function of the mass (M) and atomic number (Z) of the ion and target atoms, as well as the Coulomb interaction between the two ($s_n(\varepsilon)$).

$$S_n(E) = 4\pi\alpha Z_1 Z_2 e^2 \frac{M_1}{M_1+M_2} s_n(\varepsilon) \quad (10)$$

The collision parameters of the target material can be gathered together in a single function $F_D(E, \theta)$, in which α is a dimensionless function of mass ratio and impact

$$F_D(E, \theta) = \alpha N S_n(E) \quad (11)$$

angle θ , and N is the density of the target material. Further, the sputtering properties of the target material can be gathered into a function Λ ,

$$\Lambda = \frac{3}{4\pi^2} \frac{1}{N C_0 U_0} \quad (12)$$

in which the value C_0 is described below, with λ_0 and the Thomas-Fermi screening radius a_{BM} determined from the Born-Mayer potentials of the target.

$$C_0 = \frac{\pi}{2} \lambda_0 a_{BM}^2 \quad (13)$$

With these two parameters described, the total sputter yield Y can be addressed as

$$Y = \Lambda F_D(E, \theta) \quad (14)$$

for low ($\lesssim 10$ keV) energy sputtering. Algebraic manipulation of (14) yields equation (15).

$$Y = \frac{3}{4\pi^2} \frac{\alpha S_n(E)}{C_0 U_0} \quad (15)$$

which is easily converted into equation (7) using the definitions of the nuclear stopping power and the coefficient C_0 .

1.2.2 Evolution of Model Equations

In 1980, Matsunami⁴ updated equation (7). Matsunami's Equation (16) incorporates a threshold energy (E_{th}) below which sputtering does not occur. Note that the constant 0.042 is the calculated value of $\frac{3}{4\pi^2 C_0}$, assuming $\lambda_0 = 24$ and $a_{BM} = 0.219 \text{ \AA}$ (from Born-Mayer potentials) for all materials.

$$Y = 0.042 \frac{\alpha}{U_0} S_n(E) \left[1 - \sqrt{\frac{E_{th}}{E}} \right] \quad (16)$$

In this equation, U_0 is estimated as roughly the sublimation energy of the target. This improvement yielded good predictions at high ion energies (>1 keV), and much better predictions at low (<1 keV) ion energies. Then, in 1996, Yamamura & Tawara⁵ produced a table of values for monatomic solids using equation (16). Additionally, the duo fitted an equation to non-normal incidence sputter yields, creating the first widely-accepted non-normal ion incidence equation (17).

$$Y = y(0) \cos(\beta)^{-f} e^{-\Sigma \left(\frac{1}{\cos(\beta)} - 1 \right)} \quad (17)$$

This equation would likewise be calculated from a table of values provided in their paper. For equation (18), $y(0)$ is the total yield at normal incidence, β is the ion incidence angle, and f and Σ are defined in (18a) and (18b),

$$f = f_s \left[1 + 2.5 \left(\frac{1-\xi}{\xi} \right) \right] \quad (18a)$$

$$\Sigma = f * \cos(\theta_{opt}) \quad (18b)$$

where f_s is a fitted parameter provided in the tables, and ξ and θ_{opt} are further calculated from the following equations,

$$\xi = 1 - \sqrt{\frac{E_{th}}{E}} \quad (18c)$$

$$\theta_{opt} = 90 - (286 * \Psi^{0.45}) \quad (18d)$$

with E_{th} and Ψ as further fitting values from the tables. Each fitted parameter is specific to a particular ion-target combination.

Independently of Yamamura & Tawara, Bohdansky⁶ additionally created a predictive equation for normal incidence yields which was more accurate at lower energies. In equation (19), k is a fitting parameter based on the total yield at normal incidence.

$$Y = k \left[1 - \left(\frac{E_{th}}{E} \right)^{\frac{2}{3}} \right] \left[1 - \frac{E_{th}}{E} \right]^2 \quad (19)$$

1.3 The Role of Sputtering in Electric Propulsion

Sputtering is the primary life-limiting factor in electric propulsion. For engines which are expected to function for years without stopping, the slow, steady erosion of charged grids or thruster channel walls will eventually cause irreversible damage.

Figure 2 is a picture of a Hall Thruster after 500 hours of continuous operation.

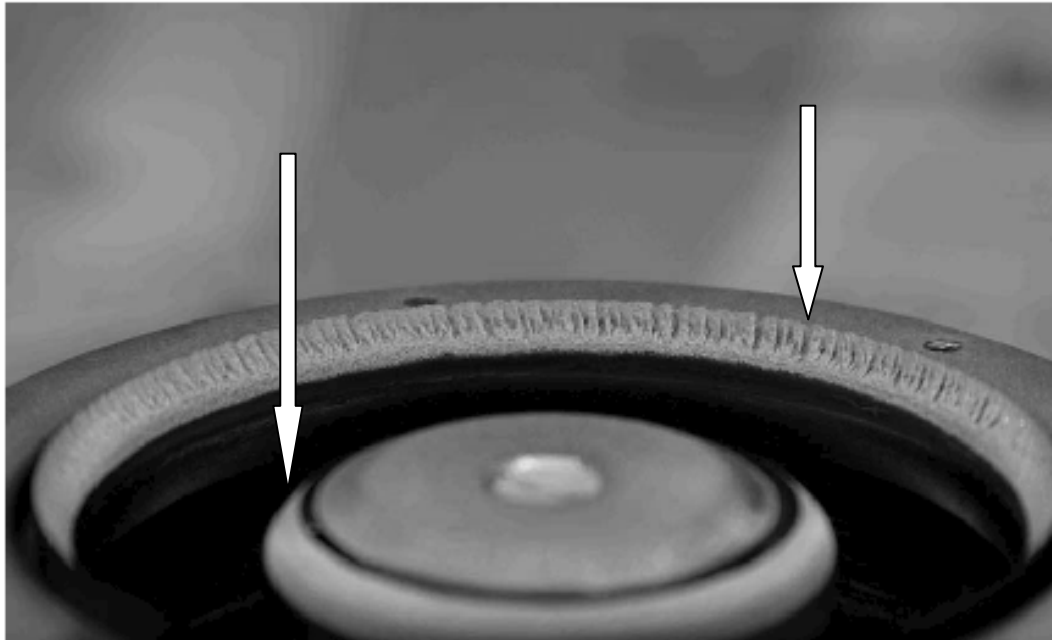


Figure 2. A Hall Thruster after 500 hours of operation at Keldysh Research Center⁷. Erosion is visible along the insulator channel wall.

In addition to limiting the longevity of these thrusters, sputtering sends eroded particles out from the engine where they may collect on and contaminate other surfaces, eventually causing failure of any systems on which the particles accumulate. Lifetime tests of these engines are costly and exceedingly lengthy; if the engine will run for 10 years, then a lifetime test takes many tens of thousands of hours perform. For this reason, models have been developed to predict the effects of sputtering, but most of these are missing critical data at very low energies, where most sputtering inside a Hall Thruster takes place as shown in Figure 3. To that end, the research performed herein will contribute to filling this gap for one of the most common materials in electric thruster design: Boron Nitride.

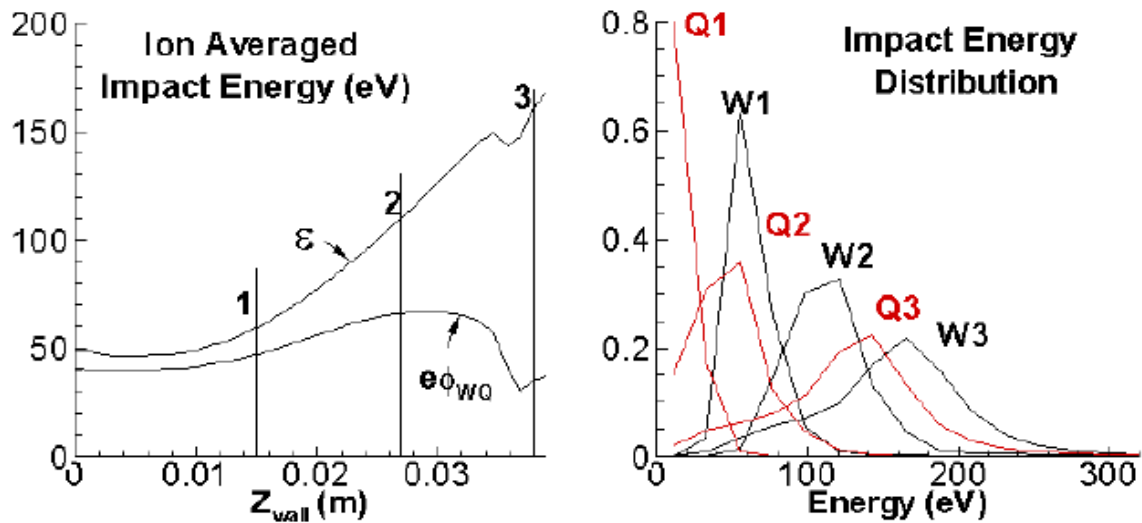


Figure 3. Ion impact energy distribution in the thruster channel for 1 kW Hall Thruster⁸.

1.4 Boron Nitride in Hall-Effect Thrusters

Hall-effect thrusters use insulator materials for the thrust channel walls. While there are many options of usable materials, typically Boron Nitride or Boron Nitride composite ceramics are used, largely due to their low sputter yields. These insulator ceramics line the thruster channel walls to allow the electric field to exist in the channel and protect the inner and outer structure of the thruster, in particular the magnets which create and maintain the Hall-effect. Because of the shape of the thruster channels and the nature of the electric and magnetic fields inside, the heaviest sputtering occurs near the exit plane of the thruster⁹, as shown in Figures 2 and 4.

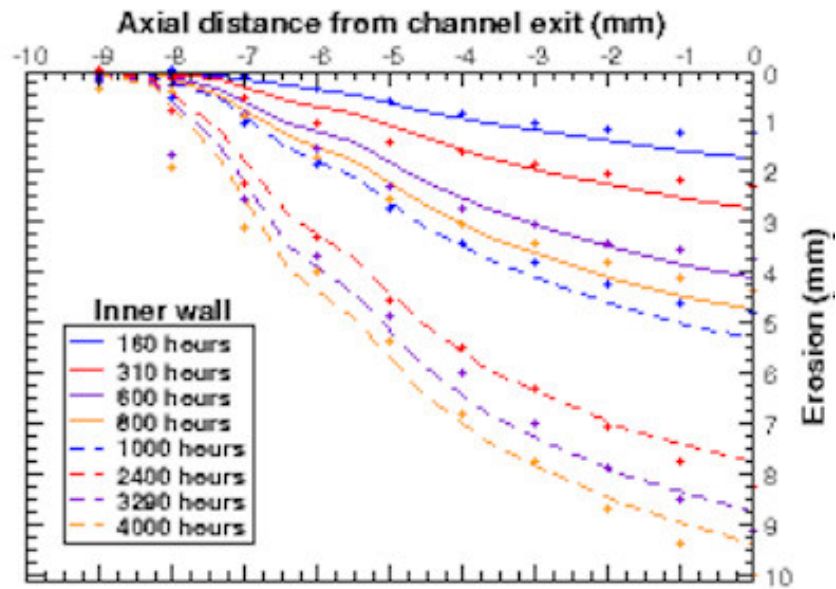


Figure 4. Erosion near an SPT-100 Hall Thruster exit plane⁹.

From figures 3 and 4, it can be concluded that ions with ~ 150 eV or less cause nearly a centimeter of erosion at the thruster exit plane over the course of 4000 hrs, or about half of one year. For an engine expected to run for many years, this suggests that several (and possibly tens of) centimeters would be eroded away, prohibitively damaging the thruster. Thus, understanding the mechanisms by which this erosion occurs at these ion energies will considerably improve the ability to design around this problem.

1.5 Sputter Measurement Techniques

Since the first concepts of sputtering were proposed, many techniques have been developed to study its effects, both in terms of sputter yield and of surface morphology. The first test specifically directed towards sputtering was performed by Goldstein¹⁰ in 1902, in which a cathode was pointed toward a gold film. The test was performed visually: the film disappeared over time. In 1908, Stark¹¹ initiated the concept of a “sputtering event”, which led to the idea of a collision cascade. Once sputtering was understood as an atomic event, more scientific means of measurement became of interest. One of the earliest and simplest methods is weight loss, wherein the target is weighed before and after sputtering. Rutherford backscattering allowed detection of much smaller amounts of sputtered particles by post-test observation of a deposition surface. As the understanding of electromagnetism improved, instruments such as the mass spectrometer came into use. With the advent of lasers, several techniques including laser-induced fluorescence (LIF) and cavity ring-down spectroscopy (CRDS) came into existence. Finally, as the precision with which a crystal can be cut increased, the quartz crystal microbalance (QCM) came into use.

1.5.1 Rutherford Backscattering

Rutherford backscattering (RBS) allows surface composition or structure analysis through detection of scattered ions. Typically, light ions such as He^{+2} or H^+ are

directed at a target from a particle accelerator. These ions are accelerated to the MeV range, and, upon striking the target, reflect off at a specific angle and with a specific energy based on the local surface topography and composition. By measuring the reflected angle and energy of the incident ion, it is possible to determine the mass (and thus the composition) of the target using

$$E = \left[\frac{M_1 \cos \phi + \sqrt{M_2^2 - M_1^2 \sin^2 \phi}}{M_1 + M_2} \right]^2 E_0 \quad (20)$$

where E is the residual energy of the ion, E_0 is the incident energy of the ion, ϕ is the ion reflection angle, and M_1 and M_2 are the incident ion and target masses respectively¹². A target is sputtered with an ion beam, then analyzed with RBS spectrometry to determine film thickness, from which deposition rate (and hence sputter yield) can be determined. Shutthanandan¹³ used this technique to measure sputter yields. Compared to other spectroscopic methods such as Auger Electron Spectroscopy (AES) or X-ray Photon Spectroscopy (XPS), RBS is lacking in sensitivity and depth resolution, but eliminates the concern of secondary sputtering while performing the analysis, which can negatively impact results.

1.5.2 Mass Spectrometry

The Lorentz Force (Eq. 4) coupled with time-of-flight measurements govern the detection of sputtered particles in a mass spectrometer. During testing, a mass

spectrometer is placed at some angle relative to the target (which corresponds to the angle α in the current QCM study). The target is sputtered as normal, at which time some of the sputtered particles drift into the mass spectrometer aperture. The particles are ionized by filaments, and then pass through an $\vec{E} \times \vec{B}$ filter channel. Governed by the Lorentz Force, the particles can be mass-selected (through the force $\vec{F} = m\vec{a}$) by cycling the electric or magnetic field strengths. A detector at the end of the channel counts particles. With the number of particles and their respective masses known, the sputter yield can be determined. Mass spectrometry can be used to determine sputter products using the same method. The composition of an unknown particle of mass M can be identified based on its mass as determined by the crossed electric and magnetic fields. Wucher and Reuter¹⁴ used this method to determine sputter yields, as did Oyarzabal *et. Al.*¹⁵.

1.5.3 Laser Techniques

Of the host of laser measurement techniques, LIF and CRDS are among the most common. To detect particles with a laser, one must first identify a useful transition wavelength. Since most particles have different spectral lines, a different laser is typically needed for each material of interest, which can rapidly become very expensive. However, once a spectral line is selected, laser measurements can detect part-per-billion to part-per-trillion quantities of particles, giving them orders of magnitude higher sensitivity than most other methods.

Once a spectral line has been selected and an appropriate laser chosen, there are two fundamental ways to detect the particles themselves. With LIF, the laser is injected into the path of the sputtered particles. When a particle passes through the beam, it absorbs a photon and reaches an excited state. Particles which do not share the spectral line pass through the beam to no effect. Once the sputtered particle has been excited, it very quickly releases a photon to return to the ground state. A very sensitive detector such as a photomultiplier tube is then used to detect the released photons, giving a particle count. In vacuum, typically the quality of the detector is the limiting factor for particle detection. At higher pressures, scattering rapidly becomes of greater significance. Larger sputter yields also mean stronger signals, and conversely, smaller sputter yields result in weaker signals, making high-quality detectors even more important in laser sputter detection.

With CRDS, the chosen laser is injected into a cavity formed by two high-reflectivity mirrors (>99.9%).

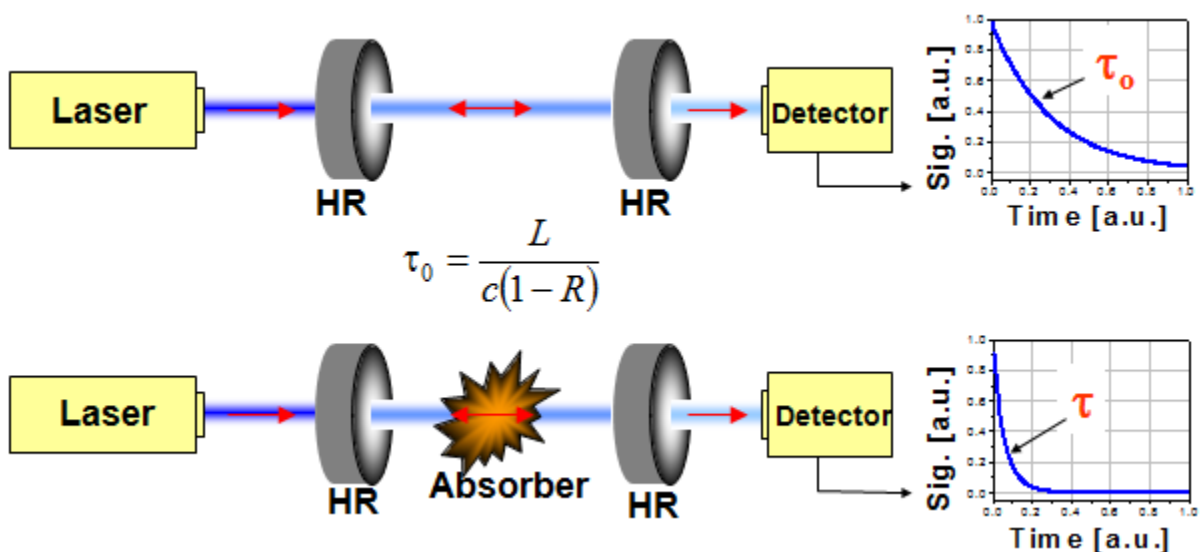


Figure 5. CRDS schematic¹⁶.

The laser beam reflects tens of thousands of times between the mirrors before eventually decaying to zero, effectively increasing the path length that the laser travels through by several orders of magnitude. When the cavity is empty (*i.e.* in vacuum), the light decays with a time constant τ_0 . This decay is called a “ring-down”. When the target particles (called “absorbers”) are present in the cavity, the decay rate is accelerated because some of the light is absorbed during each reflection. This generates a new decay time constant τ , which can be compared to the empty cavity time constant to generate a particle number density in the cavity. It is important to note that neither method presented here can provide information on the emission direction of the sputter products, only the total number emitted.

2. Experimental Setup

In this chapter, the vacuum chamber in which these experiments are conducted, the measuring devices, and the supporting equipment are described in greater detail.

2.1 Measurement System Overview

The QCM system consists of three principle components: a vacuum chamber in which the QCM itself resides and inside which experimentation is performed, a power cabinet which holds all power supplies needed to run the QCM systems and which allows the user to control the ion source, and the data acquisition system including a Sigma Instruments QCM Controller connected to a laboratory PC which receives and records the QCM signal, processes the initial data, and contains a control feedback system which adjusts the QCM system as needed during experimentation. Figure 6 is a photograph of the measurement system.

Attached to the vacuum chamber is a Leybold-Heraeus D30A roughing pump capable of bringing the chamber from atmospheric pressure to the cryogenic pump crossover pressure of 0.1 Torr in approximately 15 minutes. Adjacent to the

roughing system is a CTI-8 cryogenic pump with a 1500 liter/s pumping speed which provides a chamber background pressure of 5×10^{-7} Torr and maintains a working

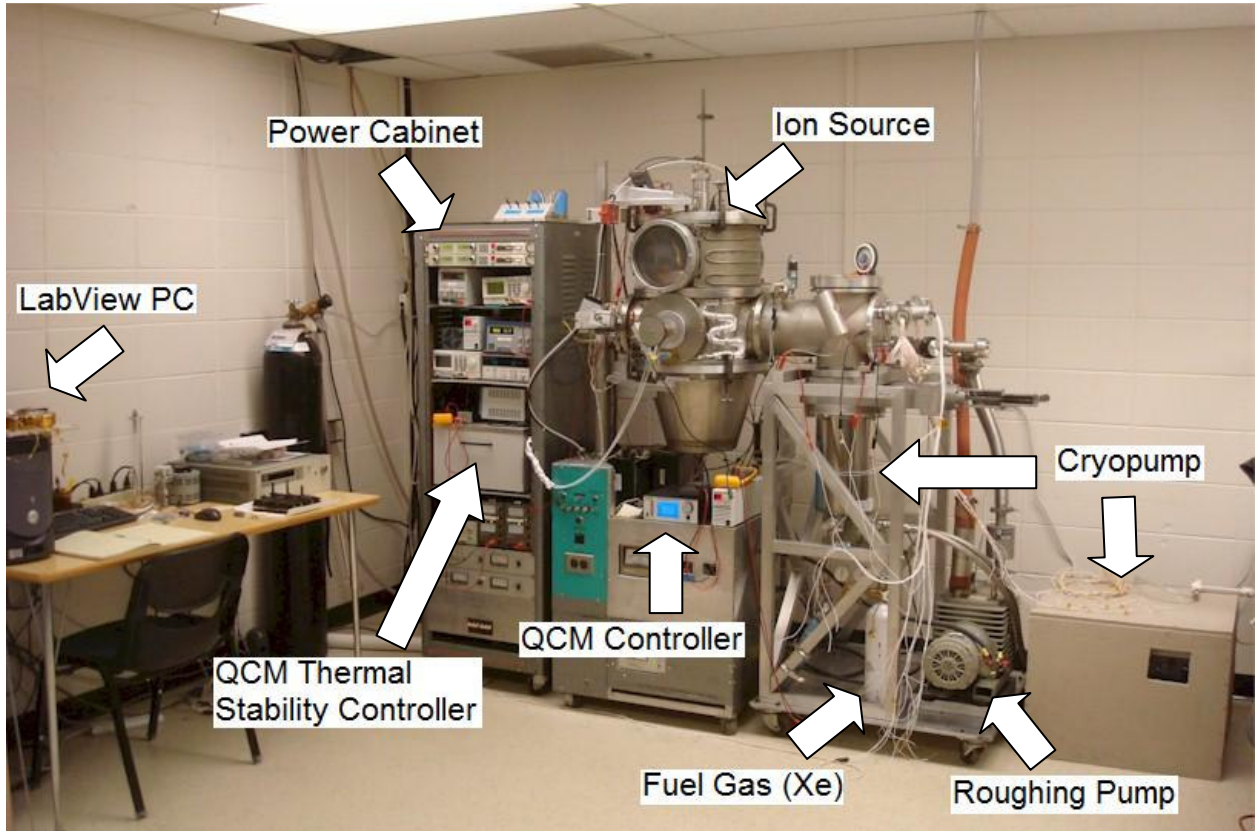


Figure 6. QCM measurement system. Major components are labeled.

chamber pressure of between 5×10^{-5} and 1×10^{-4} Torr for Xenon gas flow. A Residual Gas Analyzer (SRS RGA100) showed the primary contaminants to be N_2 at 2×10^{-7} Torr, followed by H_2O at 1.2×10^{-7} Torr.

The main section of the chamber is 43 cm in diameter and 76 cm tall, yielding a total chamber volume of approximately 0.125 m^3 . The top section contains a DC-Kaufman ion source (oriented vertically downward), the central section has the QCM itself and the sample target and a 15 cm x 15 cm holder 23 cm downstream from the ion source, and the bottom section contains the rotary feedthrough for

the sample target holder. The arm on the right of figure 5 has the cryopump, the roughing pump, and several electrical feedthroughs.

The mechanical rotary feedthrough in the bottom section of the chamber allows the sample target holder to be rotated in the ϕ -angle (see fig. 7). It consists of a 50 cm long rod that attaches at the top to a screw-clamped bracket at the base of the target holder and at the bottom (outside of vacuum) to a 25000 step stepper motor (Parker Compumotor).

In the central section of the chamber, a second rotary feedthrough connected to another Parker Compumotor turns the QCM arm through its range of angles. The feedthrough shaft also contains two water lines, used to thermally stabilize the QCM itself (see section 2.6).

2.1.1 Definition of Angles

The following system is used to define the angles involved in this research project. β is the ion beam incidence angle relative to target surface normal, with $\beta = 0$ for normal incidence. α is the polar angle of the sputtered particles with respect to surface normal. ϕ is the sputtered particle azimuthal angle measured in the plane of the target surface such that $\phi = 0$ is the forward direction. Figure 7 illustrates these angles. All angles are initially recorded in the data acquisition system in the target normal reference frame, then converted as needed to the target reference frame during the analysis portion of the data handling.

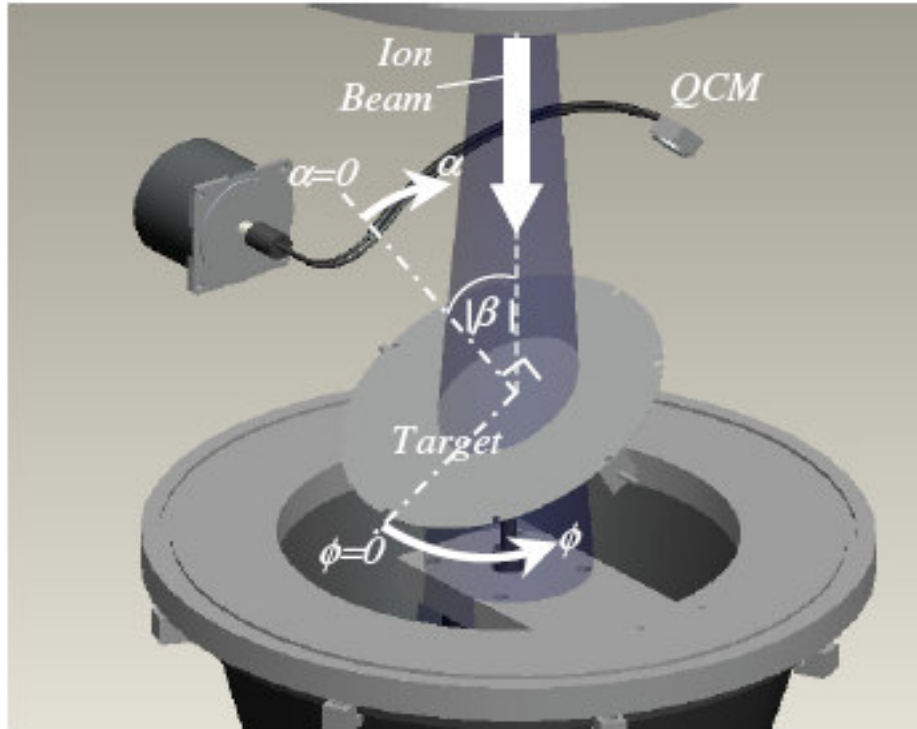


Figure 7. Solid model of QCM with angle definitions.

2.2 Quartz Crystal Microbalance

The QCM operates on the principle of resonance frequencies. A piezoelectrically active crystal is stimulated to vibrate at its resonance frequency, while an analogue signal measuring this frequency is returned to a controller. Changes in the resonance frequency of the crystal can be converted into changes in the mass of the crystal due to particle accumulation. However, the crystal is sensitive to temperature changes (noise frequency equivalent to hundreds of nanograms for temperature changes of a few degrees) requiring thermal control of the system, which will be discussed in section 2.7.

2.2.1 The Sauerbrey Equation

In 1959, Sauerbrey¹⁷ developed an equation to relate the oscillation frequency of a piezoelectric crystal to a mass change of the crystal

$$\Delta f = -\frac{2 \cdot \Delta m \cdot f^2}{A \sqrt{\rho_q \mu_q}} \quad (21)$$

where Δf is the frequency change, Δm is the mass change, f is the resonant frequency of the quartz crystal, A is the piezoelectrically active surface area, ρ_q is the density of quartz, and μ_q is the shear modulus of quartz. The use of this equation requires that frequency changes be small ($\Delta f/f < \sim 0.05$), and that the crystal be oscillating with negligible ambient viscous effects. During QCM testing, each measurement taken covers a frequency change of roughly 0.5 Hz, with a resonant frequency of 6 MHz. Additionally, all measurements are taken in vacuum, where the ambient viscosity is zero. Therefore, the use of the Sauerbrey equation is fully justified.

Since the QCM frequency is measured with a resolution of 0.001 Hz, and using 2.648 g/cm³ as the density of quartz and 2.947x10¹¹ g/cm·s² as the shear modulus for an AC-cut crystal, the minimum mass change detectable on the QCM is approximately 6 picograms. In practice, thermal noise in our system currently limits detection to the nanogram range, although this can be mitigated by waiting longer to increase total accumulation on the crystal (discussed in further detail in sections 2.3 and 2.7).

2.2.2 Quartz Crystal

The primary component of the QCM is the quartz crystal inside. This crystal is very precisely cut along a crystallographic plane inside a larger quartz crystal. Several grades (cuts) of crystal are available commercially: AT, RC, and SC, named for the crystal axis on which they are cut. Each type has specific properties, and care must be taken when selecting a crystal to match the experimental operating conditions (some details are discussed below). The crystal is piezoelectrically stimulated to vibrate at its resonant frequency with a pair of small gold electrodes. As the mass of the crystal changes, due to sputtered particles either depositing on the surface or coming off the surface, the resonance frequency changes. However, the crystalline structure of quartz also carries a vulnerability to thermal shock as well as stresses caused by impinging particles. Certain cuts of crystal are less vulnerable to these effects, however cost can rapidly become a major issue. AT-cut crystals are thermally compensated, with an inflection point in their thermal profile near room temperature¹⁸. This means that if they are maintained near room temperature during testing, thermal fluctuations in the QCM signal will be minimized. SC-cut crystals are stress-compensated, reducing their reaction to impinging particles during sputtering¹⁹. They also have a reduced vulnerability to temperature, with an inflection point near 92°C. However, they are very expensive. RC-cut crystals are a variant of the SC-cut, and were selected for use at Colorado State University, due to their high sensitivity, low thermal noise, and lower cost. The

signal from an RC-cut crystal is optimized near 92° C, reasonably close to the ~80°C at which most testing occurred.

2.2.3 Measurement

When an ion beam strikes the surface of a target and sputters particles, these particles may leave at a wide variety of angles from the surface. Differential sputter yields (discussed in depth in sections 3.1 and 4.4) are measured by examining the volume of particles which leave the surface at a given angle. By placing the QCM at a particular polar angle α over the target surface, a measurement of the differential sputter yield in that direction is taken. When these point measurements are taken at many polar angles over the target, a yield *per steradian* profile is generated. All of the particles which leave the surface and travel inside the 5.4 steradian viewing cone of the QCM²⁰ crystal strike the QCM itself. It is important to note that just because a particle strikes the QCM does not mean that it sticks to it. However, for most of the materials under investigation in this study, these sticking coefficients (the ratio between total particles which remain stuck to the surface and total impacting particles) are near unity²¹ once a layer of at least a few tens of angstroms of the material has been deposited on the crystal. This assumption can be further validated through comparison between the QCM measured total yield and the weight loss measured total yield. If the sticking coefficient is near 1, then the two measurements should agree. It is also important to note that only condensable components of the sputtered products can stick to the QCM. Gaseous particles such as N or N₂

sputtered from Boron Nitride will not stick to the QCM (sticking coefficient of nearly 0). Because of this, calculation of a QCM-based true total sputter yield (referenced to the target) is

$$Y_{Total} = Y_{QCM} \left[\frac{M_1 + M_2}{M_1} \right] \quad (22)$$

with Y_{Total} the true total sputter yield, Y_{QCM} the QCM measured total sputter yield, M_1 the condensable particle, and M_2 the non-condensable particle. This equation as written is for a two-component sputter product, but can be easily adapted for other multi-component products.

2.3 Data Acquisition

During sputter testing, the signal from the QCM is recorded at a rate of just less than 1 Hz. This signal passes from the QCM out of the chamber and into the QCM controller (Sigma Instruments), which converts the signal into a measurement in the units of $\frac{g}{s}$. A LabView-based program (written in-home) displays this data for in-test monitoring, as well as recording each point with its time stamp and QCM position values to an Excel Spreadsheet.

In a given test, the QCM position is also controlled by the LabView program. At the beginning of the test, the QCM arm is rotated to its zero position (approximately 120° from the ion incidence direction). The program launches by moving the QCM to its first polar angle and waiting for a predetermined length of

time to reach thermal equilibrium (further discussed in section 2.7). Once thermally stable, the program begins recording a specified number of data points. After these points have been collected, the program moves the QCM to its next polar location. The process is repeated for each polar angle α in this sweep. After completing the last position, the QCM is rotated back to its zero position and, if desired, the program rotates the target in the azimuthal direction. The entire program to this point is then repeated for each desired azimuthal angle φ .

A major source of error is thermal drift in the QCM signal (discussed further in section 2.7), however, this is mitigated through the process of data accumulation by waiting at each location until thermal stability has been reached. The remnant noise from the thermal fluctuations at this point is typically several orders of magnitude below the deposition signal from the sputtered target.

2.4 Ion Source and Four Grid Optics

2.4.1 Ion Source

A Kaufmann ion source²² generates the ions for target bombardment with dual thoriated tungsten filaments as a discharge cathode. A feed gas, usually Xenon, is passed through three inlets, two on the sides where the cathode wires connect, and one in the top center above the upper anode. The base of the ion source is designed to allow different sets of ion optics to be easily attached with minimal adjustments

to the system. Below the ion optics is a ground screen with a thoriated tungsten neutralizer filament (insulated from ground) which passes directly through the center of the beam. During operation, the neutralizer filament is biased at 25 V below ground to encourage electron emission from the filament into the ambient plasma. The current used to heat the filament is maintained such that the total filament emission current is at least 150% of the total beam current. Beam and sample neutralization studies have been performed and are presented in section 4.3.

2.4.2 Four Grid Ion Optics

Investigation into very low energy sputtering, the region from the sputtering threshold (~ 25 eV) to 100 eV, faces many challenges. At energies near the sputtering threshold these sputter yields by definition drop to near zero values, requiring extremely sensitive measurement devices to detect sputtered particles. Additionally, many ion sources cannot generate ion beams at $\lesssim 100$ eV, and those which can usually have very divergent and poor quality beams with low current densities. These conditions result in few ions striking the target surface, which in turn generates even fewer sputtered particles. To make accurate measurements with reasonable margins of error, improvements must be made to the ion source.

To this end, a four-grid ion source has been developed²³. Typical ion sources feature two grids; the (inner) screen contains the plasma and is biased positive with respect to ground, but negative of the anode. The (outer) accel grid draws the ions

out of the source through the many carefully aligned holes in the grids, generating an ion beam. The accel grid is biased negatively with respect to ground, and must be maintained at a voltage large enough to prevent electron backstreaming into the source, while being small enough to prevent ions from being accelerated into very divergent trajectories. This balance of voltage is often one of the largest factors in beam divergence – too negative and the beam divergence increases dramatically, too near zero and electron backstreaming occurs. At very low beam energies, this allowable range of voltages drops to nearly zero. Thus, two grid systems are not effective in generating high-quality, low-energy ion beams. To alleviate this problem, three grid ion sources employ a third grid just downstream of the accel grid²⁴. This extra grid is usually maintained at ground potential, and reduces the likelihood of electron backstreaming, lowering the minimum voltage allowable on the accel grid. Still, three grid systems usually falter below 200 eV²⁴.

In contrast, the QCM system utilizes a four grid system that employs a second accel grid which focuses the ion beam by keeping the electric field lines that the ions follow close to vertical with respect to the grid hole alignment axis. This ‘focus’ grid is then followed by a ‘decel’ grid, maintained at or near ground potential to prevent electron backstreaming. Figure 8 is the solid model of the ion beamlet simulated by the FFX code.

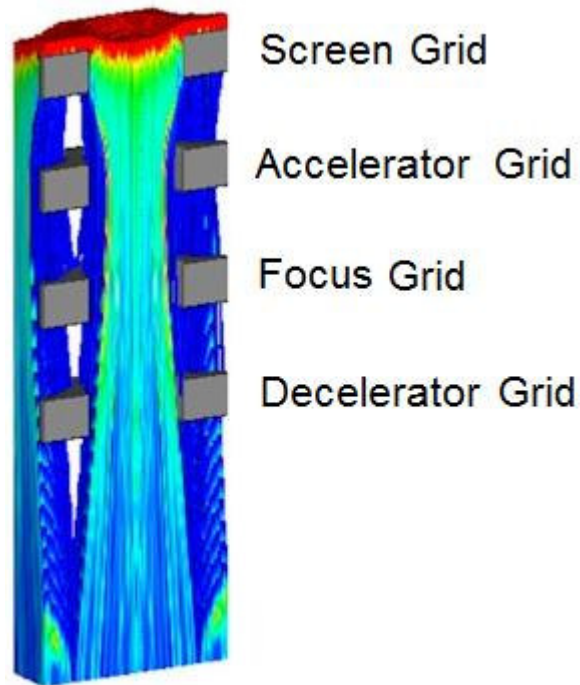


Figure 8. FFX simulation of a four grid ion beamlet. Grids are labeled.

2.4.3 Beam Profiling

Upon completion, the source was thoroughly profiled. First, the shape of the beam was measured using a system called the Multi-Axis Plasma Profiling System (MAPPS)²⁵. MAPPS is housed in a cryo-pumped vacuum chamber (vertical cylinder with a diameter of about 90 cm). The MAPPS device is a three-axis probe actuation system that measures current density with a Faraday probe. Profiles are acquired across 10-cm by 10-cm “x-y” planes orthogonal to the ion beam axis.

The Faraday probe consists of an outer body shell biased negatively to repel electrons and an inner collector plate biased positively to inhibit secondary electron ejection and collection of low energy beam plasma ions. Ions from the source pass

through a small hole that can be further reduced in size by a mesh placed directly beneath the body shell. Characterization of the probe led to an optimal bias on the body shell of -50 V relative to ground to minimize electron readings while simultaneously minimizing collection of non-sputtering ions. Internally, the collector plate bias was generally maintained at +30 V to ground. The probe was left unmeshed, with a hole diameter of 1.6 mm. Figure 9 is a picture of the MAPPS system.

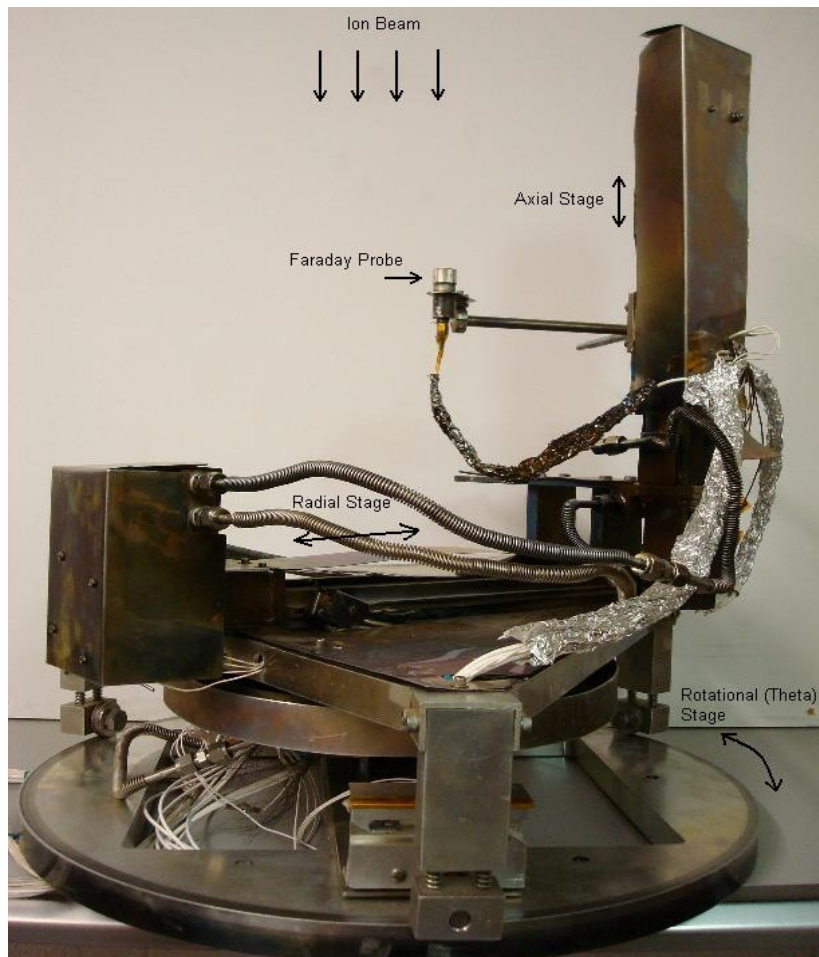


Figure 9. Photograph of the MAPPs system.

The MAPPS system was used both to profile the beam as well as to optimize the grid voltages, since this was the first time a four-grid source had ever been used at Colorado State. Once optimums had been found for the grid bias voltages, beam current densities were measured for multiple beam energies at a plane roughly 23 cm downstream of the source. Figure 10 provides examples of these scans.

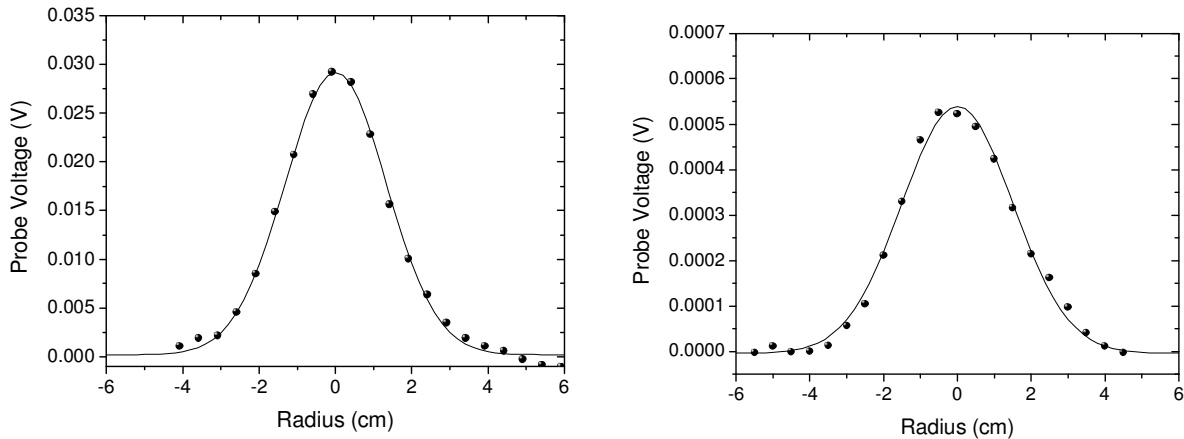


Figure 10. Left: 1-D Profile of a 250 eV beam at an axial distance of 16.3 cm from the ion source. Right: 1-D Profile of a 30 eV beam at an axial distance of 16.3 cm from the ion source.

2.4.4 Beam Characterization

Table 2 summarizes the ion source characterization data over a range of energies from 50 to 300 eV. The values measured are consistent with the FFX model²³, though the currents are slightly higher in some cases.

Beam divergence is an effect which occurs because the ion beam exiting the source is conical in nature, not cylindrical. Applied electric fields between and around the ion source grids strongly effect the divergence angle of the beam, either by collimating or further diverging the beam. Thus, every system will have an

Table 2. Ion source characterization data

Beam Voltage (V)	Extracted Beam Current (mA)	Accel Grid Voltage (V)	Focus Grid Voltage (V)	Decel Grid Voltage (V)	90% Beam Current Radius (cm)
300	5.0	-50	-100	0	4.3
250	3.9	-50	-100	0	4.2
200	3.8	-50	-100	0	4.3
150	2.8	-50	-100	0	4.4
100	2.1	-50	-100	0	4.2
75	1.5	-50	-100	0	4.2
50	1.0	-50	-100	0	4.3
30	0.7	-50	-100	0	4.0

optimum operating condition (grid voltages) with regard to beam divergence. For the system used in this experiment, the 90% width (diameter) of the beam was measured and found to be approximately 8.8 cm, much smaller than the 15 cm x 15 cm target. Although the fringes of the beam extend well beyond the edge of the target, measurements of total beam current reaching a conductive surface of the same size and shape as the target indicate that the current lost in the fringes is less than 5%.

For sputter measurements, the beam must strike only the target for two reasons. First, the measurement of beam current reaching the surface of the target is critical to calculating the total sputter yield. If a significant portion of the beam is passing to the sides of the target, this calculation becomes difficult. Second, the ion beam will sputter any surface it comes into contact with, including chamber walls, target holders, and instrumentation and feedthroughs in the path of the beam. The QCM cannot distinguish between particles sputtered from the intended target and

those sputtered from other sources. For this reason, the 90% beam current radius, that is, the circular radius which contains 90% of the beam current, is a key parameter. Since the targets that undergo sputtering are usually approximately 15 cm square, the beam used in these experiments fits easily on the targets. Beam current values are determined from the voltage across a resistor placed between the floating power supply and ground, and take current losses to the accel, focus, and decel grids into account. Integrated currents from the MAPPS profilometry should give similar values once charge exchange losses are accounted for, and indeed do for all conditions tested.

Further validation of the MAPPS profiles is found by examining the axial decay of the total current along the length of the ion beam. The total current should exponentially decay as the distance from the ion source increases, largely due to charge exchange collisions. Figure 11 provides an example of current versus axial distance for a fixed ion source condition (four grid source, $J_B = 4$ mA, $V_B = 250$ eV). The data are normalized to the initial data point, 10.3 cm from the ion source.

The expected charge exchange collision mean free path can be calculated as

$$\lambda_{CEX} = \frac{1}{n\sigma_{CEX}} \quad (23)$$

where n is the particle number density (from pressure and temperature measurements), and σ_{CEX} is the charge exchange collision cross-section. When calculated from equation 23, the mean free path λ_{CEX} was found to be 160 ± 80 cm, which is in good agreement with the measured value from the profiling data of

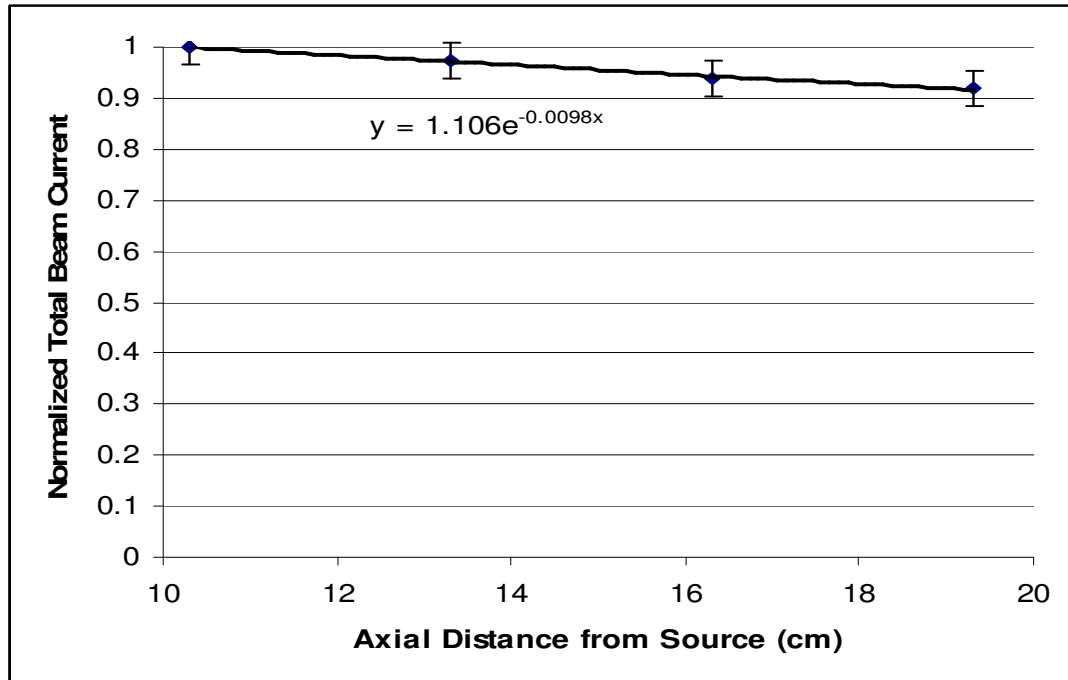


Figure 11. Exponential beam current decay due to charge exchange collisions and ion scattering.

102 cm (equal to $\frac{1}{0.0098}$ cm as shown in Fig. 11).

In addition to the shape profiling performed by MAPPs, the beam ion energy distribution was investigated through the use of a four grid Retarding Potential Analyzer (RPA). The RPA used for this profiling had an aperture diameter of 10.28 cm. This larger diameter allowed for more sensitive measurements in low-density plasma. Several ion energy distributions were measured. The peak of the distribution is located within 2 V of the beam voltage for all operating conditions, and beam full-width at half-maximums (the width of the beam at half of the peak voltage) were between 6 and 19 V, increasing with beam energy. Figure 12 shows these distribution functions for four operating conditions.

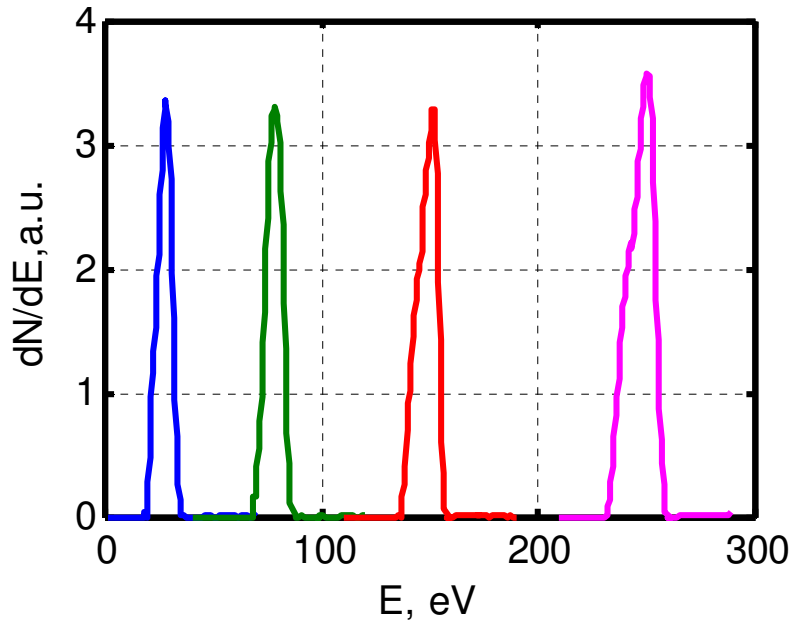


Figure 12. Four different ion energy distributions for beam voltages of 30, 80, 150, and 250 V (left to right).

Finally, measurements were made regarding ion species distributions. For this experiment, an $\vec{E} \times \vec{B}$ probe was used. This probe, also called a Wien filter, is a device that separates charged particles according to their velocity. The probe operates by using uniform crossed electric and magnetic fields, orthogonal to each other as well as to the particle velocity vector. A schematic of the probe is given in figure 13. Ions which pass through the collimator are subjected to the electric and magnetic fields. Ions with a particular velocity pass through these fields and reach a suppressor-collector at the other end. The suppressor works to inhibit secondary electron emission, making the measurements taken more accurate. During the measurements, the voltage in the electric field is swept and the collector current is recorded. In this way, particles of differing charges are filtered and detected. Figure 14 shows the results of this measurement. For beam energies above 80 eV, the

singles-to-doubles ratio was <5%. For beam energies below 80 eV, the singles-to-doubles ratio was nearly zero, possibly because the discharge voltage on the anode in the ion source was kept below the second ionization energy of Xenon.

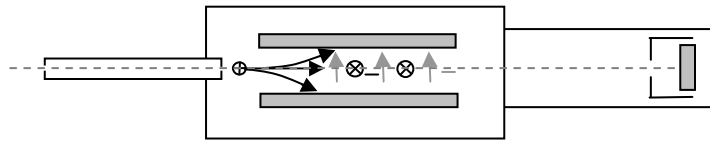


Figure 13. $\vec{E} \times \vec{B}$ probe schematic.

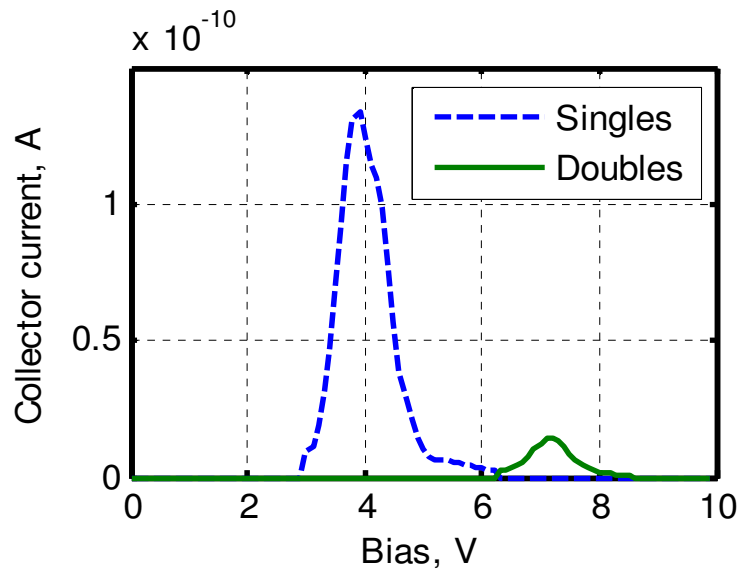


Figure 14. $\vec{E} \times \vec{B}$ Probe trace for a beam energy of 250 eV.

To determine the magnitude of the experimental error, conductive targets (typically Molybdenum) are placed at the same location as the sample targets and sputtered under the same conditions as the Boron Nitride targets. These conductive targets are insulated from their surroundings, and a single wire is attached to the underside of the target near the edge. This wire leads out from the vacuum chamber to a measurement point where a bias (-40 V), can be placed on the target and the

current striking the target can be measured. While this method neglects the effects of secondary electron emission, it has been shown that the typical fraction of secondary electrons emitted in a Xenon ion collision²⁶⁻²⁷ is less than 4%, well below the $\pm 15\%$ error margin calculated by current variations during a typical test.

2.5 Boron Nitride Test Samples

Since several grades of Boron Nitride exist, it is important to clearly identify which grade of the material is being tested. Three grades were chosen: HBC-grade Boron Nitride produced by GE-Advanced Materials²⁸, HBR-grade also produced by GE, and HP-grade Boron Nitride, manufactured by Saint-Gobain Ceramics²⁹.

2.5.1 Boron Nitride Purity

When manufacturing Boron Nitride, a binding material is frequently used. A binder can change the structure of the material, either to provide increased strength or increased hardness, to improve the machinability, change the thermal properties, or to adjust any other material characteristic. The addition of a binder can also affect the sputter yield of the material, as well as introducing adverse effects in vacuum testing situations. HBC Boron Nitride is a hot-pressed, diffusion bonded grade which does not use any binder, and has a purity of better than 99% (B+N). HBR-grade Boron Nitride is also hot-pressed and uses a Calcium Borate binder at 6% by volume. The use of Calcium Borate strengthens the material, but also induces moisture

absorption effects, which will be discussed in section 2.5.2. HP-grade Boron Nitride is considered a combat-grade material, and uses Calcium Borate as a binder at roughly 9% by volume. It also has a 3% porosity, which improves thermal shock resistance and conductivity, but dramatically increases atmospheric moisture absorption.

2.5.2 Moisture Absorption and Atmospheric Effects

When exposed to atmosphere, Boron Nitride can absorb moisture to varying degrees, depending on the grade. The HBR- and HP-grades of Boron Nitride contain a binding material (Calcium Borate), while the HBC-grade does not. The binder is believed to play a strong role in moisture absorption effects, although the exact mechanism is uncertain. The presence of moisture in the sample can lower the apparent sputter yield by changing the apparent mass loss. When the sample is first weighed, the moisture makes the mass appear higher. Once exposed to the ion source filaments the water evaporates, reducing the post-test weight measurement. Figure 15 is drawn from the Material Data sheet for Boron Nitride from GE Advanced Materials²⁸.

From this graph it can be seen that HBC and HBR grades of Boron Nitride can absorb up to 1% of their total weight in moisture from the air. In practice, the rate of absorption is heavily dependent on the humidity level, and so these values can change. Additionally, Boron Nitride samples are rarely left exposed to atmosphere for more than a couple of hours. However, Figure 15 does illustrate the need for

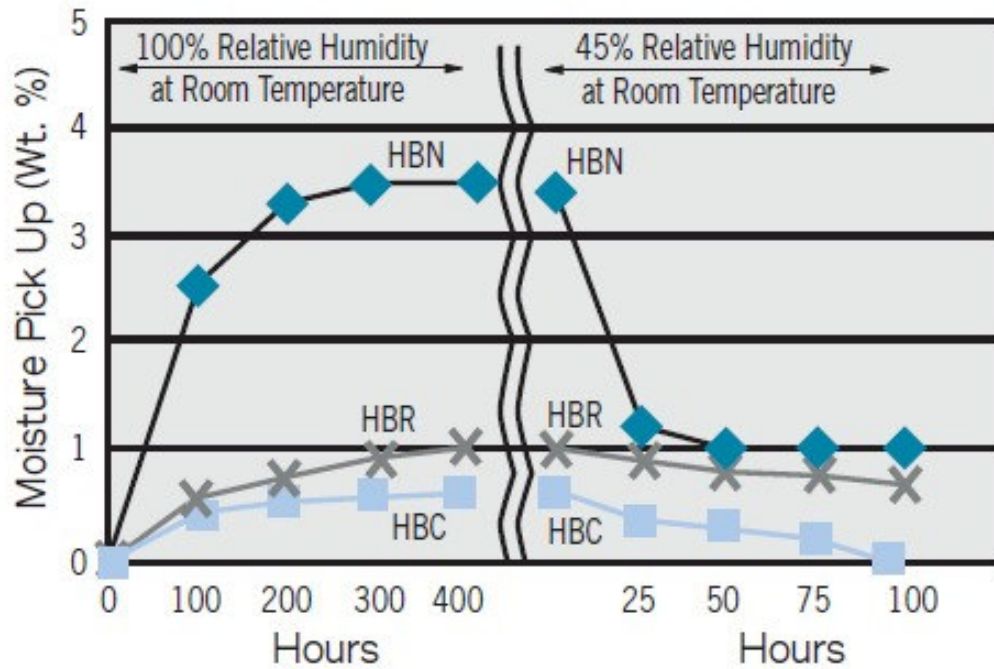


Figure 15. Moisture absorption for HBC and HBR grades of Boron Nitride.

bake-out procedures to remove moisture before testing. The HP-grade Boron Nitride used in this experiment did not include a moisture absorption data sheet. Experiments have produced Figure 16, demonstrating the mass gain with respect to length of exposure to atmosphere at between 20% and 40% humidity for the HP sample tested in the present work. Given that the total weight loss in a sputter test is on the order of 10 μg , within one minute of removal, the sample has gained at least that amount of mass due to moisture absorption. This precludes performing weight loss measurements on the HP-grade Boron Nitride until a method of counteracting these effects is developed. In practice, if the Boron Nitride samples have been exposed to atmosphere for longer than an hour, the samples are baked at $\sim 150^\circ\text{C}$ for at least a half hour. During this time, the chamber pressure is monitored

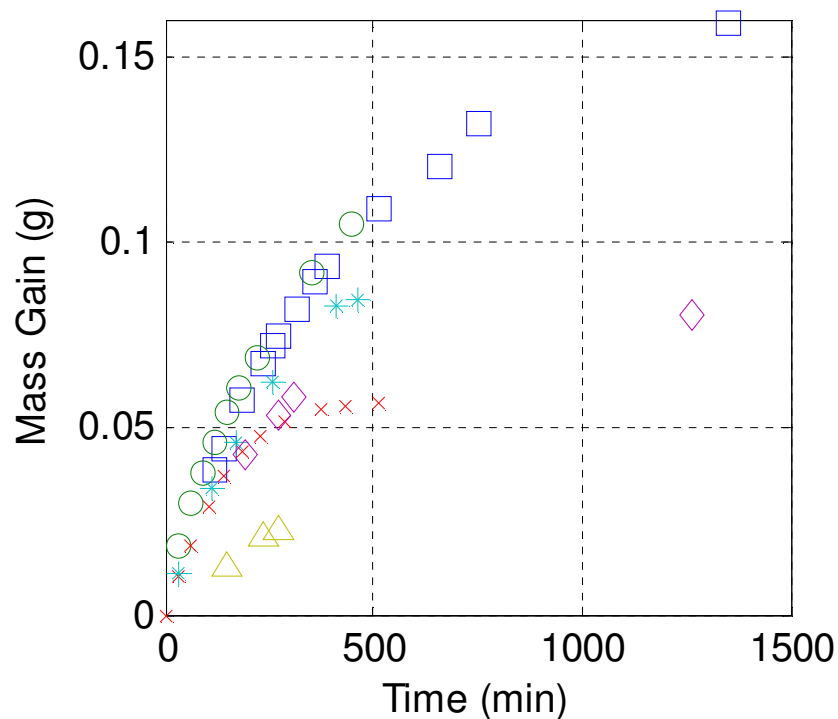


Figure 16. Mass gain of HP-grade Boron Nitride as a function of time of atmospheric exposure. Different symbols on the graph represent different test series. The starting sample mass is approximately 150 g. Time zero corresponds to 90 minutes after removal from the vacuum chamber.

to observe when outgassing from the sample ceases. If not accounted for, the absorbed moisture can dramatically change the (apparent) sputter yield of the material. Figure 17 shows the measured sputter yield of HBR Boron Nitride after about 1 hour of atmospheric exposure. The mass buildup due to moisture absorption was observed for all grades of Boron Nitride³⁰, and similar effects have been observed by other researchers³¹. The absorption appears to level off after approximately one hour with HBC- and HBR-grade Boron Nitride. It is important to note, however, that these post-experimental effects do not influence QCM measurements.

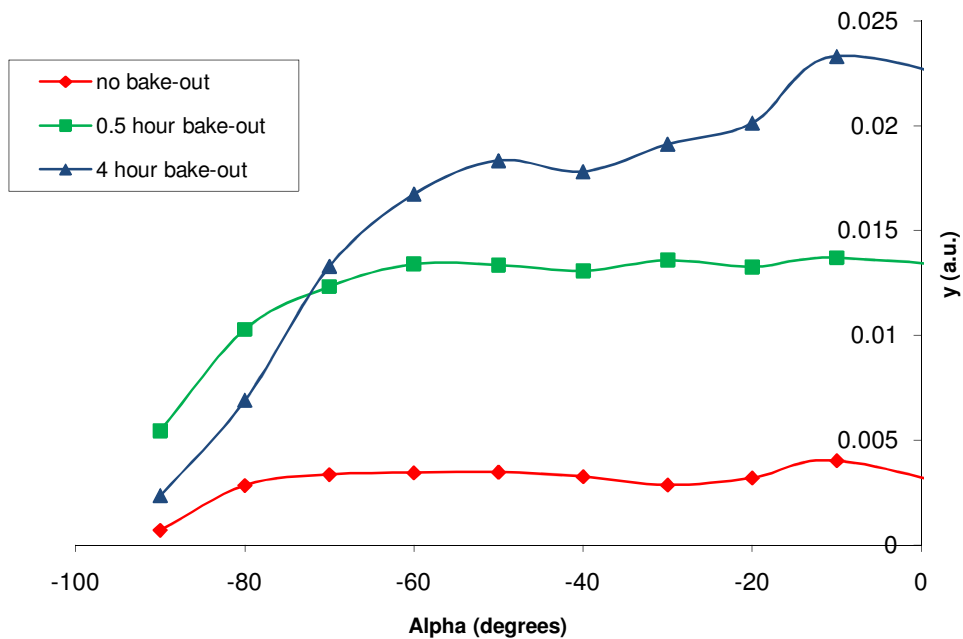


Figure 17. Measured sputter yields of HBR Boron Nitride after different bake-out procedures.

2.5.3 Surface Analysis

During sputtering, ions may preferentially sputter target particles from certain areas or faces of the target due to atomic structure³²⁻³⁴. Because of this, target surfaces evolve throughout the sputter test, and continue to evolve over multiple tests. As the target surface changes, on the microscopic level ions may begin striking at unexpected incidence angles or embedding into the target. Sputtered particles may redeposit on the target due to the formation of surface structures. These effects, though on the microscopic scale, can have a substantial effect on the overall test results, and as such, must be accounted for. A scanning electron microscope (SEM) has been used to investigate the Boron Nitride target surface before and after

sputtering. These images, shown in figure 18, demonstrate minimal target surface evolution over the course of 15 hours of sputtering by 250 eV ions.

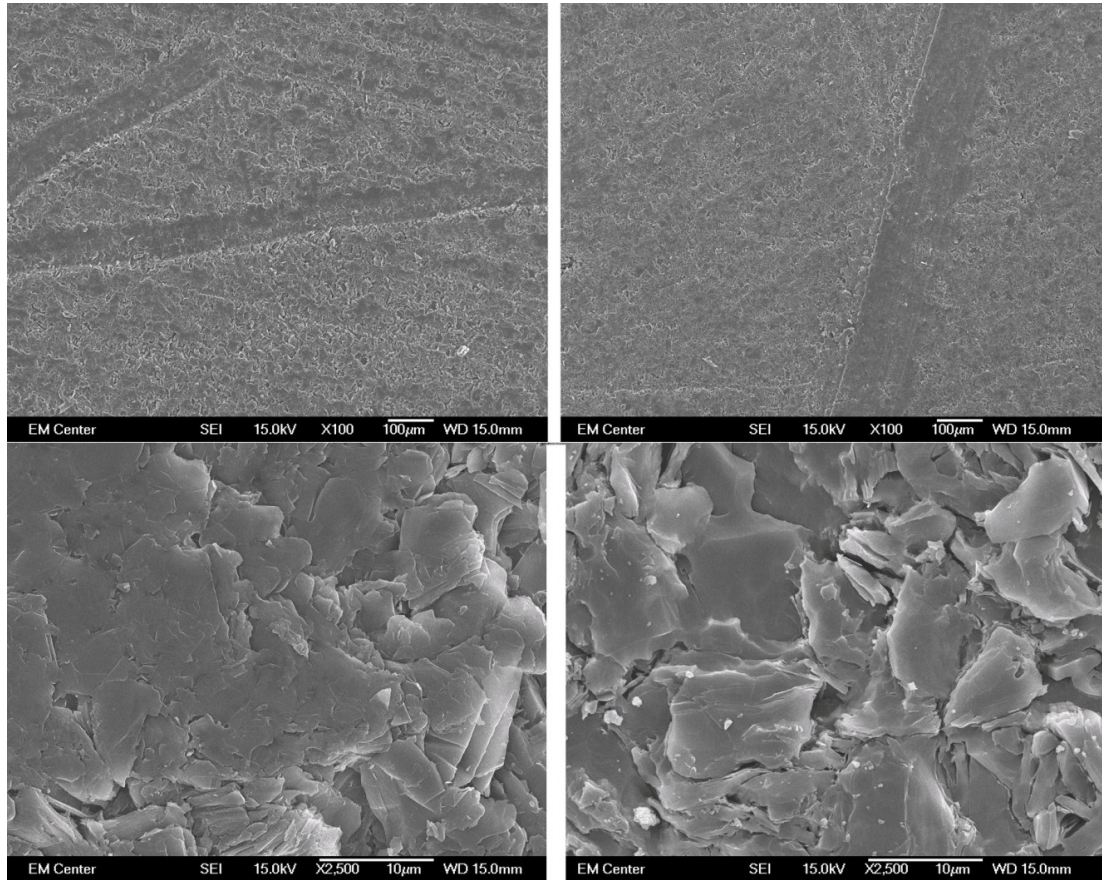


Figure 18. SEM images of HBC Boron Nitride surface. Left: Unspattered. Right: After 15 hour dose of 250 eV Xe^+ ions. The scale for the upper two images is 100 μm , while the lower image scale is 10 μm .

Due to the apparent lack of surface structure formation, it can be assumed that test results from this experimentation are negligibly affected by surface topography.

2.6 Weight Loss Measurements

Sputtering inherently changes the mass of the target being sputtered, so it is possible to calculate a sputter yield based on the target mass loss.

2.6.1 Procedure

Weight loss analysis can provide a highly accurate measure of the total sputter yield. However, weight measurements are vulnerable to effects such as moisture absorption and the formation of oxide layers on the surface of the target (see section 2.5.2), both of which artificially inflate the post-test mass, reducing the apparent sputter yield. With this in mind, the exposure to air by the targets must be carefully limited and controlled, or even eliminated. To this end, the following procedure is conducted when performing weight loss measurements.

First, the samples are placed into the vacuum chamber on the sample holder. Typically four 7.5 cm by 7.5 cm square samples are tiled together, since one 15 cm square sample will not fit on the scale used for this experiment. The chamber is pumped down to high vacuum. Once high vacuum has been achieved, the chamber filaments are all turned on, exposing the target to radiative heat. The sample is left to bake in vacuum for one hour or longer, depending on how much time the sample previously spent exposed to atmosphere. During this time, it is possible to observe the chamber pressure as read by an ion gauge. When the pressure settles to the expected chamber background pressure, it can be assumed that all outgassing by the target has been completed.

Next, the filaments are turned off and allowed to cool. Once the chamber (and target) has returned approximately to room temperature, the chamber is vented and the target is removed and weighed immediately. The weight measurements are conducted as quickly as possible without sacrificing accuracy, and usually take no

more than 5 minutes. Each 7.5 cm square target is weighed 3-5 times to ensure accuracy, and the weights are averaged to find a total target weight. The target is then immediately reinserted into the chamber and the chamber is pumped down to high vacuum. With this method, the total sample exposure to atmosphere between post-bake-out venting and post-weighing pump down takes less than 10 minutes. Once the chamber has reached high vacuum, the sputtering test is conducted.

After completing the sputtering test, the chamber is again allowed to cool to roughly room temperature, and is then vented. Immediately after venting, the target is removed and the same series of weight measurements as previously described are performed. If another sputtering test is to be performed, the target is immediately placed back into the vacuum chamber and the chamber is pumped to high vacuum. If not, the sample is stored in an air-tight bag, and moved into storage until the next time it is needed.

2.6.2 Ion Implantation

Another phenomenon that can influence weight loss measurements is ion implantation, specifically Xenon ions in this experiment. If a significant number of Xenon ions are implanted in the sample, their mass may affect the weight measurement and influence the apparent sputter yield. To check for this effect, X-ray Photon Spectrometry (XPS) analysis was performed on a sputtered sample of HBC-grade Boron Nitride. A previously unsputtered sample was exposed to a Xenon ion beam for 15 hours at 250 eV. The ion dose was approximately 3×10^{19} ions/cm².

The sample was then removed from vacuum and placed into the XPS system. The measured atomic fraction of Xenon with respect to electron emission angle is shown in figure 19. The test shows that the depth of Xenon penetration does not exceed a few nanometers, and, from the point of view of weight loss, can be considered negligible compared to the mass change due to sputtering³⁵.

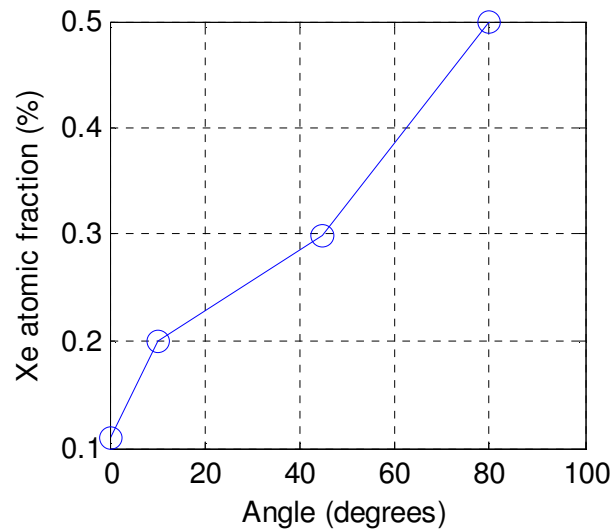


Figure 19. Angularly resolved XPS measurements of Xe in HBC-grade Boron Nitride target. The x-axis represents the emission angle of the electrons with respect to the surface normal.

2.6.3 Sputter Yield Calculation

Once a mass change has been recorded, the test parameters can be used to convert it into a sputter yield

$$Y = \frac{\Delta m}{\rho * J * t} \quad (24)$$

where Δm is the measured mass variation, ρ is the target material density, J is the beam current reaching the target, t is the time length of the test in seconds, and Y is

the resulting sputter yield, in volumetric units. In practice, the target density is not always well known, and as such equation 24 can be converted to units of $\frac{mg}{c}$ by removing ρ . The more generic units of $\frac{atoms}{ion}$ can be obtained through

$$Y = \frac{\Delta m * q * N_A}{M * J * t} \quad (25)$$

where q is the elementary charge of an ion, N_A is Avogadro's Number, and M is the molecular weight of the target.

2.7 System Thermal Control

As mentioned in section 2.3, QCM measurements are vulnerable to thermal fluctuations in the system. Filaments in the system produce heat radiation, warming the walls, the sample, and the QCM itself. The fringes of the ion beam itself strike the QCM, depositing energy in the form of heat. All of these actions serve to create a large amount of thermal noise in the QCM signal, dramatically reducing the sensitivity of the measurements. To this end, several adjustments have been made to the system.

First, the QCM is water cooled, with the water temperature controlled by a Programmable temperature controller (Polyscience 9200), which is capable of maintaining the bath water temperature to within ± 0.01 K. During experimentation, the bath water has to travel 2 meters from the temperature controller to the QCM itself, and it was noted that the presence of heat sources, even a minor as a person

entering the room, caused notable changes in the QCM signal due to warming or cooling of the water on the way to the vacuum chamber. Because of this, the lines were insulated against ambient external temperature fluctuations.

Second, the ion beam itself deposits a significant amount of energy into the QCM, particularly when measuring polar angles near the ion beam itself. In addition, the filaments radiate heat energy which dramatically warms the entire system. The cooling water helps to control this issue, but cannot completely compensate for it. However, if the QCM is allowed to reach thermal equilibrium at the position being tested, stable measurements can be taken. For this reason, at each polar angle α , the QCM is left unmoving for several minutes before measurements are taken. The length of time required to reach thermal equilibrium varies both with the angle α of the QCM and the other test conditions such as neutralizer emission and beam energy. Additionally, the point at which “thermal equilibrium” is reached is dependent on the sputtered particle signal strength. If the sample has a high yield, it generates a much stronger signal on the QCM and the thermally induced noise is negligible. However, in the case of Boron Nitride the sputter yield is low. At average beam energies (80 – 250 eV) the QCM is usually allowed to equilibrate for 5-10 minutes. At very low energies (<80 eV), the QCM is left to equilibrate for as long as 20 minutes.

Finally, the filaments to which the QCM is exposed carry poorly conditioned AC current. This leads to variations in the amount of heat being emitted from the

filaments. Little can be done to the QCM regarding this, but DC power supplies have been ordered which will at least mitigate this issue.

2.8 Sample Thermal Control

Sputtering of Boron Nitride inside a firing thruster occurs at elevated temperature. Many measurements and simulations³⁶⁻³⁹ place the wall temperature of the thruster during firing at ~ 700 °C. It is therefore of interest to both monitor and control the sample temperature. To this end, three separate sample holders have been designed. The first consists of a 15cm x 15cm x 2.5cm stainless steel block with four 1.25cm holes drilled into the sides, shown below in figure 20. These holes are carefully fitted to Omega heater cartridges so as to provide the maximum amount of contact in the vacuum. This holder has proven able to reach 550 °C, but has thus far been unable to exceed that value.



Figure 20. Sample holder designed for cartridge heaters. Pen is provided for size reference.

In order to reach higher temperatures, a new ceramic heater plate has been purchased. This plate has the same surface dimensions, but is thicker. When this plate is installed in the system, temperatures of up to 900 °C should be reachable. Measurement of temperature dependent sputter yields will be conducted in the future.

So as not to limit the facility to elevated temperature sputtering, a cooled sample holder has also been constructed. Employing high-volume flows of facility water (~10° C), the cooled holder enables research to be performed at near room temperature, even under ion beam bombardment. The cooled sample holder is shown in figure 21.



Figure 21. Cooled sample holder.

Given the target thickness, it was important to investigate the surface temperature of the sample, and not just the sample holder. Thermocouples placed at several locations on the sample holder as well as the surface of the sample itself demonstrated consistency between values, with variations of no more than 15 °C.

3.QCM Signal Analysis & Yield Determination

QCM data are recorded by the computer as a mass accumulation rate $R(\alpha, \varphi)$ in units of $\frac{g}{s}$. A program written in-house takes this data and the associated beam currents and converts each measurement into a differential sputter yield in terms of yield per steradian,

$$y(\alpha, \varphi) = \frac{R(\alpha, \varphi)r_{QCM}^2}{\rho A_s J_{B,Avg}} \quad (26)$$

where r_{QCM} is the radial distance from the target surface to the QCM, ρ is the density of the target material, A_s is the exposed surface area of the QCM (0.535 cm²), and $J_{B,Avg}$ is the average beam current reaching the target surface. The quantity $\frac{A_s}{r_{QCM}^2}$ corresponds to the solid angle the QCM subtends, while $\frac{R(\alpha, \varphi)}{\rho J_{B,Avg}}$ represents the volume of material sputtered per bombarding ion. The resulting differential sputter yield $y(\alpha, \varphi)$ has (volumetric) units $\frac{mm^3}{C*sr}$.

The differential sputter yield profile $y(\alpha, \varphi)$ can be integrated to find the total sputter yield. As will be discussed below, each yield profile is based on a fitting function termed the “Modified Zhang Equation”, and contains two fitting parameters; the total yield Y , which describes the amplitude of the yield profile, and the characteristic energy E^* , a value that describes the shape of the profile.

3.1 The Modified Zhang Equation

Since the data acquired is not continuous, it must be fitted to give an overall shape. Starting from Matsunami (equation 4), Zhang⁴⁰ developed an equation to fit sputtering data at non-normal incidence. This equation, given below, provides a very good description of angularly dependent sputtering.

$$S(E, \beta, \alpha) = 0.042 \frac{\alpha \left(\frac{M_2}{M_1}, \theta \right) S_n(E)}{\pi U_s} \cos(\alpha) \cdot \left[1 - \frac{1}{4} \sqrt{\frac{E_{th}}{E}} \left\{ \cos(\beta) \gamma(\alpha) + \frac{3}{2} \pi \sin(\beta) \sin(\alpha) \cos(\varphi) \right\} \right] \quad (27)$$

However, in the form given above, it can only be used for *a priori* calculation, not fitting. Therefore, this equation has been modified to create what is termed the “Modified Zhang Equation” (MZ)

$$y = \frac{Y}{1 - \sqrt{\frac{E^*}{E}} \cos(\beta)} \frac{\cos(\alpha)}{\pi} \cdot \left[1 - \frac{1}{4} \sqrt{\frac{E^*}{E}} \left\{ \cos(\beta) \gamma(\alpha) + \frac{3}{2} \pi \sin(\beta) \sin(\alpha) \cos(\varphi) \right\} \right] \quad (28)$$

where y is the “differential” sputter yield (discussed in section 5.1), E is the beam ion energy, β is the ion incidence angle, α and φ are the polar and azimuthal ejection angles of the sputtered particle, $\gamma(\alpha)$ is a function given below, and Y and E^* are the fitting parameters.

$$\gamma(\alpha) = \frac{3 \sin^2(\alpha) - 1}{\sin^2(\alpha)} + \frac{\cos^2(\alpha) [3 \sin^2(\alpha) + 1]}{2 \sin^3(\alpha)} \ln \left[\frac{1 + \sin(\alpha)}{1 - \sin(\alpha)} \right] \quad (29)$$

From equation 28 it can be seen that Y is an amplitude parameter, and that increasing Y increases the overall magnitude of the profile. Similarly, E^* is part of the energy ratio $\frac{E^*}{E}$, which controls the shape of the profile. An E^* of zero results in

a completely diffuse profile, while increasing E^* increases the under-cosine nature of the profile (within the limit $E^* < E$). As will be shown in Chapter 5, the Modified Zhang equation provides accurate fits to the sputter yield profiles, both for Boron Nitride and for other materials tested including Molybdenum²⁰.

3.2 Analysis Considerations

3.2.1 Assumptions

Analysis of test results requires that the following assumptions be made. The solid angle cone observed from the QCM to the target must contain the entire target surface, since this equation normalizes the mass accumulation by the total beam current reaching the target. In fact, the QCM viewing angle is approximately 5.4 steradians, corresponding to an area larger than the target surface. Also, the viewing angle of the QCM actually corresponds to a range of polar and azimuthal angles, that is, a sputtered particle from one area of the target may reach the QCM with a value (α, φ) , while another particle from a different area may also reach the QCM with a slightly different (α, φ) . However, a simulation has been performed⁴¹ which shows a worst-case 5% error if the QCM and target are treated as points (not areas) connected by a single vector.

In addition to the requirements imposed by the preceding concerns, the assumption must be made that the beam current leaving the ion source is equal (after subtracting scattering and charge exchange losses) to that reaching the target

surface. To validate this assumption, conductive targets of the same size and shape as non-conductive targets are placed under the ion beam at the same conditions, and the current reaching their surface is measured. The current measured on the conductive target matches (within $\pm 5\%$) the current leaving the grid voltage power supplies after subtracting the calculated 10% loss to charge exchange and scattering (see Figure 11 with a target 23 cm downstream from the ion source).

3.2.2 Condensables

Not all particles which arrive at the QCM adhere to the surface. Assumptions of sticking coefficients can be validated through testing with single-element targets²¹, however multi-component targets such as Boron Nitride add a dramatic complexity to the situation. Sputtered particles can take the form of Boron atoms, Nitrogen atoms, and dozens of polyatomic compounds including B_2 , BN , B_xN_y , and N_2 . Since each of these compounds has a distinct atomic mass, fully interpreting the QCM signal requires knowledge of the fraction of each which is present in the experiment. To this end, X-Ray Photon Spectroscopy (XPS) has been performed on the QCM crystal surface to better understand which compounds are present. Figure 22 illustrates these results, with the Boron Nitride surface on the left and the crystal surface on the right, both taken after a sputtering experiment.

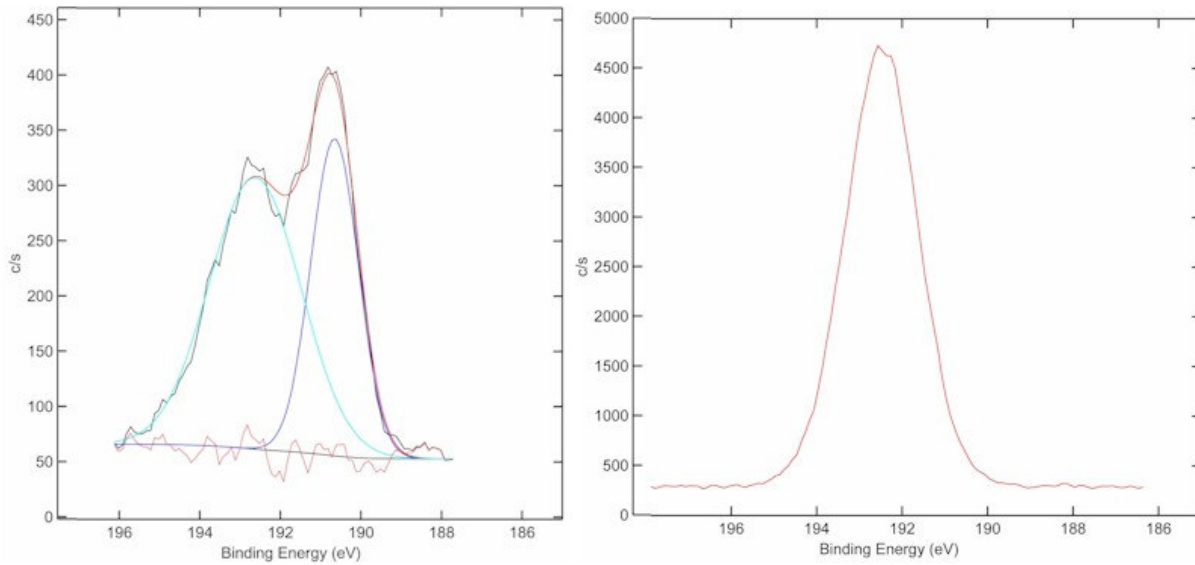


Figure 22. Left: XPS scan of HBC Boron Nitride surface. Right: QCM crystal surface.

From the left graph, peaks for Boron Nitride, Boron, Nitrogen, water vapor, and other atmospheric constituents can be seen. However, on the crystal surface only one single peak is present, representing B_2O_3 (from the NIST database⁴²). The Boron on the crystal is not atomic because the crystal is exposed to atmospheric oxygen during transit from the vacuum chamber to the XPS test facility. However, the lack of Nitrogen on the crystal indicates that, of the constituent particles on the Boron Nitride surface, the majority of the sputtering occurs as Boron atoms or B_x , and not as B_xN_y . XPS analysis of a Boron Nitride surface performed before and after sputtering by Garnier³¹ showed little variation between the Boron and Nitrogen fractions, suggesting that Boron and Nitrogen are sputtered at approximately the rates (1:1) expected by the bulk composition (one Boron atom for every Nitrogen atom).

3.3 MATLAB Analysis

All collected data is processed through a MATLAB program written at CSU. The program accepts the raw recorded data from the QCM controller, and takes several user inputs including average beam current, beam voltage, chamber operating pressure, feed gas, and several target material parameters, and uses these to convert the data into units of $\frac{mm^3}{C}$. Once the conversion has been made, the program applies the Modified Zhang equation to fit the data using the two free parameters Y and E^* . The output from the program is a file containing all the converted data points and the best-fit values of Y and E^* for the data, and plots of the individual data series with their best-fit Modified Zhang lines and the interpolated (fitted) hemisphere above the target. Appendix A is the code for this program.

4. Total Sputter Yields

4.1 Molybdenum Validation Experiments

Periodically during testing, a Molybdenum target was used in place of the Boron Nitride target. The Molybdenum target is 15 cm x 15 cm, and is 99.5% pure. This target is used to verify test parameters such as beam current, as well as validating system operation and data integrity. The Molybdenum target is bombarded under identical conditions to the Boron Nitride target. Figure 23 demonstrates the results for Molybdenum bombardment at normal incidence for 150, 250, and 350 eV. The Yamamura and Tawara prediction curve as well as data from Kolasinski⁴³, Doerner⁴⁴, and previous CSU testing²⁰ are included for comparison. Each data point in figure 23 represents the average value of many tests, while the error bars represent the spread in the total yields from those tests. Some variation in the data is expected, as shown by the somewhat lower yields obtained during this testing period. However, the data is strongly self-consistent, and indeed matches both the older CSU data and that from Doerner within error bars. Agreement with the Yamamura and Tawara curve also further validates the assumption of unity for the sticking coefficient.

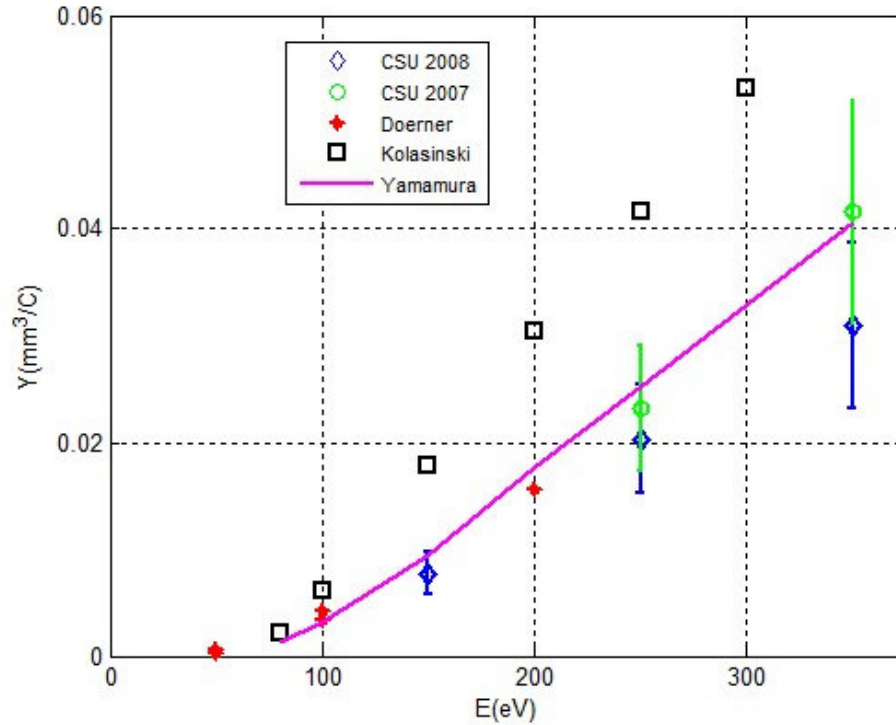


Figure 23. Molybdenum bombardment at normal incidence (CSU 2008). Yamamura & Tawara prediction, Kolasinski data⁴³, Doerner data⁴⁴, and former CSU (CSU 2007) data are provided for comparison.

4.2 Total Sputter Yields of Boron Nitride

The total sputter yield, when given in atomic units, is defined as the total number of particles that are ejected per incident ion. This value can have many different units, the most common of which are $\frac{atoms}{ion}$ and $\frac{mg}{C}$. For the purposes of this study, however, units are usually given as $\frac{mm^3}{C}$ corresponding to the volume of sputtered material per unit charge of ions, which prevents any confusion due to the multi-component nature of the material. For Boron Nitride, this represents the

difference between the sputter yield of atomic Boron and that of Boron Nitride or atomic Nitrogen.

Appendix A contains a full table of data taken during testing. These data are summarized here. Experimental points were taken at Xenon ion energies between 60 eV and 350 eV, and at ion incidence angles (β) between 0° (normal) and 75° . During testing, the sample was not cooled, and reached a steady-state temperature of approximately 80° C.

Figure 24 shows the total sputter yields of HBC-grade Boron Nitride, as determined from the Y -parameter of the best-fit MZ profile as a function of beam ion energy for normal incidence. Recall that the total yields measured by QCM represent only the deposition of condensable components, and require equation 22 to find the corresponding full Boron Nitride yield. Measurements of total sputter yield are performed multiple times for nearly all data points, and are then averaged for display in Figure 24.

Error bars in figures 24-26 are calculated as the greater of the experimental uncertainty and the spread in the data taken at the same conditions. The uncertainty stems predominantly from fluctuations in the ion source itself, both in the shape and quality of the ion beam and its position on the target, and in the power output from the filaments in the ion source. Methods for determining the variation in beam current are described in section 2.4.4. Figures 25 and 26 show the total sputter yields of HBR-grade and HP-grade Boron Nitride respectively, using the same method as with HBC-grade above.

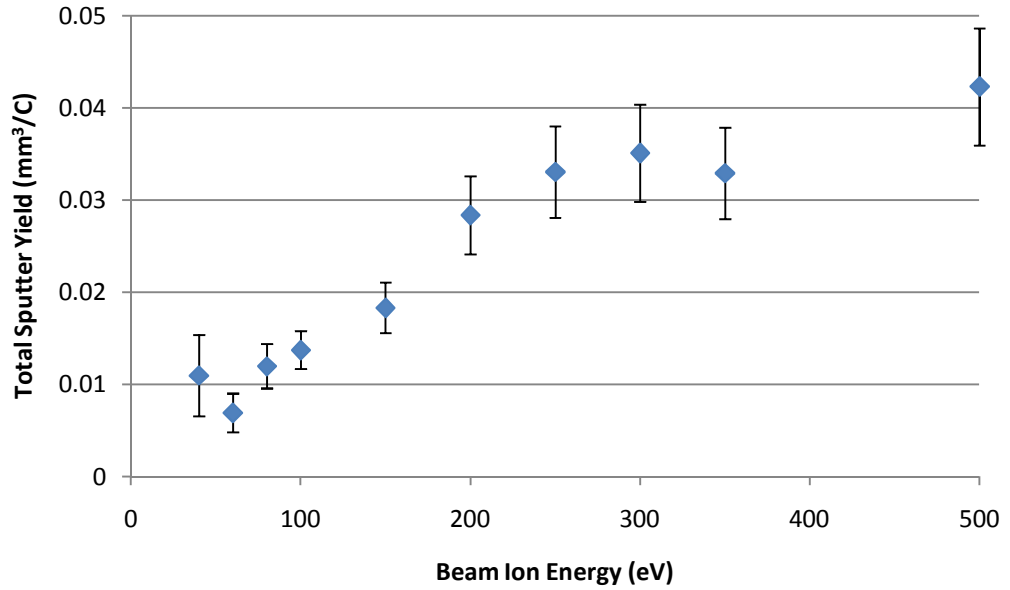


Figure 24. Total sputter yields of HBC-grade Boron Nitride at normal incidence.

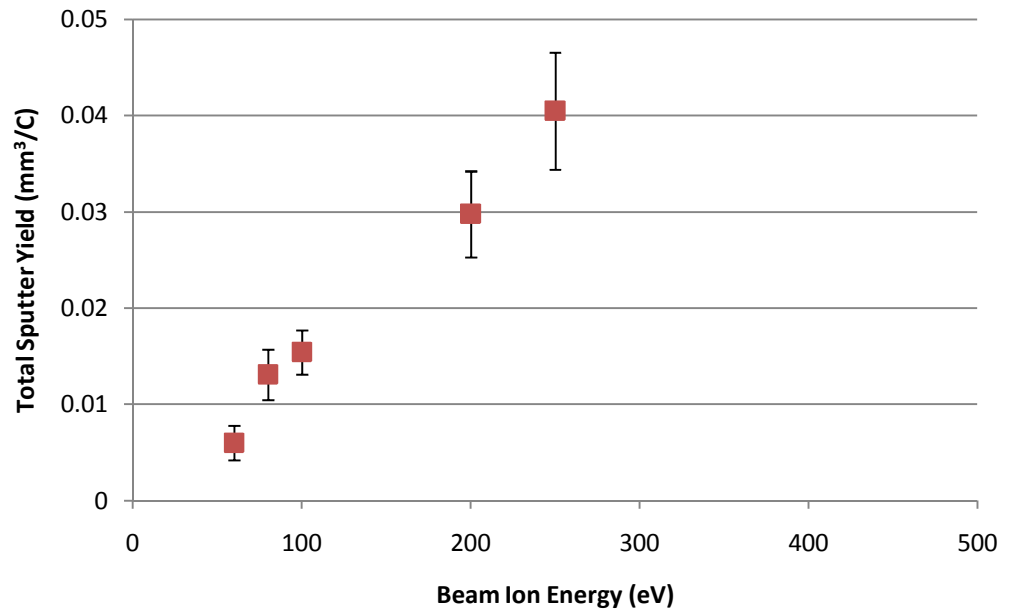


Figure 25. Total sputter yields of HBR-grade Boron Nitride at normal incidence.

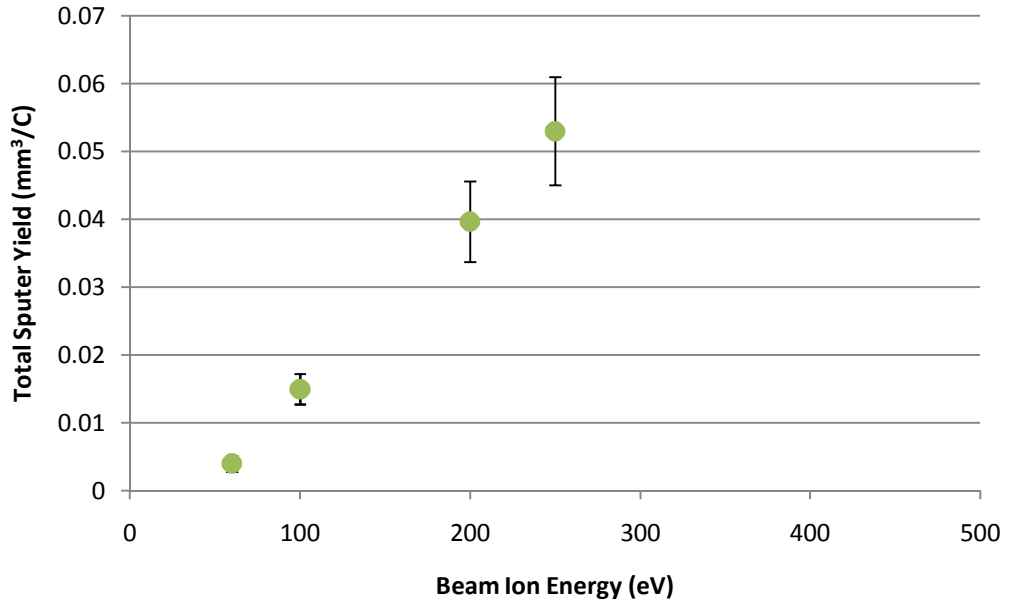


Figure 26. Total sputter yields of HP-grade Boron Nitride at normal incidence.

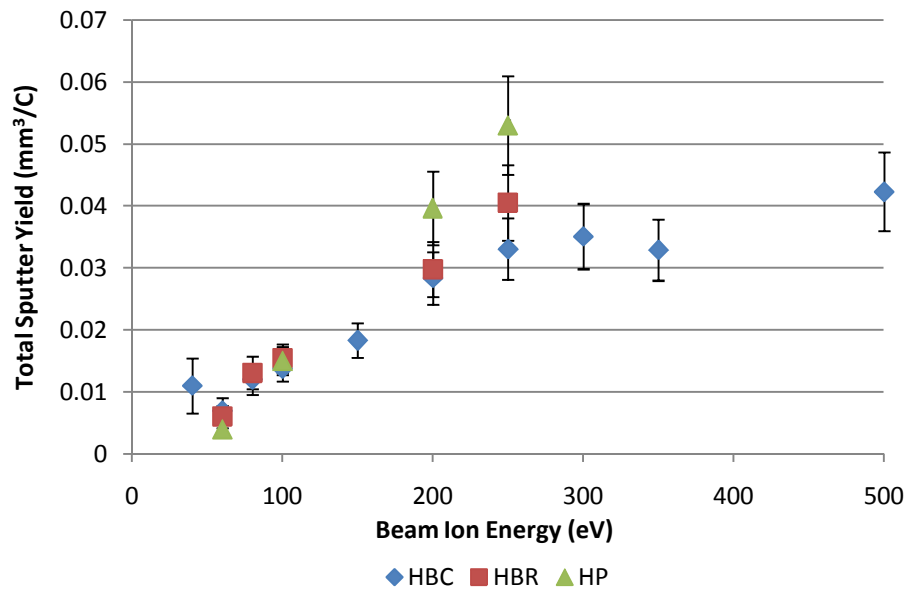


Figure 27. Total sputter yields of all three grades of Boron Nitride at normal ion incidence.

From the above figures, the sputter yield of HBC- and HBR-grades of Boron Nitride are nearly identical, while the yield of HP-grade is somewhat higher, though

still within statistical uncertainty of the HBC and HBR samples. Note that all yields presented in Figures 24-27 are condensable components only. To calculate the total sputter yield, one must use equation 22 along with the results shown on the above figures. Figure 28 compares these yield measurements with those from Garnier³¹, Abashkin⁷, Semenov⁴⁵, Kim⁴⁶, and computer modeled values from Yim⁴⁷.

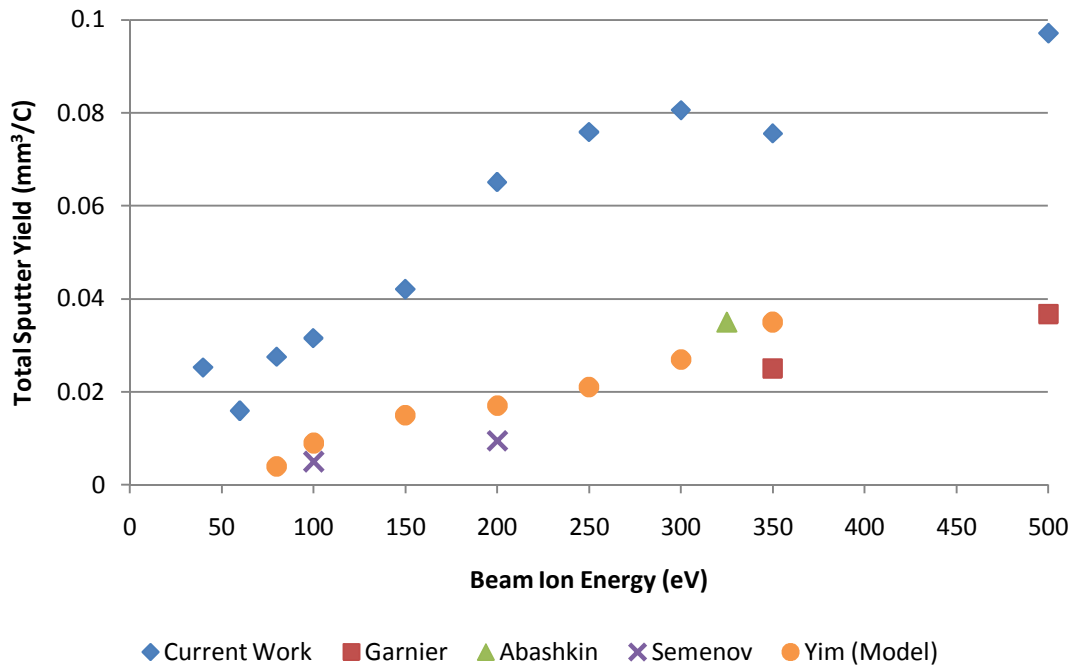


Figure 28. Comparison of total sputter yields to other published values. See text.

The sputter yields plotted in figure 28 are total (maximum) yields as opposed to condensable (QCM) yields, converted using equation 22 to make comparison with data from the literature possible. Note that many published yields do not specify the grade of Boron Nitride used, and that the data points from Yim were calculated using the available results at the time. Still, the results presented herein are at least a factor of two higher than most others published in this energy range. Reasons for

this are uncertain but are believed to include variations in the target material as well as a strong yield dependence on neutralization conditions. As discussed in section 4.3 and shown in figure 32, the addition of a PBN to the system increased the sputter yields by a factor of roughly 2 as well. Given that this is the principle difference between the system used in this experiment and that used in many others, there were concerns about induced effects from the PBN. However, there is no reason to believe the PBN is artificially raising the sputter yield. The particles emitted from the PBN have a -17 V bias, well below the sputter threshold, and are emitted approximately tangential to the target surface. Additionally, any target surface bias introduced by the PBN should be quickly neutralized by the ion beam itself.

Testing was also performed at varying angles of incidence. Figure 29 demonstrates the total condensable sputter yield measured as a function of β . In general, the peak sputter yield occurs near a value for β of 55° , as predicted by the Yamamura Equation⁴⁸ using the appropriate values for Boron. Similar tests were performed at 250 eV and 350 eV, and are presented in Figures 30 and 31. All three show similar trends, with peaks near 55° incidence.

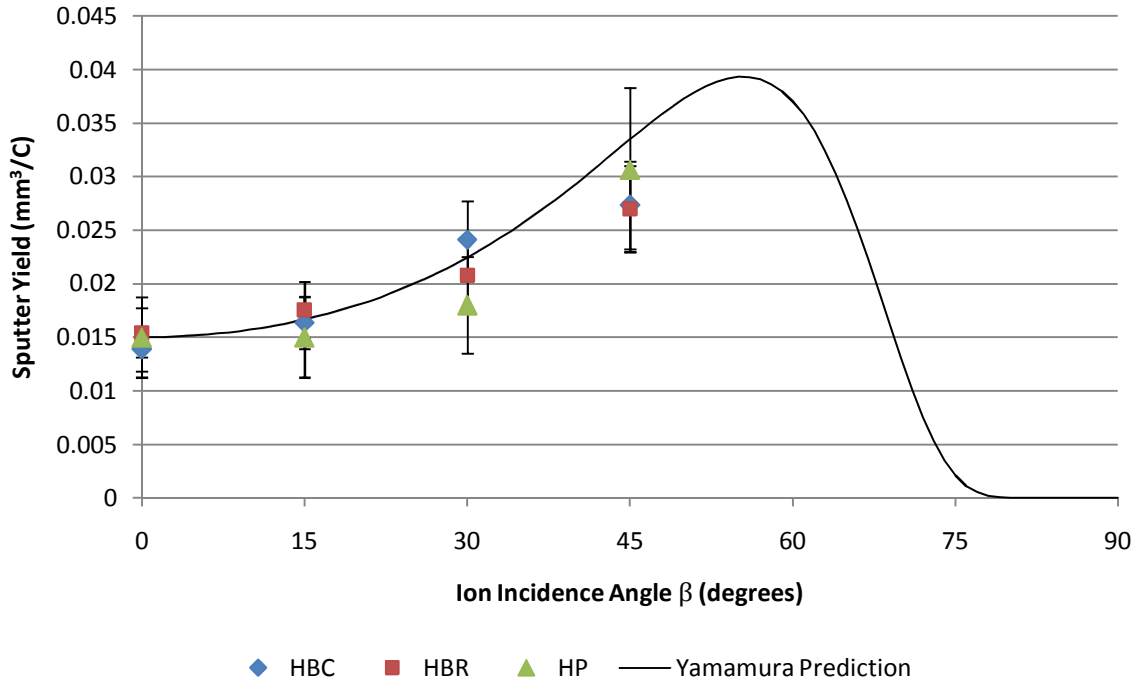


Figure 29. Sputter yields of all three grades of Boron Nitride at 100 eV. A Yamamura prediction is provided for reference, and calculated using the average values for Boron and Nitrogen and their total atomic weight. Since the Yamamura prediction is intended for monatomic species, it should be viewed as a guide, not an expectation.

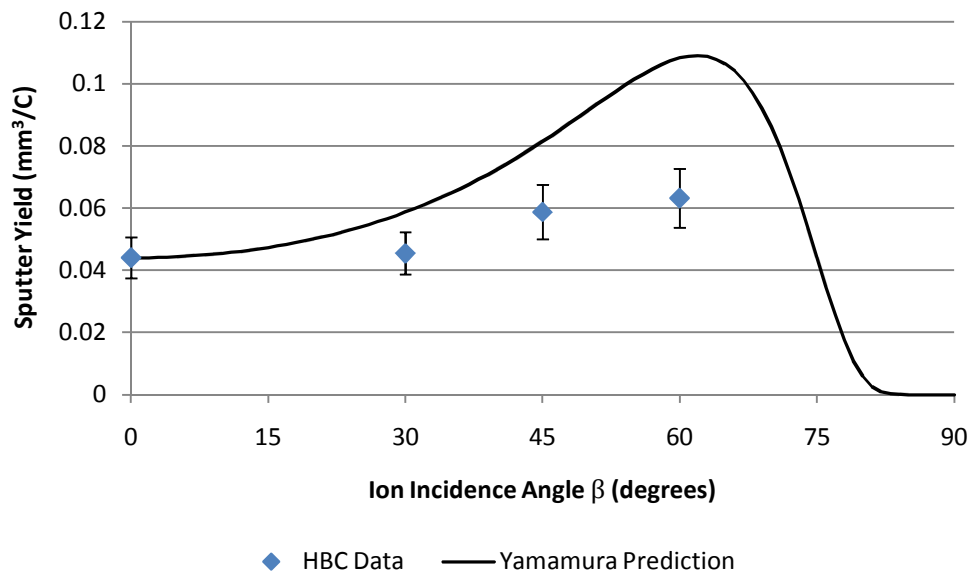


Figure 30. Sputter yield of HBC-grade Boron Nitride at 250 eV. The Yamamura prediction is provided for reference, calculated using the average values for Boron and Nitrogen and their total atomic weight.

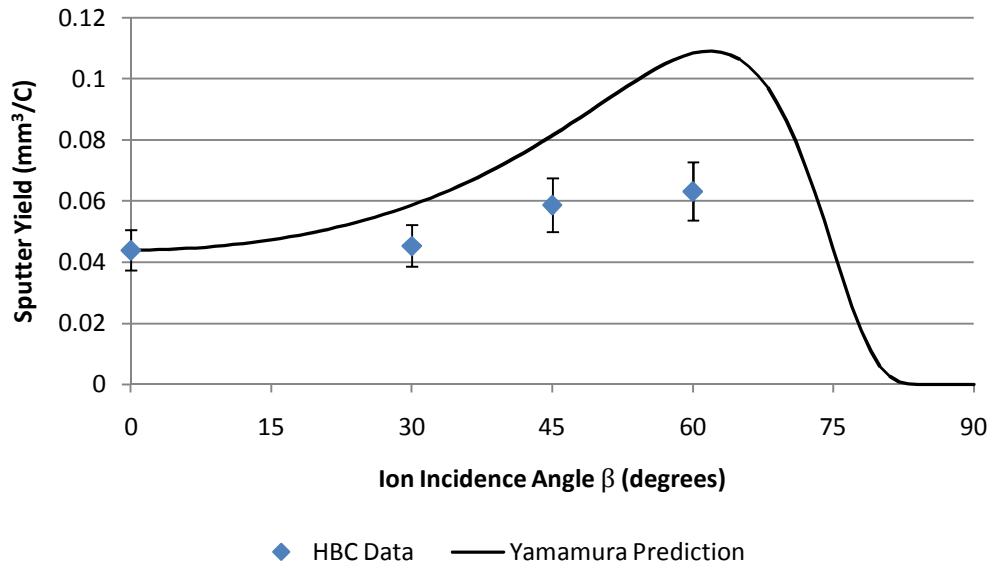


Figure 31. Sputter yield of HBC-grade Boron Nitride at 350 eV. The Yamamura prediction is provided for reference, and calculated using the average values for Boron and Nitrogen and their total atomic weight.

4.3 Dependence of Sputter Yields on Neutralization

In space, the thruster plasma is neutralized by a cathode neutralizer, while the material of interest (the channel wall) is neutralized by ambient electrons inside the thruster. In a laboratory, the ion source is usually neutralized by a filament, as in this experimental setup. However, it has been shown^{30,35,49-51} that surface charge build-up plays an important role in sputter measurement. To ensure accurate sputter yield measurements, a neutralization study has been performed to quantify the effect of filament neutralization and investigate the addition of a plasma bridge neutralizer (PBN) for the target surface.

By placing the QCM in a single polar location, a mass deposition signal (i.e. sputter rate) is recorded. As the neutralizer emissions are varied (through changes in the applied voltages and currents), the signal changes in response to the conditions on the target surface. It is important to ensure that no other elements of the beam conditions change, and to this end, beam and discharge currents, grid and anode voltages, and fuel gas flow rates are carefully monitored, and QCM signals are recorded for lengthy periods of time to eliminate any fluctuations or drift caused by transient thermal noise. Once stability has been acquired, the QCM signal is interpreted as a sputter rate, and compared to other rates taken under different neutralizer conditions. Figure 32 demonstrates the effect of installing a plasma bridge neutralizer to assist with target surface neutralization.

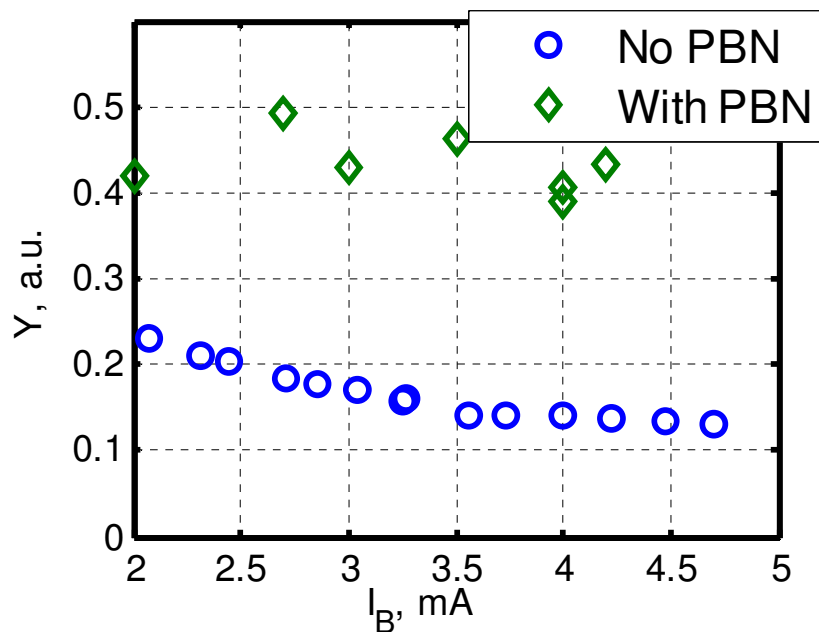


Figure 32. Comparison of sputter yield of Boron Nitride against filament-neutralized beam current ($I_{filament} \sim 6 I_{beam}$) with and without the Plasma Bridge Neutralizer (PBN) installed in the system.

The PBN consists of a hollow stainless steel housing (keeper) around a tungsten filament cathode, both of which are biased relative to each other and to ground to promote the emission of electrons. The PBN is positioned such that the ejection path of the electrons is tangential to and 2-3 cm above the surface of the target. Once the importance of the PBN had been shown, the emission currents of the PBN and of the source neutralizer were varied, producing Figures 33 and 34.

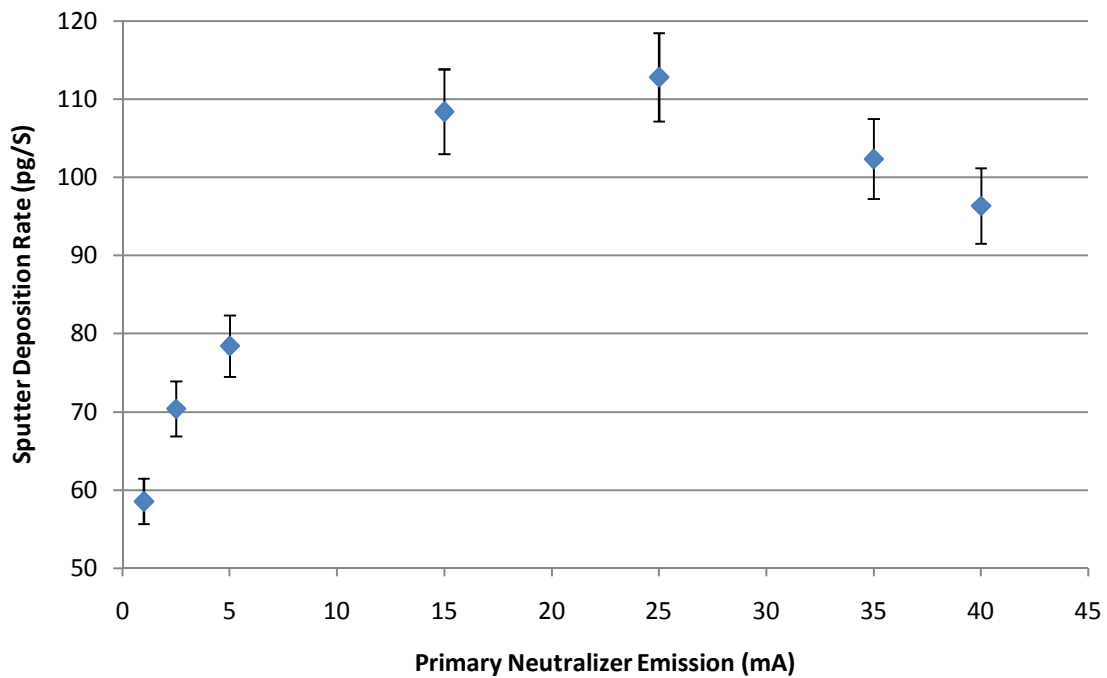


Figure 33. Sputter yield rate with variation of the primary (source) neutralizer emission.

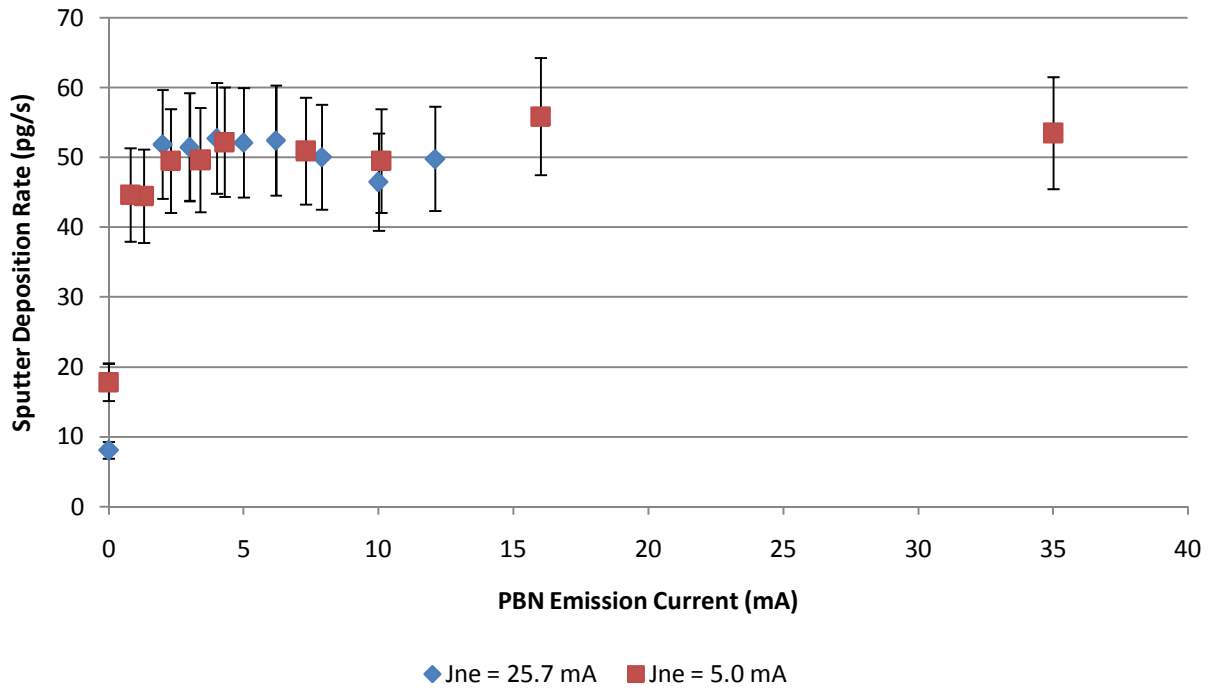


Figure 34. Sputter yield rate with variation of the PBN emission.

The objective of both tests is to locate a saturation point, at which the sputter yield is roughly at its maximum (no surface charging effects), without the neutralizer emissions being excessively high, which would limit the lifetime of the filament. From the data presented here, it is determined that an optimal operating condition occurs with primary emission near 25 mA and PBN emission at roughly 6 mA.

5. Differential Sputter Yield Profiles

Differential sputter yields are fitted using the two shape parameters discussed in section 3.1 within the Modified Zhang equation (28). A comparison between values of $\frac{E^*}{E}$ allows investigation into the evolution of the overall shape of the profile, while Y allows direct comparison of the associated total sputter yields for each data set.

5.1 Fitted Profiles

When a differential test has been completed, the data are processed through the program presented in section 8.2. The outputs of this program include the (integrated) total sputter yield, and plots of both raw and fitted data against QCM position. Also on these plots is a diffuse profile with the same (integrated) total sputter yield for comparison.

Figure 35 demonstrates a Modified Zhang fit to a QCM test of Molybdenum at 350 eV. Given a clean data set, the fit is highly representative of the measurements. The strongly under-cosine shape denotes a high value of E^* , in this case 72 eV. For Boron Nitride, these profiles are typically less under-cosine. Figure 36 is the fitted profile for HBC-grade Boron Nitride at 350 eV and normal incidence.

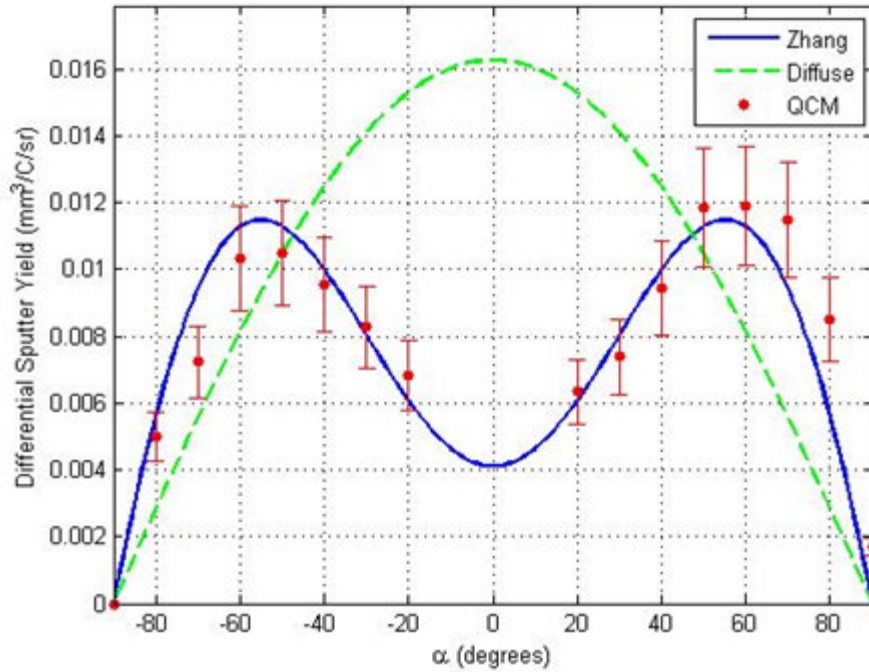


Figure 35. Fitted profile of a QCM sweep over Molybdenum at 150 eV, normal incidence. Red dots are actual data points, the blue line is the Modified Zhang fit, and the green dashed line is a diffuse profile with the same total yield.

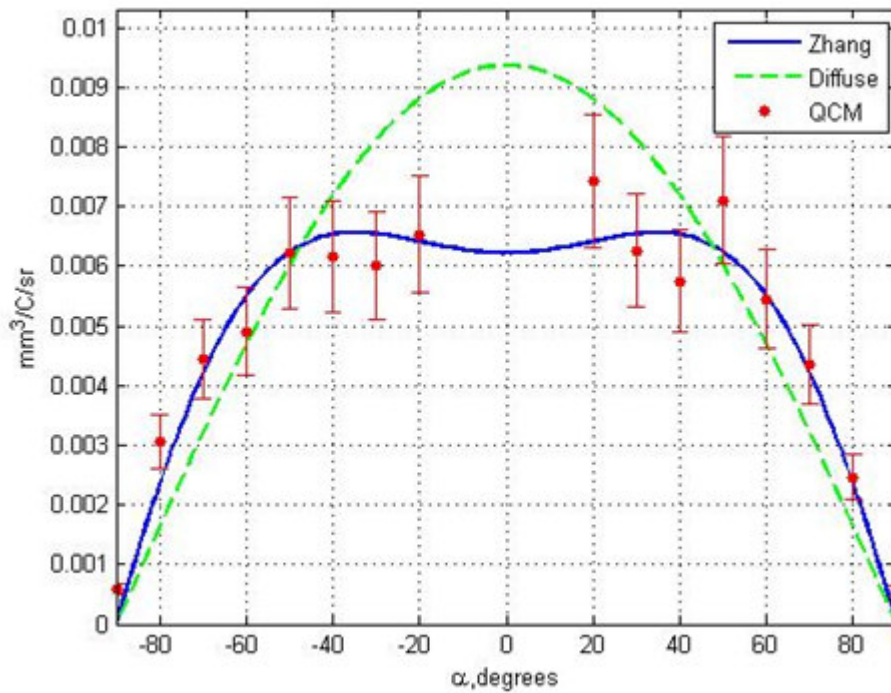


Figure 36. HBC-grade Boron Nitride at 350 eV, normal incidence.

These fits are applied to non-normal incidence data as well. Figure 37 presents the fit to HBC-grade Boron Nitride at several higher angles of incidence.

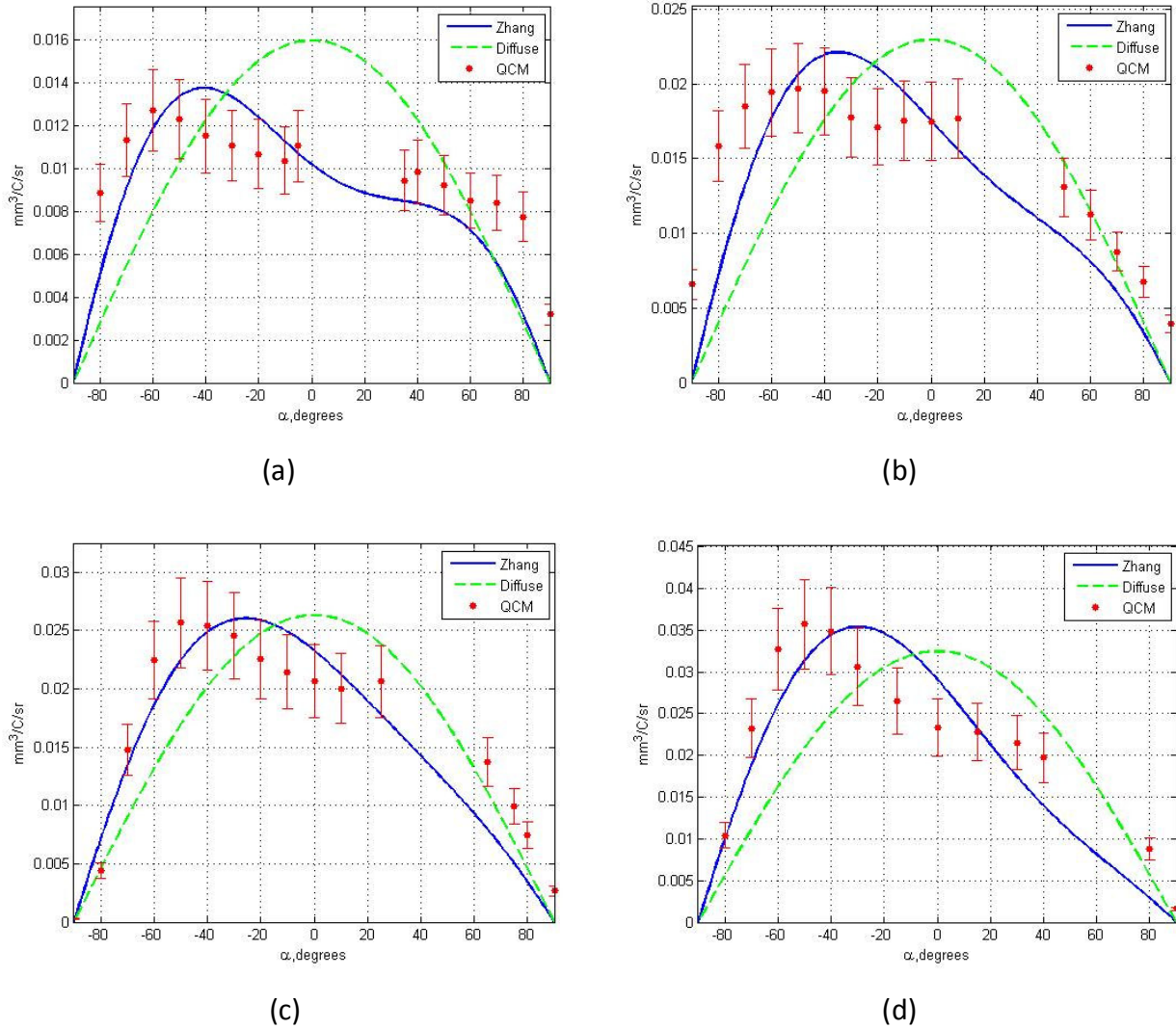


Figure 37. Fitted profiles of HBC-grade Boron Nitride at 350 eV and various angles of ion incidence. (a) $\beta = 15^\circ$, (b) $\beta = 30^\circ$, (c) $\beta = 45^\circ$, (d) $\beta = 60^\circ$. For clarity, the y-axis in these graphs is the differential sputter yield.

It is apparent that the fits do not capture the shape of the profile quite as accurately as at normal incidence, however the shape remains reasonably representative of the data. Integrated total yields also agree well with total yields

from mass loss measurements (given the known variation due to condensable fraction), as well as the trends from the Yamamura prediction mentioned above.

5.2 Zhang-Fit Hemispheres

When data are taken at multiple angles of φ for a given test condition, the various azimuthal “slices” of data can be individually analyzed to observe trends or can be combined and extrapolated to form contour plots on hemispheres representing the overall differential sputter yields above the target. At normal incidence, these azimuthal data sets are (within experimental uncertainty) symmetric for each of the tested grades of Boron Nitride. However, at non-normal incidence, these hemispheres are asymmetric (with φ) and allow a more visual illustration of the three dimensional profile of the target sputter behavior. Figures 38 and 39 present examples of Zhang-fit hemispheres for normal and non-normal incidence, respectively.

From these figures, it is clear that the assumption of a cosine distribution of the sputter yield is a poor choice. Referring to Figures 37a and 37d, for example, the dashed line representing the cosine diffuse assumption is clearly well off the experimental data set. This is true for Molybdenum as well, as shown in figure 35. Indeed, testing has shown that even a nominal 5° inclination from normal incidence results in an asymmetric data set, as shown in Figures 40 and 41.

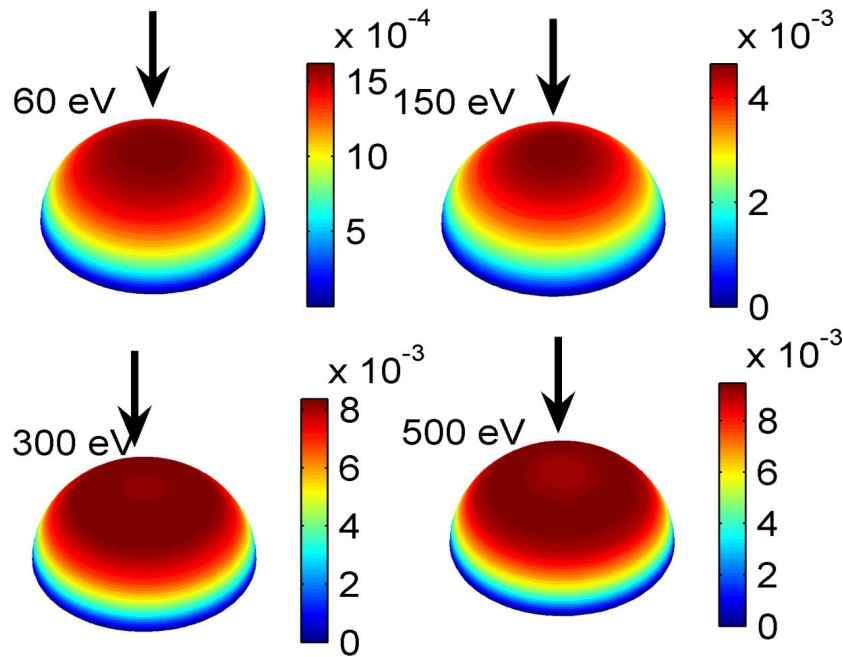


Figure 38. Zhang-fit hemispheres for various beam ion energies at normal incidence.

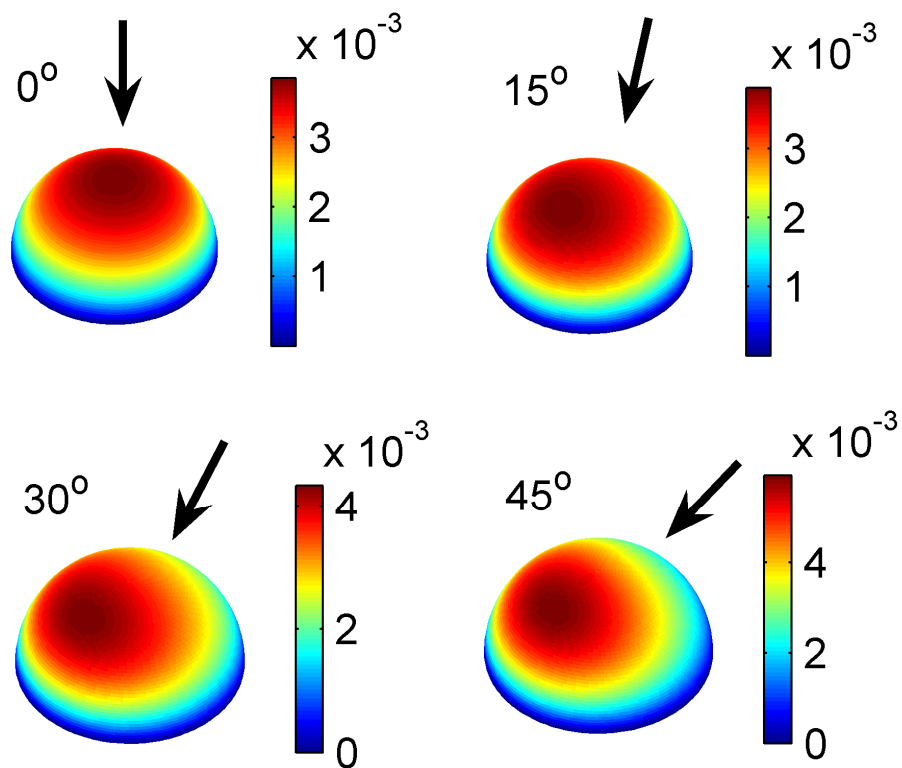


Figure 39. Zhang-fit hemispheres for various incidence angles at 100 eV. The arrows demonstrate the angle of ion incidence.

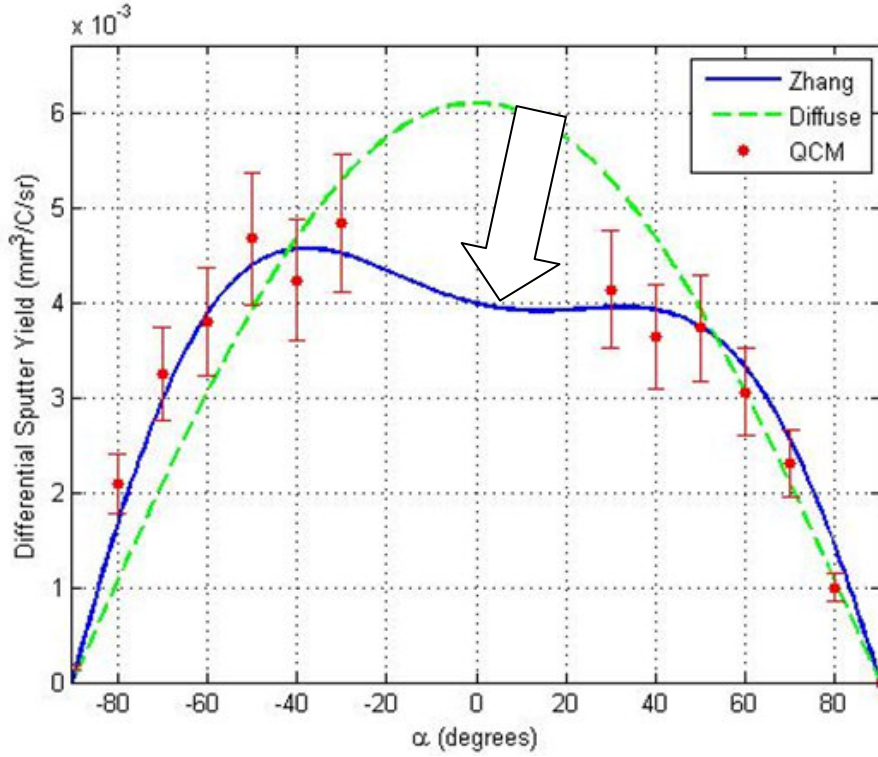


Figure 40. HBC-grade Boron Nitride at 5° incidence at 150 eV. Note the asymmetry between the left and right halves (left and right of $\alpha = 0$), as compared to the diffuse profile.

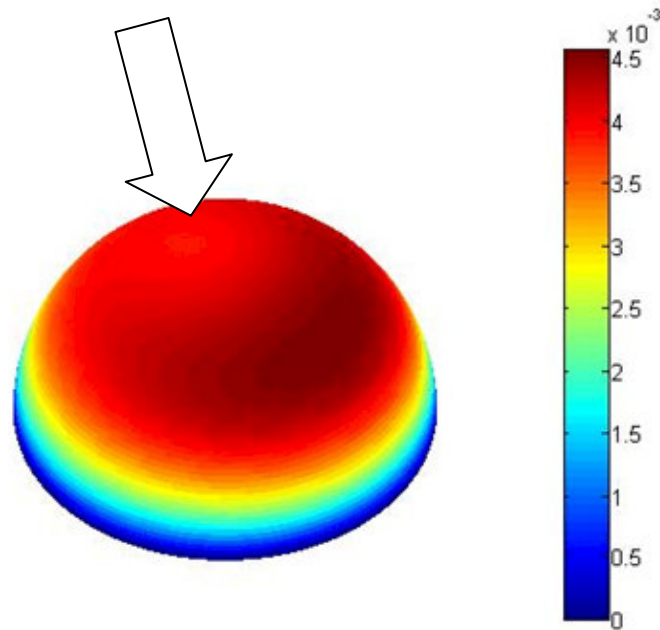


Figure 41. Zhang-fit hemisphere of HBC-grade Boron Nitride at 5° incidence. Note that the forward sputter lobe is more than 10% higher than the backscatter lobe, indicating a strong asymmetry even at near-normal angles of incidence.

5.3 E^* Shape Factors

For differential sputter yields, valuable information can be taken from the shape of the distribution as well as the overall yield. The shape describes where deposits of sputtered particle densities are highest, and can be used during the design phase of a spacecraft to ensure re-deposition of sputtered material onto sensitive surfaces such as solar panels is minimized. The ratio $\frac{E^*}{E}$ provides this description, in that larger values of $\frac{E^*}{E}$ correspond to more under-cosine distributions (for the energy range of interest to this study), while an $\frac{E^*}{E}$ value of zero corresponds to the diffuse assumption of the profile shape (cosine).

However, since it is the ratio between the beam energy E and the shape parameter E^* which describes the overall shape, figure 42 provides a more complete picture of the evolution of the profile shape with respect to beam energy. The $\frac{E^*}{E}$ ratio is relatively constant independent of energy which suggests that the overall profile shape changes little through the studied energy range. All three grades show similar trends.

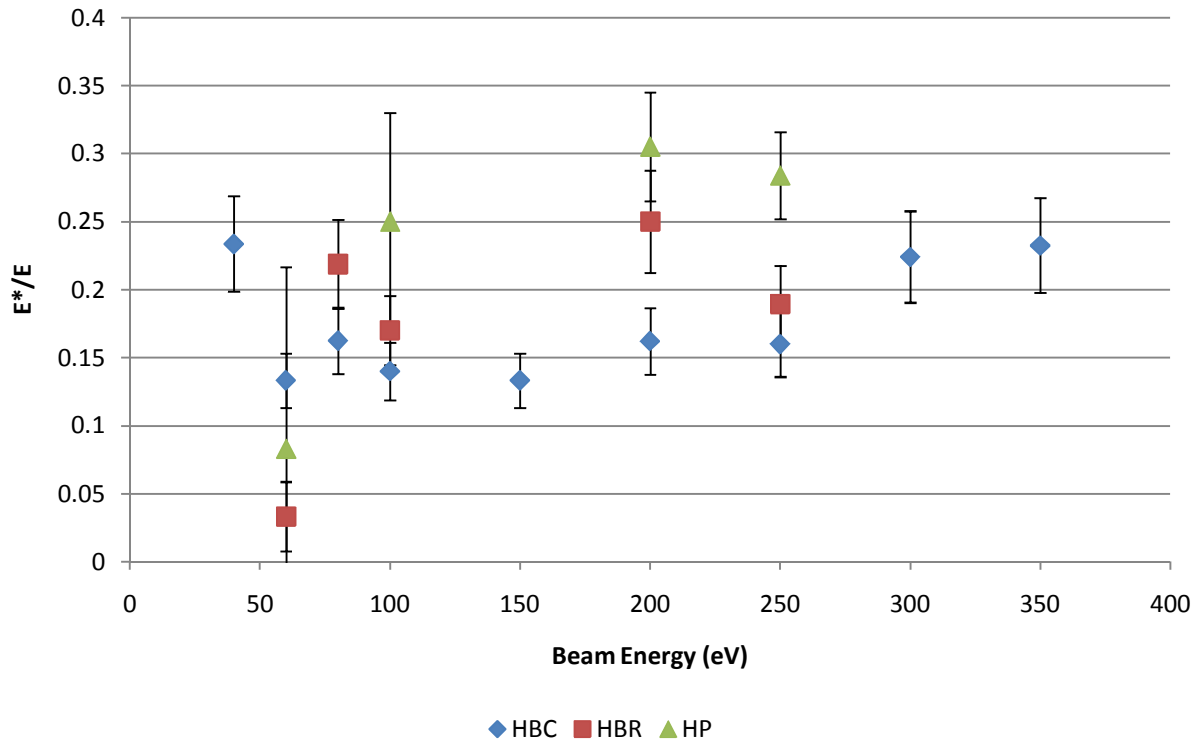


Figure 42. Evolution of the ratio $\frac{E^*}{E}$ with respect to beam ion energy E for all studied grades of Boron Nitride at normal incidence.

6. Conclusions

6.1 Conclusions

Ion sputtering has been shown to be an important concern in space propulsion. Erosion of grids and channel walls is a life-limiting factor in ion engines and Hall thrusters. Total and differential sputter yield measurements of Boron Nitride under Xenon ion bombardment have been made using a QCM. A four-grid ion source was developed to allow measurements below ~ 100 eV. Energies in this range are important due to their preeminence in Hall Thruster discharge chambers, where most sputtering of interest takes place. This ion source was profiled and found to be well-collimated with a divergence half-angle of 5° - 7° at higher energies, increasing to 10° at 30 eV, and having a singles-to-double ratio of $< 5\%$. The ion energy distribution was found to be highly monoenergetic ($\frac{\Delta E}{E} < 0.1$). The base pressure in the vacuum chamber is 5×10^{-7} Torr, with an operating pressure of roughly 8×10^{-5} Torr. A rotating arm allows the QCM to take data in a polar arc over the target, while an additional rotating motor allows the target to be turned through azimuthal angles without breaking vacuum. Polar sweeps by the QCM can be combined to create hemispheric plots of sputter yields. The QCM is thermally controlled to minimize noise with the use of a Polyscience 9200 temperature controller with an accuracy of 0.01 K. Two

sample holders have been constructed to either heat or cool samples as needed. Mass loss measurements have been made, but are somewhat suspect due to the moisture absorption of Boron Nitride, especially in the case of the HP-grade. Validation of the system is accomplished by use of Molybdenum sputtering. Test results are analyzed using the Modified Zhang equation, and processed through an application written in-home in MATLAB. Best-fit parameters are extracted from the Modified Zhang fit, and used to describe the magnitude and shape of the data. Integration of the Modified Zhang fit corresponds to the total sputter yield for the test. Sputter yield data are given in units of $\frac{mm^3}{c}$ to avoid confusion due to the multicomponent nature of Boron Nitride. Total sputter yields of HBC- and HBR-grade Boron Nitride are similar, with HP-grade Boron Nitride slightly higher. All three grades show trends fit well by either Yamamura & Tawara or Bohdanský modeling equations. Atmospheric effects including moisture absorption inhibit the validity of weight loss measurements of total sputter yield, particularly with the HP-grade. QCM-based measurements do not suffer from this effect, and are treated as more accurate. Neutralization of the ion beam is shown to have a strong effect on the sputter yield. A filament is used to neutralize the ion beam, and a PBN has been installed to neutralize target surface potential. Optimization of neutralization techniques has yielded an ideal operating condition for this chamber. Differential profiles presented above indicate that the typical assumption of a diffuse yield is inaccurate, increasingly so at higher angles of ion incidence. Profiles measured at varied azimuthal angles over the target during the same test can be used to simulate

a hemispheric profile over the entire surface of the target. Sputter yields are presented for ion energies ranging from 30 – 500 eV, and at ion incidence angles from normal to 60°. Total sputter yields published herein are roughly a factor of two higher than those currently available in the literature. Reasons for this discrepancy are uncertain; however they likely include variations in both neutralization schemes and grades of Boron Nitride. Shape factors of the differential yield are compared and show near-constant values relative to their associated ion energies.

6.2 Continuing Research

Future work includes pursuit of the temperature dependence of the sputter yield of Boron Nitride. Preliminary results³⁵ have suggested that elevated temperature may yield a sharp increase in the overall yield, although the profile shapes have not appeared different. Work needs to be performed to isolate the cause of this apparent increase (facility effect or true change in yield), and to obtain additional data points at various temperatures throughout the range capability of the system herein. As discussed in section 2.8, the thruster firing temperature is in the vicinity of 700 °C. This presents several challenges. First, the sample holder must be able to heat the sample to 700 °C. Second, the chamber must be made capable of withstanding 700 °C temperatures inside. Finally, the QCM must be carefully thermally controlled in the presence of a very large heat source. Insulation appears to be the solution for the first problem, and cooling wrapped around the outside of

the chamber is the solution for the second. Maintaining the temperature of the QCM will likely be the most difficult problem, as it is much more sensitive to the temperature.

7. References

- ¹D. Goebel, I. Katz, *Fundamentals of Electric Propulsion: Ion and Hall Thrusters*, JPL Science and Technology Series, JPL/CalTech (2008)
- ²O. Duchemin, "An Investigation of Ion Engine Erosion by Low Energy Sputtering", *Ph. D. Dissertation*, California Institute of Technology, Pasadena, CA (2001)
- ³P. Sigmund, "Theory of Sputtering I: Sputtering Yield of Amorphous and Polycrystalline Targets", *Physical Review*, **184** 2 pp. 383-416 (1969)
- ⁴N. Matsunami *et Al.*, "A Semi-Empirical Formula for the Energy Dependence of the Sputtering Yield", *Rad. Eff. Let.*, **57** pp. 15-21 (1980)
- ⁵Y. Yamamura, H. Tawara, "Energy Dependence of Ion-Induced Sputtering Yields from Monatomic Solids at Normal Incidence", *At. Nucl. Data Tables*, **62**, pp. 149-253 (1996)
- ⁶J. Bohdansky, "A Universal Relation for the Sputtering Yield of Monatomic Solids at Normal Ion Incidence", *Nucl. Inst. Meth.*, **B2** pp. 587-591 (1984)
- ⁷V.V. Abashkin, O.A. Gorshkov, A.S. Lovtsov, A.A. Shagaida, "Analysis of Ceramic Erosion Characteristic in Hall-Effect Thruster with Higher Specific Impulse", *30th International Electric Propulsion Conference, IEPC-2007-133*, Florence, Italy (2007)
- ⁸E. Ahedo, A. Anton, I. Garmendia, I. Caro, J. Gonzalez del Amo, "Simulation of Wall Erosion in Hall Thrusters", *30th International Electric Propulsion Conference, IEPC-2007-067*, Florence, Italy (2007)
- ⁹S.K. Absalamov *et Al.*, "Measurement of Plasma Parameters in the Stationary Plasma Thruster (SPT-100) Plume and its Effect on Spacecraft Components", *28th AIAA Joint Propulsion Conference, AIAA-92-3156*, Nashville, TN (1992)
- ¹⁰E. Goldstein, *Verhanden Deutsche Physikalische Gesellschaft*, **4** pp. 228-237 (1902)
- ¹¹J. Stark, *Z. Elektrochem.*, **14** pp. 752 (1908)
- ¹²L. Feldman, J. Mayer, "Fundamentals of Surface and Thin Film Analysis", North Holland-Elsevier, Prentice Hall, New York (1986)
- ¹³V. Shutthanandan, P. Ray, N. Shivaparan, R. Smith, T. Thevuthasan, M. Manteniaks, "On the Measurement of Low-Energy Sputtering Yield Using Rutherford Backscattering Spectrometry", *25th International Electric Propulsion Conference, IEPC-97-069*, Cleveland, OH (1997)
- ¹⁴A. Wucher and W. Reuter, "Angular Distribution of Sputtered Particles from Metals and Alloys", *J. Vac. Sci. Technol. A*, **6** pp. 2316-2318 (1988)

- ¹⁵E. Oyarzabal, J. Yu, J. Hanna, G. Tynan, R. Doerner, K. Taylor, K. Schmid, "Molybdenum and Carbon Cluster Angular Sputtering Distributions Under Low Energy Xenon Ion Bombardment", *41st Joint Propulsion Conference*, **AIAA-2005-3525**, Tuscon, AZ (2005)
- ¹⁶L. Tao, B. Lee, A. Yalin, N. Yamamoto, A. Gallimore, "Development of a Cavity Ring-Down Spectroscopy Sensor for Boron Nitride Erosion in Hall Thrusters", *31st International Electric Propulsion Conference*, **IEPC-2009-146**, Ann Arbor, MI (2009)
- ¹⁷G. Sauerbrey, "Verwendung von Schwingquartzen zur Wägung dünner Schichten und zur Mikrowägung", *Zeitschrift für Physik*, **155** pp. 206-222 (1959)
- ¹⁸"SC-cut Parameters", Technical document received June 13, 2008 from Tangidyne Corporation.
- ¹⁹A. Ballato, T.J. Lukaszek, E.P. Eernisse, " ", *IEEE Transactions on Sonics and Ultrasonics*, vol. 6, pp. 163- (1979)
- ²⁰A.P. Yalin, J.D. Williams, V. Surla, K.A. Zoerb, "Differential Sputter Yield Profiles of Molybdenum due to Bombardment by Low Energy Xenon Ions at Normal and Oblique Incidence", *J. Phys. D: Appl. Phys.*, **40** 3194 (2007).
- ²¹L. Bachmann, J.J. Shin, "Measurement of the Sticking Coefficients of Silver and Gold in an Ultrahigh Vacuum", *J. Appl. Phys.*, **37** 1 pp. 242-246 (1966)
- ²²H.R. Kaufman, "Technology of Ion Beam Sources Used in Sputtering", *J. Vac. Sci. Technol.*, **15** 2 (1978)
- ²³C. Farnell, "Performance and Lifetime Simulation of Ion Thruster Optics", *Ph.D. Dissertation*, Colorado State University, April 2007
- ²⁴H.R. Kaufman, J.J. Cuomo, J.M.E. Harper, "Technology and Applications of Broad-Beam Ion Sources Used in Sputtering. Part I. Ion Source Technology", *J. Vac. Sci. Technol.*, **21** 3 (1982)
- ²⁵C.C. Farnell et. Al., "Multi-Axis Plasma Profiling System for Characterization of Plasma Thruster Plumes", *42nd Joint Propulsion Conference*, **AIAA-2006-4818**, Sacramento, CA (2006)
- ²⁶H. Hagstrum, "Auger Ejection of Electrons from Molybdenum by Noble Gas Ions", *Phys. Rev.*, **104**, 3, pp. 672-683 (1956)
- ²⁷H. Hagstrum, "Theory of Auger Ejection of Electrons from Metals by Ions", *Phys. Rev.*, **96**, 3, pp. 336-365 (1954)
- ²⁸*Hot-Pressed Boron Nitride Shapes*; Product Datasheet, Momentive Performance Materials: Albany, NY (2006) <http://www.advceramics.com/downloads/documents/81507.pdf>
- ²⁹*Combat Solid Boron Nitride Grade HP*; Product Datasheet, Saint-Gobain Advanced Ceramics: Amherst, NY (2008) <http://www.bn.saint-gobain.com/uploadedFiles/SGbn/Documents/Solids/Solid-Combat-BN-GradeHP.pdf>
- ³⁰J.L. Topper, B. Rubin, C.C. Farnell, A.P. Yalin, "Preliminary Results of Low Energy Sputter Yields of Boron Nitride due to Xenon Ion Bombardment", *44th Joint Propulsion Conference*, **AIAA-2008-5092**, Hartford, CT (2008)

- ³¹Y. Garnier, V. Viel, J-F. Roussel, J. Bernard, "Low-energy Xenon Ion Sputtering of Ceramics Investigated for Stationary Plasma Thrusters", *J. Vac. Sci. Tech. A*, **17** pp. 3246-3254 (1999)
- ³²S. Rusponi, G. Costantini, F. Buatier de Mongeot, C. Boragno, U. Valbusa, "Patterning a Surface on the Nanometric Scale by Ion Sputtering", *Appl. Phys. Lett.*, **75**, 21 (1999)
- ³³S. Park, B. Kahng, H. Jeong, A.-L. Barabási, "Dynamics of Ripple Formation in Sputter Erosion: Nonlinear Phenomena", *Phys. Rev. Lett.*, **83**, 17 (1999)
- ³⁴G. Costantini, S. Rusponi, R. Gianotti, C. Boragno, U. Valbusa, "Temperature Evolution of Nanostructures Induced by Ar⁺ Sputtering on Ag(001)", *Surface Science*, **416**, pp. 245-254 (1998)
- ³⁵B. Rubin, J.L. Topper, A.P. Yalin, "Total and Differential Sputter Yields of Boron Nitride Measured by Quartz Crystal Microbalance", *J. Phys. D: Appl. Phys.*, **42** 205205 (2009)
- ³⁶F. Taccogna, S. Longo, M. Capitelli, R. Schneider, "Hall Thruster Particle Model", *4th International Spacecraft Propulsion Conference, ESA-SP-555*, Sardinia, Italy (2004)
- ³⁷M. Scharfe, N. Gascon, M. Cappelli, "Comparison of Hybrid Hall Thruster Model to Experimental Measurements", *Phys. Plasmas*, **13**, 083505 (2006)
- ³⁸H. Liu, D.R. Yu, G.J. Yan, J.Y. Liu, "Investigation of the Start Transient in a Hall Thruster", *Contrib. Plasma Phys.*, **48**, 9, pp. 603-611 (2008)
- ³⁹H. Koizumi, K. Komurasaki, Y. Arakawa, "Numerical Prediction of Wall Erosion on a Hall Thruster", *Vacuum*, **83**, 1, pp. 67-71 (2009)
- ⁴⁰Z. Zhang, L. Zhang, "Anisotropic Angular Distribution of Sputtered Atoms", *Rad. Eff. Def. Sol.*, **159**, pp. 301-307 (2004)
- ⁴¹K.A. Zoerb, J.D. Williams, D.D. Williams, A.P. Yalin, "Differential Sputtering Yields of Refractory Metals by Xenon, Krypton, and Argon Ion Bombardment at Normal and Oblique Incidences", *29th International Electric Propulsion Conference, IEPC-2005-293*, Princeton, NJ (2005)
- ⁴²<http://srdata.nist.gov/xps>
- ⁴³R.D. Kolasinski, "Oblique Angle Sputtering Yield Measurements for Ion Thruster Grid Materials", *41st Joint Propulsion Conference, AIAA-2005-3526*, Tuscon, AZ (2005)
- ⁴⁴R.P. Doerner, D.G. Whyte, D.M. Goebel, "Sputtering Yield Measurements During Low Energy Xenon Plasma Bombardment", *J. Appl. Phys.*, **93** pp. 5816-5823 (2003)
- ⁴⁵A. Semenov, I. Shkarban, "Ion Beam Sputtering of the Surfaces of Ion and Plasma Sources", *Rocket and Space Engineering: Rocket Engines and Power Plants*, **3**, pp. 42-53 (in Russian) (1991)
- ⁴⁶V. Kim, V. Kozlov, A. Semenov, I. Shkarban, "Investigation of the Boron Nitride Based Ceramics Sputtering Yield Under It's Bombardment by Xe and Kr Ions", *30th International Electric Propulsion Conference, IEPC-2007-133*, Florence, Italy (2007)
- ⁴⁷J. Yim, "Computational Modeling of Hall Thruster Channel Wall Erosion", *Ph.D. Dissertation*, Univ. of Michigan, Ann Arbor, MI (2008)

- ⁴⁸Y. Yamamura, Y. Itikawa, N. Itoh, "Angular Dependence of Sputtering Yields of Monatomic Solids", *Institute of Plasma Physics, IPPJ-AM-26*, Nagoya, Japan (1983)
- ⁴⁹A.P. Yalin, B. Rubin, S. Domingue, Z. Glueckert, J. Williams, "Differential Sputter Yields of Boron Nitride, Quartz, and Kapton Due to Low Energy Xe⁺ Bombardment", *43rd Joint Propulsion Conference, AIAA-2007-5314*, Cincinnati, OH (2007)
- ⁵⁰E. Nikiporetz, A. Semenov, I. Shkarban, E. Khartova, "Sputtering Process of BN Based Ceramic by the Flows of Noncompensated Charge Plasma", *30th International Electric Propulsion Conference, IEPC-2007-007*, Florence, Italy (2007)
- ⁵¹L. Zhang, Z.L. Zhang, "Anisotropic Energy Distribution of Sputtered Atoms Induced by Low Energy Heavy Ion Bombardment", *Rad. Eff. Def. Sol.*, **160** 337 (2005)

Appendices

Appendix A: Sputter Yield Data Tables

Table A1. Raw sputter yield data for HBC-grade Boron Nitride. Yields represent condensable components, not converted total yields.

Material	Beam Energy (eV)	Ion Incidence Angle (degrees)	Azimuthal Angle (degrees)	MZ Fitted Yield (mm ³ /C)	MZ Fitted E* (eV)
HBC	350	0	0	0.029	88
HBC	350	0	0	0.042	75
HBC	350	0	0	0.030	86
HBC	350	0	0	0.039	70
HBC	350	0	0	0.029	88
HBC	300	0	0	0.042	58
HBC	300	0	0	0.030	40
HBC	300	0	30	0.032	69
HBC	300	0	60	0.030	102
HBC	250	0	0	0.039	28
HBC	250	0	0	0.034	23
HBC	250	0	60	0.026	49
HBC	250	0	0	0.039	59
HBC	250	0	0	0.039	28
HBC	250	30	0	0.053	44
HBC	250	30	60	0.049	64
HBC	250	30	90	0.050	56
HBC	200	0	0	0.029	1
HBC	200	0	0	0.035	34
HBC	200	0	0	0.029	8
HBC	200	0	0	0.030	38
HBC	200	0	0	0.026	41
HBC	200	0	0	0.023	48
HBC	200	0	0	0.030	57
HBC	150	0	0	0.016	0
HBC	150	0	60	0.019	43
HBC	150	0	0	0.019	17
HBC	100	0	0	0.015	13
HBC	100	0	0	0.014	21
HBC	100	0	0	0.013	9
HBC	100	0	0	0.015	13

Material	Beam Energy	Ion Incidence Angle	Azimuthal Angle	MZ Fitted Yield	MZ Fitted E*
HBC	100	15	0	0.014	12
HBC	100	15	0	0.017	8
HBC	100	15	0	0.018	
HBC	100	30	0	0.021	17
HBC	100	30	60	0.032	25
HBC	100	30	0	0.016	19
HBC	100	30	0	0.021	17
HBC	100	30	0	0.032	25
HBC	100	45	0	0.021	28
HBC	80	0	0	0.012	39
HBC	80	15	0	0.015	13
HBC	60	0	0	0.006	8
HBC	60	0	0	0.009	
HBC	40	0	0	0.013	1
HBC	40	0	0	0.009	17.7
HBC	40	15	0	0.002	1
HBC	40	15	0	0.018	1
HBC	40	15	0	0.011	1
HBC	40	45	0	0.021	1

Table A2. Raw sputter yield data for HBR-grade Boron Nitride

Material	Beam Energy (eV)	Ion Incidence Angle (degrees)	Azimuthal Angle (degrees)	MZ Fitted Yield (mm ³ /C)	MZ Fitted E* (eV)
HBR	250	0	0	0.038	45
HBR	250	0	60	0.032	28
HBR	250	0	0	0.039	60
HBR	250	0	0	0.035	37
HBR	250	45	0	0.060	56
HBR	250	45	60	0.083	58
HBR	250	45	0	0.067	48
HBR	200	0	0	0.030	50
HBR	200	0	0	0.021	56
HBR	200	0	0	0.030	50
HBR	200	0	0	0.039	
HBR	100	0	0	0.014	1
HBR	100	0	0	0.016	6
HBR	100	0	0	0.014	17
HBR	100	0	0	0.014	1
HBR	100	0	0	0.016	6
HBR	100	15	0	0.015	27
HBR	100	15	0	0.020	
HBR	100	30	0	0.018	38
HBR	100	45	0	0.021	27

Material	Beam Energy	Ion Incidence Angle	Azimuthal Angle	MZ Fitted Yield	MZ Fitted E*
HBR	80	0	0	0.014	35
HBR	80	0	60	0.011	7
HBR	80	0	0	0.014	28
HBR	80	15	0	0.020	32
HBR	80	15	60	0.016	16
HBR	80	15	0	0.021	32
HBR	80	30	0	0.021	126
HBR	80	30	60	0.020	80
HBR	80	30	0	0.021	106
HBR	60	0	0	0.006	2

Table A3. Raw sputter yield data for HP-grade Boron Nitride

Material	Beam Energy (eV)	Ion Incidence Angle (degrees)	Azimuthal Angle (degrees)	MZ Fitted Yield (mm ³ /C)	MZ Fitted E* (eV)
HP	250	0	0	0.053	71
HP	200	0	0	0.035	61
HP	200	0	0	0.044	
HP	200	45	0	0.044	68
HP	100	0	0	0.015	25
HP	100	15	0	0.015	19
HP	100	30	0	0.018	10
HP	100	45	0	0.040	43
HP	100	45	60	0.031	32
HP	100	45	0	0.046	43
HP	100	45	60	0.037	32
HP	100	45	0	0.038	41
HP	100	45	0	0.044	41
HP	80	15	0	0.028	37
HP	80	15	60	0.020	22
HP	80	15	0	0.027	36
HP	60	0	0	0.004	5
HP	60	45	0	0.006	1

Appendix B: MATLAB QCM Analysis Program

```
function executebutton_Callback(hObject, eventdata, handles)
% hObject    handle to executebutton (see GCBO)
% eventdata  reserved - to be defined in a future version of MATLAB
% handles    structure with handles and user data (see GUIDATA)

global filename;
global density;
global vb;
global Na;
global qe;
global Aqcm;
global rqcm;
global torad;
global todeg;
global str;

%define constants

%Avogadro's Number
Na=6.02214179*10^23;
%Electron Charge
qe=1.602176*10^-19;
%QCM piezoelectrically active area
if(strcmp(get(handles.Aqcmbox, 'Enable'), 'on'))
    Aqcm=str2double(get(handles.Aqcmbox, 'String'));
else
    Aqcm=0.535;
end
%Radius from QCM to sample surface center
if(strcmp(get(handles.rqcmbox, 'Enable'), 'on'))
    rqcm=str2double(get(handles.rqcmbox, 'String'));
else
    rqcm=17.5;
end
%conversion to radians from degrees
torad=pi/180;
%conversion to degrees from radians
todeg=180/pi;
%'per steradian' conversion factor
str=Aqcm/(rqcm^2);
%molecular weight for atoms/ion conversion
if(strcmp(get(handles.mwbox, 'Enable'), 'on'))
    MW=str2double(get(handles.mwbox, 'String'));
    MWbool=1;
else
    MW=1;
    MWbool=0;
end

%Get variable values from GUI, throw errors if empty
filenameboxtext=get(handles.filenamebox, 'String');
filename=[filenameboxtext, '.xls'];
```



```

density=str2double(get(handles.densitybox,'String'));
vb=str2double(get(handles.beamvoltagebox,'String'));
qcmerr=(str2double(get(handles.qcmerrbox,'String')))/100;

if(strcmp(filename, '.xls'))
    errordlg('File Name cannot be empty!');
end
if(density==0 || strcmp(density, ''))
    errordlg('Density cannot be zero!');
end
if(vb==0 || strcmp(vb, ''))
    errordlg('Beam Voltage cannot be zero!');
end

%Open the file to analyze, throw error if file is not found
fileextension=['C:\Program Files\MATLAB\QCM Files\',filename];
fid=fopen(fileextension, 'r');
if(fid== -1)
    errordlg('Could not find file. Is file in the analysis directory?
(C:\Program Files\MATLAB\QCM Files\)');
end

%see if the user wants to only use E* values which result in always
%positive zhang yields
if(get(handles.Estarchoicebox, 'Value') == 1.0)
    Estarchoice=1;
else
    Estarchoice=0;
end

%if the user wants only positive zhang yields, find out if they want to
use
%the new zhang yield (based on the E*max value) (default: Yes)
if(get(handles.Newyieldcheckbox, 'Value') == 1.0)
    Newyield=1;
else
    Newyield=0;
end

%extract data from file into arrays of size (n x 1) and
%find out how many datapoints are in the file

%Read-In Format #1: Excel Spreadsheet
%num=xlsread(fileextension);
%Beta=num(1,2);
%phiextract=num(:,3);
%alphaextract=num(:,4);
%timeextract=num(:,5);
%currentextract=num(:,7);
%massgainextract=num(:,6);
%datapoints=length(alphaextract);

%Read-In Format #2: Tab-delimited Text File

```

```

[time,betalist,phiextract,alphaextract,timeextract,massgainextract,curr
entextract,m1,m2,m3,m4,m5]=textread(fileextension,'%q %f %f %f %f %f %f
%f %f %f %f %f');
Beta=betalist(1,1);
datapoints=length(alphaextract);
fclose('all');

%eliminate pre- and post-test zeros
o=1;
for a=1:datapoints
    if(alphaextract(a,1)~=0)
        data(o,1)=alphaextract(a,1);
        data(o,2)=phiextract(a,1);
        data(o,3)=timeextract(a,1);
        if(get(handles.J1checkbox,'Value')== 1.0)
            %if the user has opted to use a J1 current, subtract this
value
            %from all currents in the list. Check to make sure user has
            %typed in a J1 current if they checked the box!
            j1current=(str2double(get(handles.J1box,'String')))/1000;
            %if(strcomp(num2str(j1current),''))
            %    errordlg('No J1 current entered!');
            %end
            data(o,4)=currentextract(a,1)-j1current;
        else
            data(o,4)=currentextract(a,1);
        end
        data(o,5)=massgainextract(a,1);
        o=o+1;
    end
end

datalength=length(data);

%Find the endpoints of each alpha and phi value, create conversiondata
for
%data conversion (so that's what conversiondata is for ....)
j=2;
k=2;
conversiondata(1,1)=data(1,1);
conversiondata(1,2)=data(1,2);
alphaindex(1,1)=1;
phiindex(1,1)=1;
phis(1,1)=data(1,2);
for x=2:datalength
    if(data(x,1)~=data(x-1,1))
        conversiondata(j,1)=data(x,1);
        conversiondata(j,2)=data(x,2);
        alphaindex(j,1)=x;
        if(data(x,2)~=data(x-1,2))
            phiindex(k,1)=x;
            phis(k,1)=data(x,2);
            k=k+1;
        end
        j=j+1;
    end
end

```

```

end
alphaindex(length(alphaindex)+1,1)=datalength;
%conversiondata(,) now contains all the alpha and phi values from the
first point of interest,
%or the point at which we begin taking data. alphaindex(1,1) will be
the index of that point
%in the array data(x,1). Thus, from alphaindex(1,1) to alphaindex(2,1)-
1 will be the
%datapoints from data(,) for the first alpha angle of the first phi
angle (i.e. alpha=-90,
%phi=0 for beta=0 or alpha=-120, phi=0 for beta=45)
%conversiondata will be a 2 x (#alphas) array containing alphas with no
repeats per phi in the
%first column and associated phis in the second column

%now we begin to process the data by calculating the current dose for
each
%datapoint starting by checking to see if we should use a sample
current.
%Make sure the user has entered a sample current if they checked the
box!
currentsum=0;
currents=0;
for q=1:datalength
    allcurrents(q,1)=data(q,4);
end
if(get(handles.samplecurrent1checkbox,'Value')==get(handles.samplecurre
nt1checkbox,'Max'))

samplecurrent=(str2double(get(handles.samplecurrent1box,'String')))/100
0;
    currents=1;
    if(get(handles.samplecurrent2checkbox,'Value')==1.0)

samplecurrent2=(str2double(get(handles.samplecurrent2box,'String')))/10
00;
        currents=2;
        if(get(handles.samplecurrent3checkbox,'Value')==1.0)

samplecurrent3=(str2double(get(handles.samplecurrent3box,'String')))/10
00;
            currents=3;
            if(get(handles.samplecurrent4checkbox,'Value')==1.0)

samplecurrent4=(str2double(get(handles.samplecurrent4box,'String')))/10
00;
                currents=4;
            end
        end
    end
end
if(currents==1)
    for q=1:datalength
        currentsum=currentsum+data(q,4);
    end

```

```

currentratio=samplecurrent/(currentsum/datalength);

for f=1:datalength
    data(f,4)=data(f,4)*currentratio;
end

elseif(currents==2)
    for q=1:(phiindex(2,1)-1)
        currentsum=currentsum+data(q,4);
    end
    currentratio=samplecurrent/(currentsum/(phiindex(2,1)-1));
    for f=1:(phiindex(2,1)-1)
        data(f,4)=data(f,4)*currentratio;
    end
    currentsum=0;

    for q=phiindex(2,1):datalength
        currentsum=currentsum+data(q,4);
    end
    currentratio=samplecurrent2/(currentsum/(datalength-
phiindex(2,1)));
    for f=phiindex(2,1):datalength
        data(f,4)=data(f,4)*currentratio;
    end

elseif(currents==3)
    for q=1:(phiindex(2,1)-1)
        currentsum=currentsum+data(q,4);
    end
    currentratio=samplecurrent/(currentsum/(phiindex(2,1)-1));
    for f=1:(phiindex(2,1)-1)
        data(f,4)=data(f,4)*currentratio;
    end
    currentsum=0;

    for q=phiindex(2,1):(phiindex(3,1)-1)
        currentsum=currentsum+data(q,4);
    end
    currentratio=samplecurrent2/(currentsum/(phiindex(3,1)-1-
phiindex(2,1)));
    for f=phiindex(2,1):(phiindex(3,1)-1)
        data(f,4)=data(f,4)*currentratio;
    end
    currentsum=0;

    for q=phiindex(3,1):datalength
        currentsum=currentsum+data(q,4);
    end
    currentratio=samplecurrent3/(currentsum/(datalength-
phiindex(3,1)));
    for f=phiindex(3,1):datalength
        data(f,4)=data(f,4)*currentratio;
    end

else

```

```

for q=1:(phiindex(2,1)-1)
    currentsum=currentsum+data(q,4);
end
currentratio=1;
for f=1:(phiindex(2,1)-1)
    data(f,4)=data(f,4)*currentratio;
end
currentsum=0;

for q=phiindex(2,1):(phiindex(3,1)-1)
    currentsum=currentsum+data(q,4);
end
currentratio=1;
for f=phiindex(2,1):(phiindex(3,1)-1)
    data(f,4)=data(f,4)*currentratio;
end
currentsum=0;

for q=phiindex(3,1):(phiindex(4,1)-1)
    currentsum=currentsum+data(q,4);
end
currentratio=1;
for f=phiindex(3,1):(phiindex(4,1)-1)
    data(f,4)=data(f,4)*currentratio;
end
currentsum=0;

for q=phiindex(4,1):datalength
    currentsum=currentsum+data(q,4);
end
currentratio=1;
for f=phiindex(4,1):datalength
    data(f,4)=data(f,4)*currentratio;
end
end

%factor fast neutrals & CEX into sample currents
kb=1.380658*(10^-23);
Tin=str2double(get(handles.Temperaturebox, 'String'));
P1=str2double(get(handles.pressure1box, 'String'));
P2=str2double(get(handles.pressurepowerbox, 'String'));
Ptorr=P1*(10^P2);
%'corr' is the correction factor on the ion gauge for the fuel gas
if(get(handles.Hebutton, 'Value')==get(handles.Hebutton, 'Max'))
    corr=0.15;
elseif(get(handles.N2button, 'Value')==get(handles.N2button, 'Max'))
    corr=1;
elseif(get(handles.Arbutton, 'Value')==get(handles.Arbutton, 'Max'))
    corr=1.19;
elseif(get(handles.Krbutton, 'Value')==get(handles.Krbutton, 'Max'))
    corr=1.86;
else
    corr=2.87;
end
nd=Ptorr*133.322/(kb*Tin*corr);
%'nd' is the number density per m^3

```

```

sigma=(87.3-(13.6*log10(vb)))*10^-20;
%'sigma' is collision cross-section. This equation comes from fitted
data and
%is in Angstroms^2, hence the 10^-20 factor on the end.
mfp=1/(nd*sigma);
%'mfp' is mean free path
corrfactor=1/exp(-0.23/mfp);
%0.23 is the radius (in meters) from the grids to the target

%multiply all currents by the CEX correction factor
for w=1:datalength
    data(q,4)=data(q,4)*corrfactor;
end

%create a data column "current dose" used in the conversion to mm^3/C
and
%calculate a least-squares regression on a linear fit to each
%individual 'mass gain' @ 'alpha value' vs. current dose. Compute the
r-squared
%values of that fit and, if r-squared < 0.99, drops the first data
point at
%this alpha and repeats until r-squared is at least 0.99 or it has
dropped
%7 datapoints.
for m=1:length(alphaindex)-1
    t=1;
    lim=0;
    massgainsum=0;
    currentsum=0;
    n1=alphaindex(m,1);
    n2=alphaindex(m+1,1)-1;
    masspoints=zeros(n2-n1,1);
    currentdosepoints=zeros(n2-n1,1);
    repeat=1;

    while(repeat)
        for n=n1:n2
            masspoints(t,1)=data(n,5);
            if(t==1)
                currentdosepoints(t,1)=data(n,4)*(data(n+1,3)-
data(n,3));
            else
                currentdosepoints(t,1)=currentdosepoints(t-
1,1)+(data(n,4)*(data(n,3)-data(n-1,3)));
            end
            massgainsum=massgainsum+data(n,5);
            currentsum=currentsum+data(n,4);
            t=t+1;
        end
        ntot=n2-n1;
        avemassgain=massgainsum/ntot;

        if(avemassgain<10^-9 && avemassgain>0)

```

```

outliers=excludedata(currentdosepoints,masspoints,'range',[(avemassgain
-(avemassgain*10) (avemassgain+(avemassgain*10))]);
    ignore=0;
    elseif(avemassgain<0)
        ignore=1;
    else

outliers=excludedata(currentdosepoints,masspoints,'range',[(avemassgain
/100) (avemassgain*100)]);
    ignore=0;
end

%if the average mass gain is zero or negative, take zero yield.
%Otherwise, treat the data as is and find a fit
if(ignore)
    slope=0;
    rsquared=1;
else
    OPTIONS=fitoptions('Exclude',outliers);
    [cfun,
cfunvalues]=fit(currentdosepoints,masspoints,'poly1',OPTIONS);
    rsquared=double(cfunvalues.rsquare);
    slope=cfun.p1;
end
%the slope of the fit line will be in grams per Coulomb. Divide
%by the density to get cm3/C. Multiply by 1000 to get mm3/C.

if(rsquared<0.99 && lim<7)
    n1=n1+1;
    repeat=1;
    lim=lim+1;
    t=1;
else
    repeat=0;
end
end

%conversion from grams/Coulomb to mm3/C/sr
qcmyield(m,1)=(slope*1000)/(density*str);
conversiondata(m,5)=qcmyield(m,1);

%this is the yield for each alpha value in mm3/C

clear masspoints timepoints;

end

%convert alphas and phis to target frame for Zhang fitting
[conversiondata]=AngleConversionData(conversiondata,Beta);

%create full list of alphas & phis (for all phis) for -90<=alpha<=90 to
evaluate Zhang fit
%at all points. Begin constructing the array to output the data
(Alldata)

```

```

[alphaneu,phinew]=AngleConversion(phiindex,data,Beta);
for t=0:length(phis)-1
    for r=1:181
        Alldata(r+(181*t),1)=phis(t+1,1);
    end
end
for lt=1:181
    alphaza(lt,1)=lt-91;
end

for m=0:length(phis)-1
    for s=1:90
        Alldata(s+(181*m),2)=alphaza(s,1);
    end
    for s=91:181
        Alldata(s+(181*m),2)=alphaza(s,1);
    end
end
for s=1:90
    alphaza(s,1)=alphaza(s,1)*-1;
end

%define least-squares routine to fit the Zhang equation to our
datapoints.
%Mp0 are 'initial guesses' to input to 'leastsquares'
Mp0(1,1)=vb/2;
Mp0(2,1)=0.01;
%Mpin=zeros(2,1);

%format for fmincon is (@function, initial guess,[],[],[],[],lower
bound,
%upper bound,[],OPTIONS,function parameters). If you are not
%using a lower bound, an upper bound, or OPTIONS, the format for those
%values is []. 'leastsquare' returns a vector of the differences
between the
%datapoints and the calculated Zhang values, which fmincon then
minimizes
%by re-calling the function with new initial guess(Mp0) values. Mp is
then the
%output, a vector (L x 1) of the minimized values (in our case, E* and
Y)
OPTIONS=optimset('MaxFunEvals',500000,'MaxIter',200,'TolFun',5e-9);
lb=[0,0];
%Mp=lsqnonlin(@ (Mpin)leastsquare(Mpin,vb,Beta,conversiondata),Mp0,[],[],
,OPTIONS);
[Mp6,fval,exitflag,output]=fmincon(@leastsquare,Mp0,[],[],[],[],lb,[],[
],OPTIONS,vb,Beta,conversiondata);
[Mp,fval,exitflag,output]=fmincon(@leastsquare,Mp0,[],[],[],[],lb,[],[
,OPTIONS,vb,Beta,conversiondata);

%calculate the maximum E* value less than or equal to the original E*
value
%which yields positive Zhang yields for all alphas, if the user wants
to do so
if(Estarchoice)
    Estar = ZhangMaxEstar(alphaneu,phinew,Mp(1,1),Mp(2,1),vb,Beta);

```



```

else
    Estar=Mp(1,1);
end

%recalculate the optimum yield for the Zhang fit using the given E*max
if
%user wants to do so
Mp2=Mp(2,1);
if(Newyield)

%ZYield=lsqnonlin(@ (Mp3) leastsquareE (Mp3, Estar, vb, Beta, conversiondata),
    %Mp2);

[ZYield, fval, exitflag, output]=fmincon(@leastsquareE, Mp2, [], [], [], [], lb,
[], [], OPTIONS, Estar, vb, Beta, conversiondata);
else
    ZYield=Mp(2,1);
end

for e=1:length(phis)
    yz(:,e)=ZhangAll (alphaza(:,1), phinew(:,e), Estar, ZYield, vb, Beta);
    %yz(:,e)=ZhangAll (alphaza(:,1), phis(e), Estar, ZYield, vb, Beta);
    flag=0;

    %for r=2:length(yz)
    %    test=yz(r,e);
    %    if(test<=0 && flag==0)
    %        if(test==0)
    %            trans=length(yz)-r;
    %            flag=1;
    %        else
    %            trans=length(yz)-r;
    %            flag=1;
    %        end
    %    end
    %end

    %for r2=trans+1:length(yz)
    %    yzout(r2,e)=yz(r2-trans,e);
    %end

end

%Build the output array to export for the MATLAB graphing program.
Alldata
%will contain all data necessary to produce 2-D and 3-D plots for
reports
for k=0:length(phis)-1
    for s=1:length(alphanew)
        Alldata(s+(181*k),3)=yz(s,k+1);
        Alldata(s+(181*k),4)=(ZYield*cos((alphanew(s,k+1))*torad))/pi;
    end
end
end

```

```

%append the datapoint alphas, qcm values, and qcm errors to the dataout
%array listed by phi. Recall that the dataout array has 181 points per
phi
%and the conversiondata array has (datapoints @ phi) points per phi, so
we
%write 0's to all cells past the number of datapoints at each phi
before
%starting anew with the next phi.
t=2;
for s=0:length(phis)-1
    Alldata(1+(s*181),5)=conversiondata(t-1,3)*-1;
    Alldata(1+(s*181),6)=conversiondata(t-1,5);
    Alldata(1+(s*181),7)=qcmerr*conversiondata(t-1,5);
    h=-1;
    for w=1:181
        if(t<=length(conversiondata))
            if(conversiondata(t,2)==conversiondata(t-1,2))
                if(abs(conversiondata(t,3))<abs(conversiondata(t-1,3))
&& h~=1)
                    h=-1;
                else
                    h=1;
                end

                Alldata(w+(181*s)+1,5)=conversiondata(t,3)*h;
                Alldata(w+(181*s)+1,6)=conversiondata(t,5);
                Alldata(w+(181*s)+1,7)=qcmerr*conversiondata(t,5);
                t=t+1;
            else
                if(w+(181*s)<length(Alldata))
                    Alldata(w+(181*s)+1,5)=0;
                    Alldata(w+(181*s)+1,6)=0;
                    Alldata(w+(181*s)+1,7)=0;
                end
            else
                if(w+(181*s)<length(Alldata))
                    Alldata(w+(181*s)+1,5)=0;
                    Alldata(w+(181*s)+1,6)=0;
                    Alldata(w+(181*s)+1,7)=0;
                end
            end
        end
        t=t+1;
    end

    Alldata(1,8)=Mp(2,1);
    Alldata(1,9)=Mp(1,1);
    Alldata(1,10)=0;
    if(MWbool)
        Alldata(1,11)=(Mp(2,1)*Na*qe*density)/(1000*MW);
    end

t=1;
OPTIONS=optimset('MaxFunEvals',500000,'MaxIter',200,'TolFun',5e-9);
for u=1:length(phis)

```

```

Mpphi0(1,1)=Mp(1,1);
Mpphi0(2,1)=Mp(2,1);
v=2;
singlephidata(1,1)=conversiondata(t,1);
singlephidata(1,2)=conversiondata(t,2);
singlephidata(1,3)=conversiondata(t,3);
singlephidata(1,4)=conversiondata(t,4);
singlephidata(1,5)=conversiondata(t,5);
t=t+1;
while (conversiondata(t,2)==conversiondata(t-1,2))
    singlephidata(v,1)=conversiondata(t,1);
    singlephidata(v,2)=conversiondata(t,2);
    singlephidata(v,3)=conversiondata(t,3);
    singlephidata(v,4)=conversiondata(t,4);
    singlephidata(v,5)=conversiondata(t,5);
    t=t+1;
    if(t>length(conversiondata))
        break;
    end
    v=v+1;
end

%Mpphi=fmincon(@leastsquare,Mp0,[],[],[],[],lb,[],[],OPTIONS,vb,Beta,conversiondata);

[Mpphi,fval,exitflag,output]=fmincon(@leastsquare,Mpphi0,[],[],[],[],lb,[],[],OPTIONS,vb,Beta,singlephidata);
Alldata(u+1,8)=Mpphi(2,1);
Alldata(u+1,9)=Mpphi(1,1);
Alldata(u+1,10)=phis(u);
if(MWbool)
    Alldata(u+1,11)=(Mpphi(2,1)*Na*qe*density)/(1000*MW);
end

end

Alldata(1,12)=vb;
Alldata(2,12)=Beta;
if(get(handles.samplecurrent1checkbox,'Value')==1.0)
    Alldata(3,12)=samplecurrent;
end
if(get(handles.samplecurrent2checkbox,'Value')==1.0)
    Alldata(4,12)=samplecurrent2;
end
if(get(handles.samplecurrent3checkbox,'Value')==1.0)
    Alldata(5,12)=samplecurrent;
end
if(get(handles.samplecurrent4checkbox,'Value')==1.0)
    Alldata(6,12)=samplecurrent;
end

fileoutputextension1=['C:\Program Files\MATLAB\QCM
Files\',filenameboxtext];
fileoutputextension=[fileoutputextension1,'_conv.xls'];

xlswrite(fileoutputextension, Alldata);

```

```

Estarout=num2str(Mp(1,1));
Yieldout=num2str(Mp(2,1));

msg=['Conversion and Output Complete! Output file:
',fileoutputextension];
msg2=['E*: ',Estarout,' eV'];
msg3=['Ytotal: ',Yieldout,' mm^3/C'];
msg4='Creating Hemisphere and Zhang-slice Plots...';
msg5='Done plotting! Thank You!';
disp(msg);
disp(msg2);
disp(msg3);
disp(msg4);
plotting(fileoutputextension,torad, Beta, vb, singlephidata);
disp(msg5);
close(QCMAGUI);

end

%Plotting Function

function plotting (fileoutputextension,torad, Beta, vb, singlephidata)

num = xlsread(fileoutputextension); %load data from the file

%now convert the data
beta=Beta; %incidence angle
E=vb; %ion energy
p=1; %phi counter
c=1; %global counter
a=1;

while c<=length(num)
    phi(a,p)=num(c,1);
    alpha(a,p)=num(c,2);
    y_zhang(a,p)=num(c,3);
    y_diffuse(a,p)=num(c,4);
    if(a<length(num))
        if (num(a,5)~=0 || (num(a,2)<0 && num(a,5)==0 &&
num(a+1,5)~=0))
            alpha_exp(a,p)=num(c,5);
            y_exp(a,p)=num(c,6);
            y_exp_err(a,p)=num(c,7);
            end
        end

        if c==1 %first row - Zhang parameters for all phi angles
            y_tot=num(c,8);
            E_star=num(c,9);
        elseif num(c,8)~=0 %other rows with non-zero Y_tot and E*
values - individual phis
            ytot(a)=num(c-1,8);
            estar(a)=num(c-1,9);

```

```

end
if (num(c+1)~=num(c)) || (c==length(num))
    figure
    plot(alpha(:,p),y_zhang(:,p),'-b','Linewidth',2);
    hold on
    plot(alpha(:,p),y_diffuse(:,p),'--g','Linewidth',2);

errorbar(alpha_exp(1:length(alpha_exp),p),y_exp(1:length(y_exp),p),y_ex
p_err(1:length(y_exp_err),p),'r','MarkerSize',15);
    grid on
    legend('Zhang','Diffuse','QCM');
    xlabel('\alpha,degrees');
    ylabel('mm^3/C/sr');

ylim([0,max([max(y_exp(:,p))+max(y_exp_err(:,p)),max(y_zhang(:,p)),max(
y_diffuse(:,p)))]*1.1)];
    xlim([-90 90]);
    hold off
    p=p+1; %next phi
    a=0;
end
c=c+1;
a=a+1;
end

%Now plot 3D hemisphere
clear alpha phi
alpha=[-pi/2:pi/100:-pi/100,pi/100:pi/100:pi/2];
phi=0:pi/100:2*pi;
[alpha1,phil]=meshgrid(alpha,phi);
for l=1:length(phi);
    for k=1:length(alpha)
        x(1,k)=sin(alpha1(1,k))*cos(phil(1,k));
        y(1,k)=sin(alpha1(1,k))*sin(phil(1,k));
        z(1,k)=cos(alpha1(1,k));
        if (abs(abs(alpha1(1,k))-pi/2)<1e-8) || (abs(alpha1(1,k))<1e-
8) || (abs(abs(alpha1(1,k))-pi)<1e-8)
            yield(1,k)=0;
        else
            gamma=(3*(sin(alpha1(1,k)))^2-
1)/((sin(alpha1(1,k)))^2)+(cos(alpha1(1,k)))^2*(3*(sin(alpha1(1,k)))^2+
1)/(2*(sin(alpha1(1,k)))^3))*log((1+sin(alpha1(1,k)))/(1-
sin(alpha1(1,k))));
            yield(1,k)=y_tot/(1-
sqrt(E_star/E)*cos(beta*torad))*cos(alpha1(1,k))/pi*(1-
0.25*sqrt(E_star/E)*cos(beta*torad)*gamma+3/2*pi*sin(beta*torad)*sin(a
lpha1(1,k))*cos(phil(1,k)));
        end
        yield_x(1,k)=yield(1,k)*sin(alpha1(1,k))*cos(phil(1,k));
        yield_y(1,k)=yield(1,k)*sin(alpha1(1,k))*sin(phil(1,k));
        yield_z(1,k)=yield(1,k)*cos(alpha1(1,k));
    end
end
figure

surf(x(:,1:51),y(:,1:51),z(:,1:51),yield(:,1:51),'EdgeColor','none');
h=gca;

```

```

set(gca, 'Visible', 'off');
set(gcf, 'Color', 'white')
colorbar;
axis equal;
grid off;
view([37.5 45]);
% title(strcat('Y=', num2str(y_tot), ' cm^3/C;
E^*=', num2str(E_star)));
% backward sputter lobe
figure

surf(x(:,1:51), y(:,1:51), z(:,1:51), yield(:,1:51), 'EdgeColor', 'none');
h=gca;
set(gca, 'Visible', 'off');
set(gcf, 'Color', 'white')
colorbar;
axis equal;
grid off;
% title(strcat('Y=', num2str(y_tot), ' cm^3/C;
E^*=', num2str(E_star)));
view([217.5 45]);

end

function [yz] =
ZhangAll(alphanew, phinew, Estarvalue, Yieldvalue, Energyvalue, Betavalue)
global torad;
for x=1:length(alphanew)
    if(round(alphanew(x,1))==0)
        gamma(x,1)=5.333;
    else
        gamma1=((3*(sin(alphanew(x,1)*torad))^2)-
1)/((sin(alphanew(x,1)*torad))^2);
gamma2=((cos(alphanew(x,1)*torad))^2)*((3*(sin(alphanew(x,1)*torad))^2
)+1)/(2*(sin(alphanew(x,1)*torad))^3);
        gamma3=log((1+sin(alphanew(x,1)*torad))/(1-
sin(alphanew(x,1)*torad)));
        gamma(x,1)=gamma1+(gamma2*gamma3);
    end

    if(x<(length(alphanew)/2))
        phimult=-1;
    else
        phimult=1;
    end

    if(round(alphanew(x,1))==90 || round(alphanew(x,1))==90)
        yz(x,1)=0;
    else
        yz1=Yieldvalue/(1-
((sqrt(Estarvalue/Energyvalue))*cos(Betavalue*torad)));
        yz2=(cos(alphanew(x,1)*torad))/pi;
        yz3=0.25*(sqrt(Estarvalue/Energyvalue))*((cos(Betavalue*torad))*gamma(

```

```

x,1))+1.5*pi*(sin(Betavalue*torad))*(sin(alphanew(x,1)*torad))*(phimul
t));
        yz(x,1)=yz1*yz2*(1-yz3);
    end
end
end

%Zhang single datapoint evaluation for least squares fitting
function [yzs] =
SinglePointZhang(conversiondata,Estarvalue,Yieldvalue,Energyvalue,Betav
alue,f)
global torad;
    if (conversiondata(f,3)*torad<=10^-3)
        gamma=5.333;
    else
        gamma1=((3*(sin(conversiondata(f,3)*torad))^2)-
1)/((sin(conversiondata(f,3)*torad))^2);
        gamma2=((cos(conversiondata(f,3)*torad))^2)*((3*(sin(conversiondata(f,
3)*torad))^2)+1)/(2*(sin(conversiondata(f,3)*torad))^3);
        gamma3=log((1+sin(conversiondata(f,3)*torad))/(1-
sin(conversiondata(f,3)*torad)));
        gamma=gamma1+(gamma2*gamma3);
    end

    if (single(conversiondata(f,3))==90 ||
single(conversiondata(f,3))==double(-90))
        yzs=0;
    else
        yz1=Yieldvalue/(1-
((sqrt(Estarvalue/Energyvalue))*cos(Betavalue*torad)));
        yz2=(cos(conversiondata(f,3)*torad))/pi;
        yz3=0.25*(sqrt(Estarvalue/Energyvalue))*((cos(Betavalue*torad))*gamma)
+(1.5*pi*(sin(Betavalue*torad))*(sin(conversiondata(f,3)*torad))*(cos(c
onversiondata(f,4)*torad)));
        yzs=yz1*yz2*(1-yz3);
    end
end

%evaluate the Zhang equation with our given parameters to find the
largest
%value of E* which maintains a positive value of the Zhang yield at all
%points (Given Y, E*, Alphas, Phis, Beta, Beam Energy, find E*max)
function [Estarmax] =
ZhangMaxEstar(Alphavalue,Phivalue,Estarvalue,Yieldvalue,Energyvalue,Bet
avalue)
global yz;
global torad;
    for x=1:length(Alphavalue)
        if ((Alphavalue(x,1)*torad)<=10^-3)
            gamma(x,1)=5.333;
        else
            gamma1=((3*(sin(Alphavalue(x,1)*torad))^2)-
1)/((sin(Alphavalue(x,1)*torad))^2);

```

```

gamma2=((cos(Alphavalue(x,1)*torad))^2)*((3*(sin(Alphavalue(x,1)*torad
))^2)+1)/(2*(sin(Alphavalue(x,1)*torad))^3);
gamma3=log((1+sin(Alphavalue(x,1)*torad))/(1-
sin(Alphavalue(x,1)*torad)));
gamma(x,1)=gamma1+(gamma2*gamma3);
end

if((Alphavalue(x,1)*torad)==double(pi/2) ||
(Alphavalue(x,1)*torad)==double(-pi/2))
yz(x,1)=0;
else
yz1=Yieldvalue/(1-
(sqrt(Estarvalue/Energyvalue))*cos(Betavalue*torad));
yz2=(cos(Alphavalue(x,1)*torad))/pi;

yz3=0.25*(sqrt(Estarvalue/Energyvalue))*((cos(Betavalue*torad))*gamma(
x,1)+(1.5*pi*(sin(Betavalue*torad))*(sin(Alphavalue(x,1)*torad))*(cos(
Phivalue(x,1)*torad)));
yz(x,1)=yz1*yz2*(1-yz3);
end

if(yz(x,1)<0)
x=1;
Estarvalue=Estarvalue-0.5;
clear yz;
end
end
Estarmax=Estarvalue;
end

%convert full list of alphas spanning -90 to 90 for Zhang fit profile
function [alphanew,phinew] = AngleConversion(phiindex,data,Beta)
global torad;
global todeg;
for c=1:length(phiindex)
philab(c,1)=data(phiindex(c,1),2)*torad;
if(Beta==0)
alphaprime(c,1)=(-pi/2)*todeg;
else
alphaprime(c,1)=(-
pi+(atan(1/((tan(Beta*torad))*(cos(philab(c,1)))))))*todeg;
end
end

for d=1:length(philab)
for x=0:180

R=(cos((philab(d,1))*torad))*(sin((alphaprime(d,1)+x)*torad));
S=cos((alphaprime(d,1)+x)*torad);
T=(sin((alphaprime(d,1)+x)*torad))*(sin(philab(d,1)*torad));
U=((cos(Beta*torad))*R)+((sin(Beta*torad))*S);
W=(-sin(Beta*torad))*R)+((cos(Beta*torad))*S);
Y=(U^2)+(T^2);
alphanew(x+1,d)=(acos(W))*todeg;
if (Y==0)

```



```

        phinew(x+1,d)=0;
    elseif (U<=0)
        phinew(x+1,d)=(pi-asin(T/(sqrt(Y))))*todeg;
    elseif (U>0)
        phinew(x+1,d)=(asin(T/(sqrt(Y))))*todeg;
    end
end
end
end

%convert alpha and phi datapoints to target frame (columns 3,4 in
%conversiondata)
function [conversiondata] = AngleConversionData(conversiondata,Beta)
global torad;
global todeg;
    for d=1:length(conversiondata)

R=(cos(conversiondata(d,2)*torad))*((sin((conversiondata(d,1))*torad)));
;
        S=cos((conversiondata(d,1))*torad);

T=(sin((conversiondata(d,1))*torad))*(sin(conversiondata(d,2)*torad));
        U=((cos(Beta*torad))*R)+((sin(Beta*torad))*S);
        W=(-sin(Beta*torad))*R+((cos(Beta*torad))*S);
        Y=(U^2)+(T^2);
        conversiondata(d,3)=(acos(W))*todeg;
        if (Y==0)
            conversiondata(d,4)=0;
        elseif (U<=0)
            conversiondata(d,4)=(pi-asin(T/(sqrt(Y))))*todeg;
        elseif (U>0)
            conversiondata(d,4)=(asin(T/(sqrt(Y))))*todeg;
        end
    end
end

function [diffsum] = leastsquare(Mpin,E,Beta,conversiondata)
diffs=zeros(length(conversiondata),1);
diffsum=0;
    for f=2:length(conversiondata)-1
        diffs(f,1)=1000*(conversiondata(f,5)-
double(SinglePointZhang(conversiondata,Mpin(1,1),Mpin(2,1),E,Beta,f)));
    end
    diffsum=sqrt(sum(diffs.^2));
end

function [diffsum]=leastsquareE(Mp1,Estar,E,Beta,conversiondata)
diffs2=zeros(length(conversiondata),1);
    for f=2:length(conversiondata)-1
        diffs2(f,1)=1000*(conversiondata(f,5)-
double(SinglePointZhang(conversiondata,Estar,Mp1,E,Beta,f)));
    end
    diffsum=sqrt(sum(diffs2.^2));
end

```